Fill Factor Loss Mechanisms:

Analysis and Basic Understanding in Silicon Hetero-junction Solar Cells

by

Mehdi (Ashling) Leilaeioun

A Dissertation Presented in Partial Fulfillment
of the Requirements for the Degree
Doctor of Philosophy

Approved July 2018 by the
Graduate Supervisory Committee:

Stephen M. Goodnick, Co-Chair
Michael Goryll, Co-Chair
Mariana Bertoni
Stuart Bowden
Michael Stuckelberger

ARIZONA STATE UNIVERSITY

August 2018

ABSTRACT

The objective of this thesis is to achieve a detailed understanding of the loss mechanisms in SHJ solar cells. The working principles of these cells and what affects the cell operation, e.g. the IV characteristics at the maximum power point (MPP) and the correspondingly fill factor (FF) are investigated. Different loss sources are analyzed separately, and the weight of each in the total loss at the MPP are evaluated. The total series resistance is measured and then compared with the value obtained through summation over each of its components. In other words, series resistance losses due to recombination, vertical and lateral carrier transport, metalization, etc, are individually evaluated, and then by adding all these components together, the total loss is calculated. The concept of fill factor and its direct dependence on the loss mechanisms at the MPP of the device is explained, and its sensitivity to nearly every processing step of the cell fabrication is investigated. This analysis provides a focus lens to identify the main source of losses in SHJ solar cells and pave the path for further improvements in cell efficiency.

In this thesis, we provide a detailed understanding of the FF concept; we explain how it can be directly measured; how it can be calculated and what expressions can better approximate its value and under what operating conditions. The relation between $FF$and cell operating condition at the MPP is investigated. We separately analyzed the main FF sources of losses including recombination, sheet resistance, contact resistance and metalization. We study FF loss due to recombination and its separate components which include the Augur, radiative and SRH recombination is investigated. We study FF loss due to contact resistance and its separate components which include the contact resistance of different interfaces, e.g. between the intrinsic and doped a-Si layers, TCO and a-Si layers. We also study FF loss due to lateral transport and its components that including the TCO sheet resistance, the finger and

the busbars resistances.

To Farzaneh Mohamadi (my mother), Sarah Kurtz (my role model)

and

Clarice Lispector (my hero)

ACKNOWLEDGMENT

I would like to express my sincere gratitude to my advisers and mentors, Dr. Stephan M. Goodnick, Dr. Michael Goryll and Dr. Christina Honsberg for their appreciable patience and support. I am deeply indebted for their guidance and encouragement that helped me a great deal in the completion and success of this study. I would like also to thank my committee members, Dr. Mariana Bertoni, Dr. Stwart Bowden and Dr. Michael Stuckelberger, for their invaluable comments. I also wish to thank Dr. Varda Faghir Hagh, Dr. Mojdeh Khorsand, Dr. Michelle Jordan, Dr. Delia Saenz, Dr. Silvana Ayala and Dr. Michael Stuckelberger, without them I would not have such colorful memories to cherish. Last but not least, I would like to thank my parents for their unconditional love and sustained support which was my main source of motivation in the face of challenges.

TABLE OF CONTENTS

CHAPTER Page

LIST OF TABLES

LIST OF FIGURES

Chapter 1

Introduction

1.1 Motivation

Several countries have already installed solar panels and reached grid parity in many locations. The Compound Annual Growth Rate (CAGR) of PV installations was 40% between 2010 to 2016 [1]. Cell processing related costs are typically less than around 20% of the total module cost and only about 10% of the system level. While at first sight, it seems that increasing the cell power efficiency may not play a significant role, it can actually provide a direct path to decrease the levelized cost of electricity (LCOE)[1].

With the goal of boosting cell efficiency, in this thesis we focus mainly on advances in silicon photovoltaic (PV) technology, which compared with other technologies has already successfully transformed to large scale and mass-production, where it is currently leading the photovoltaic market [5, 6]. Si-wafer based PV technology accounted for about 94% of the total world production in 2016. The share of multi-crystalline technology is now about 70% of the total production. In the last 10 years, the efficiency of the average commercial wafer-based silicon modules increased from about 12% to 17%.

Silicon solar cell industry takes advantage of the stability, abundance and non-toxicity of silicon material. It's energy band gap is at 1.12 eV and is well matched to the solar spectrum, very close to the optimum value for solar-to-electric energy conversion using a single semiconductor optical absorber [7]. Figure 1.1 shows the

[1]The levelized cost of electricity (LCOE) is a measure of a power source which attempts to compare different methods of electricity generation on a consistent basis. It is an economic assessment of the average total cost to build and operate a power-generating asset over its lifetime divided by the total energy output of the asset over that lifetime. The LCOE can also be regarded as the average minimum cost at which electricity must be sold in order to break-even over the lifetime of the project.

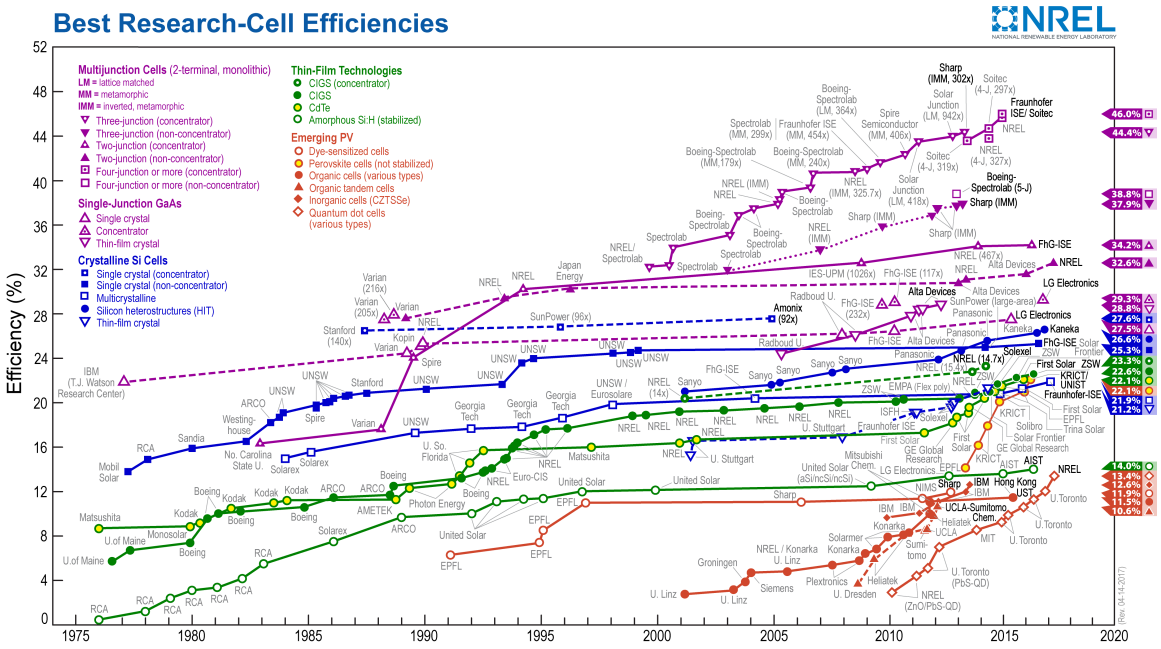

Figure 1.1: Efficiency chart for various PV technologies (taken from www.nrel.gov).

efficiency chart for various solar technologies; silicon PV technologies are shown in blue. The evolution of the energy conversion efficiencies of silicon PV is shown in Fig. 1.2 in more detail. Advanced cell architectures are one route that can be applied to silicon PV technology to achieve significantly higher cell efficiency. Currently, high-quality mono crystalline silicon (c-Si) heterojunction (SHJ) solar cells hold the world record for a single junction cell with an efficiency at 26.6% [8].

Heterojunction cells have a unique advantage over traditional homojunction cells. Their high open circuit voltage (V_{OC}) is the result of the better passivation quality resulting from depositing hydrogenated amorphous silicon (a-Si:H) on c-Si and also the doped a-Si:H layers, which act as hole and electron selective carrier contacts (the emitter and the back/front surface field) compared with traditional diffused junction cells that have higher Auger recombination rates and accordingly lower V_{OC} because of the highly doped contact regions. The use of such layers in heterojunction cells has other technological advantages, including low processing temperatures (below

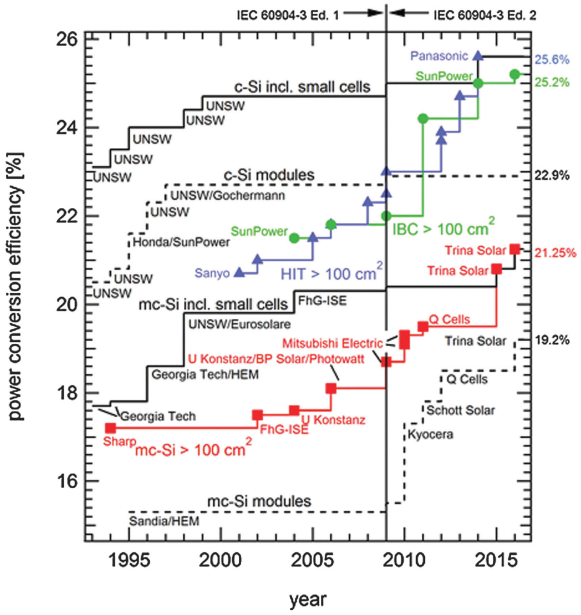

Figure 1.2: Evolution of the energy conversion efficiencies of various silicon PV technologies according to entry year in the tables of ref. [1]

200°C) that result in lower thermal budget [9], and the ability to deposit a-Si over large areas with high growth rates using plasma-enhanced chemical vapor deposition (PECVD), owing to the geometrical one dimensional nature of the free alignment architecture of this technology [10].

However, there are still many challenges remaining with high efficiency SHJ cells and the physics behind this technology has not been extensively investigated. These challenges mainly affect the cell IV characteristics at its maximum power point (MPP) and not necessarily at V_{OC} which has been the main concern with diffused junction solar cells.

Low performance at the MPP could be related to the selective collection of positive and negative charges at two spatially separated terminals. Cuevas et al, and Wurfel et al. specify that an electron selective contact must have the following properties: 1) the voltage drop produced by the electron current towards the electron

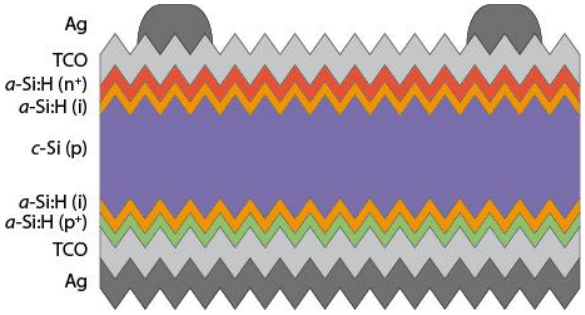

Figure 1.3: Sketch of a typical SHJ solar cell.

contact needs to be less than a few millivolts to maintain high fill factor (FF) and 2) the hole current towards the electron contact must be negligible [11, 12]. The same can be said for the hole contact by replacing the word hole for electron. These conditions are realized when, as described by Cuevas, et al., a contact: 1) has a high conductivity for one of the carriers and 2) a large asymmetry in the conductivities of the two carriers; the conductivity of the minority carrier must be low [13].

Doped amorphous silicon layers (p-type and n-type a-Si:H) deposited on top of the intrinsic a-Si:H layers (see Fig 1.3) are currently applied to provide contact selectivity for both electrons and holes [14]. This allows for very high V_{OC} of over 750 mV that are only about 10 mV below the upper theoretical limit for a high-quality crystalline silicon absorber [15]. However, this does not guarantee a perfect selectivity at the MPP. In fact, the carrier selectivity of doped a-Si layers can be further improved, first by quantitative evaluation of the contact resistances at the interfaces of these thin films [16, 17], and then by applying alternative contact materials such as metal oxides, mostly adopted from organic electronics [18, 19].

Parasitic absorption and low lateral conductivity in thin a-Si:H layers can also lead to low performance at the MPP [20] by increasing the total cell series resistance. Lateral conduction can be obtained by growing a transparent conductive oxide layer on top of the doped a-Si:H layers. In fact, employing TCOs results in an optically

transparent electrode that allows photons into the solar cell, and then transporting the photo-generated electrons to the external device terminals [21]. Accordingly, beside the requirement for high lateral conductivity, TCO layers should have very low UV-IR absorption because they are deposited both on the front and back sides of the solar cell. Therefore, specifically in the near IR region, layers with high mobility but lower carrier densities are preferred in order to maintain high conductivity while avoiding parasitic absorption [22].

1.2 Research objectives

The objective of this thesis is to achieve a detailed understanding of the loss mechanisms in SHJ solar cells. The cell operating principles and what affects cell operation, e.g. the IV characteristics at the MPP and correspondingly FF are investigated. Different sources of loss are analyzed separately, and the weight of each in the total loss at the MPP are evaluated. The total series resistance is measured and compared with the value obtained through summation over each of its components. The series resistance losses due to recombination, vertical and lateral carrier transport, metalization, etc., are individually evaluated and then by adding all these components together, the total loss is calculated. The concept of the fill factor and its direct dependence on the loss mechanisms at the MPP of the device is explained and its sensitivity to nearly every processing step of the cell fabrication is investigated. This analysis provides a framework for identifying the main source of losses in SHJ solar cells and pave the path for further improvement in the cell efficiency.

The main points can be summarized as follows:

- We provide a detailed understanding of the FF concept; we explain how it can be directly measured; how it can be calculated and what expressions can better approximate its value and under what operating conditions. The relation between

the $FF$and the cell operating conditions at the MPP are investigated.

- We separately analyze the main sources of FF loss including recombination, sheet resistance, contact resistance and metalization.

- We study FF loss due to recombination and its corresponding components including Auger, radiative and SRH recombination.

- We study FF loss due to contact resistance and its constituents including the contact resistance of different interfaces, e.g. between the intrinsic and doped a-Si layers, the TCO and the a-Si layers.

- We study FF loss due to lateral transport and its separate components including the TCO sheet resistance, the finger and busbar resistances.

1.3 Outlines

This thesis is divided into the following chapters:

In Chapter 2 we review the theory and physics behind solar cells and explain their IV characteristics. Then the concept of fill factor is discussed in more detail and it's relation with the cell operating condition at the MPP is illuminated. Specifically, we explain what the difference is between the actual, pseudo and implied FF and how each of them can be measured, calculated or approximated.

In Chapter 3, after further analysis of the fill factor concept, the approximate expressions proposed by Green, Swanson and Sinton to predict the FF of a solar cell from its V_{OC} is discussed. The expressions were originally suggested for silicon solar cells that behave according to a single-diode model and, in addition to V_{OC}, they require an ideality factor as input. They are now commonly applied to silicon cells by assuming a unity ideality factor-even when the cells are not in low-level injection- as well as to non-silicon cells. Here, we evaluate the accuracy of the expressions in

several cases. In particular, we calculate the recombination-limited FF and V_{OC} of hypothetical silicon solar cells from their simulated lifetime curves, and compare the exact FF to that obtained with the approximate expressions using assumed ideality factors. Considering cells with a variety of recombination mechanisms, wafer doping densities, and photogenerated current densities reveals the range of conditions under which the approximate expressions can be used accurately. We find that the expressions are unable to predict FF generally.

In Chapter 4, the front transparent conductive oxide (TCO) layers of silicon heterojunction solar cells are discussed and we examine how the IV characteristics, and specifically FF, are affected by the TCO. We investigate how to optimize TCO layers electrically and optically to minimize losses due to sheet resistance and free carrier absorption. We study TCOs for different wavelength ranges: $300-1200\ nm$ (full sun)and $700-1200\ nm$ (half sun). The latter is required if the silicon cell were to be used in a tandem structure as the bottom cell. Here, we demonstrate a procedure for determining the total loss associated with the front TCO layer, and employ it to determine which carrier density, mobility, and finger pitch combinations minimizes loss.

In Chapter 5, series resistance in SHJ cells is investigated, which is the main source of performance degradation for SHJ cells will be studied. Until recently, little has been done to understand the main factors contributing to the high resistance. Here we begin a systematic analysis to determine the important interactions between the different layers in the hole-collecting contact consisting of a stack of a-Si:H(i)/a-Si:H(p)/ITO/Ag. We attempt to address how the stack performs when the intrinsic and doped amorphous silicon layers thickness are varied, how the work function of the ITO - varying by the oxygen concentration - can affect the contact resistance at

it's interface with the a-Si layer and what it's contribution to total series resistance loss is. We also determine how the thickness affects the fill factor of the cell and assess how much loss is due to the contact resistivity.

In Chapter 6 we summarize the main finding of this thesis and give an outlook for future work.

Chapter 2

Concept of fill factor for silicon solar cells

2.1 Recombination mechanisms

The fundamental recombination mechanisms that can occur in silicon solar cells include:

- Radiative recombination
- Auger recombination
- Defect recombination

In the above, surface recombination is not introduced as a separate mechanisms because it is a particular case of the the third process; the discontinuity at the surface of crystalline silicon results in high number of dangling bonds that create a large number of defects within the bandgap. Recombination through these surface defects is basically very similar to that of bulk defects, and can be represented by similar physical models.

2.1.1 Radiative recombination

Radiative recombination occurs when an electron from the conduction band state falls into a vacant valance band state. The excess energy will then be released as a photon with an energy close to that of the bandgap. The corresponding lifetime expression for radiative recombination is

$$\tau_{\text{rad}} = \frac{1}{B(p_0 + n_0) + B\Delta n} \tag{2.1}$$

in which, B is the radiative coefficient [23], Δn is the excess carrier density, and n_0, p_0 are the equilibrium electron and hole densities. Depending on the illumination level, one of the terms in the denominator of the above expression will play the dominant role. Under high level injection, Δn is much larger than $(p_0 + n_0)$ and the first term

is dominant. Under low level injection, $(p_0 + n_0)$ is much larger than Δn, so the second term is dominant. In general, however, for crystalline silicon, the radiative lifetime is relatively low mainly due to its indirect band gap; for any single radiative recombination event to conserve both energy and momentum, one or more phonons are needed as well, that has inherently a low probability of occurring. The factor B in the above expression reflects this phenomenon. From detailed balance considerations, the value of B is calculated to be 9.5×10^{-15} $\mathrm{cm^3 s^{-1}}$ [24, 25].

2.1.2 Auger recombination

Auger recombination occurs when an electron and hole recombine, but unlike radiative recombination, the excess energy is transferred to a third free electron or hole. The charge carriers involved are assumed to be non-interacting quasi-free particles. For Auger recombination, there are always three free carriers involved and, because of that, its probability of occurring is higher for higher carrier densities, e.g. in highly doped material or for high injection conditions. The most recent parametrization for Auger recombination was introduced in Ref [26], which also applies the theory of Coulomb-enhanced Auger recombination. We discuss that in more detail in the next chapter. Here, we just provide a simple expression that more clearly depicts the dependency of Augur recombination on carrier density,

$$\tau_{\text{Augur, li}} = \frac{1}{C_n N_{\text{dop}}^2} \ , \ \tau_{\text{Augur, hi}} = \frac{1}{(C_a)\Delta n^2} \tag{2.2}$$

where C_n and C_a are the respective ambipolar Auger coefficients [27] and N_{dop} is doping density. As seen, for high doping densities or illumination level, the rate of Auger recombination increases.

2.1.3 Defect recombination

Semiconductor materials are not perfect, they always include defects. These defects can be a result of impurities within the bulk of the material or due to the disruption

of the perfect crystal at the surface. In both cases, these defects provide a site for an electron or hole to be trapped by an energy state in the forbidden region (bandgap). Trapped carriers in these states have the chance to recombine with an opposite type of carrier. Recombination through defects, also called Shockley-Read-Hall or SRH recombination, is parametrized for the bulk and surface of a crystalline silicon as follows [28, 29].

2.1.3.1 Bulk defects

The SRH lifetime for bulk defects can be expressed as

$$\tau_{\text{SRH}} = \frac{\tau_{n0}(p_0 + p_1 + \Delta n) + \tau_{p0}(n_0 + n_1 + \Delta n)}{(n_0 + p_0 + \Delta n)} \tag{2.3}$$

in which

$$n_1 = N_C exp(\frac{E_t - E_C}{k_B T}) \ , \ p_1 = N_V exp(\frac{E_C - E_g - E_t}{k_B T}) \tag{2.4}$$

In the above, n_1 and p_1 are the SRH electron and hole densities, E_c and E_v are the energies of the conduction and the valence band edges, E_t is the energy of the trap, N_c and N_v are the effective densities of states in the conduction and the valence bands, and k_B and T have their usual meanings.

As shown in above expression, the SRH lifetime is a function of the carrier injection level and the dopant density, as well as the defect trap density, their energy levels and their capture cross-sections. The rate at which a carrier moves into an energy level in the forbidden gap depends on the distance of the energy level from either of the band edges. Therefore, if an energy level is introduced close to either band edge, recombination is less likely as the electron (hole) is likely to be re-emitted to the conduction (valance) band edge rather than recombine with a hole (electron) which moves into the same energy state from the valence (conduction) band. For this reason, energy levels near mid-gap are very effective for recombination. Specifically,

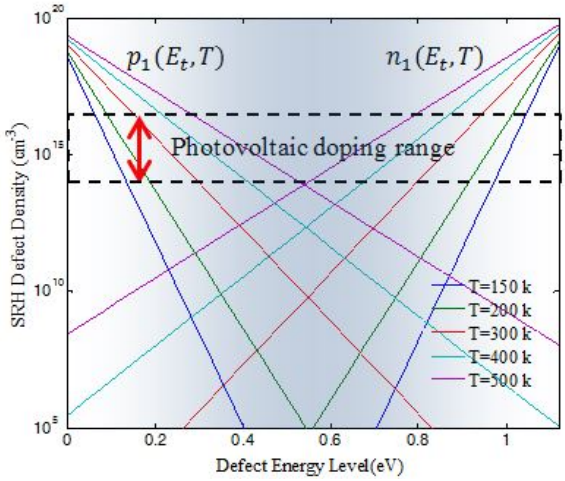

Figure 2.1: Dependence of the SRH densities n_1 and p_1 on the energy level E_t measured from the valence band edge for different temperatures (solid lines) at $300K$. To allow for a direct estimation of their magnitude, the doping region relevant for photovoltaic applications is marked by the dash line and the depth of the defect energy level is denoted by the blue color gradient.

for the case of deep defect levels close to midgap, as the SRH densities n_1 and p_1 become equal by definition to the intrinsic carrier density $n_i = 10^{10}\text{cm}^{-3}$, and so substantially smaller than the doping concentration and Eq. (3.2) simplifies for p-type doping to τ_{n0} and for n-type doping to τ_{p0}. Thus, in the limiting case of low level injection, recombination through deep level states is limited by the capture of minority carriers. Figure 2.1 shows the SRH defect densities as a function of defect energy level and temperature. As explained, for mid gap trap states, n_1 and p_1 drop significantly. As the temperature increases, however, the dependency of the defect densities on their energy level decreases; higher temperatures allow carriers need to jump between larger energy separated states.

2.1.3.2 Surface defects

Termination of the crystal at the surface of the silicon substrate leads to large numbers of partially bonded silicon atoms, which give rise to many dangling bonds, and therefore a large density of defect levels that are found within the bandgap near the

semiconductor surface. The SRH analysis classified above can apply if we reformulate it in terms of recombination events per unit surface area, rather than per unit volume. The surface recombination lifetime for a single defect can expressed as [30]

$$\tau_S = \frac{n_S p_S - n_i^2}{\Delta n(\frac{n_S+n_1}{S_{p0}} + \frac{p_S+p_1}{S_{p0}})} \tag{2.5}$$

where n_s and p_s are the concentrations of electrons and holes at the surface, and S_{n0} and S_{p0} are related to the density of surface states per unit area, N_{ts}, and the capture cross-sections, σ_p and σ_n, for the specific defect

$$S_{n0} = \sigma_n \nu_{th} N_{ts} \ , \ S_{p0} = \sigma_p \nu_{th} N_{ts} \tag{2.6}$$

where ν_{th} is the thermal velocity. As can be concluded from the above expressions, the main mechanisms that result in a reduction of surface recombination include: a) chemically passivating the dangling bonds and reducing their densities and capture cross section values by growing silicon oxide, silicon nitride or a-Si:H, b) reducing the surface concentration of electron or holes that can be achieved by doping the semiconductor surface to repel one type of carriers, e.g. electrons for a p-doped emitter or holes for a n-doped emitter. Fixed charges in an overlying dielectric can be used alternatively to create this electric field and repel one type of carriers [31]. In reality, the reduction of surface recombination in SHJ cell technology takes advantage of both of these mechanisms to some extent.

2.1.4 Effective lifetime

All the recombination mechanisms discussed above may contribute in silicon. Under different conditions, different recombination mechanisms may be dominant, however. For high quality crystalline silicon, bulk recombination is negligible. Under high injection levels or for wafers with high doping density, Auger is dominant. Surface recombination could be the dominant mechanism in cases where the passivation quality

is poor, e.g. growing a III/V material on Si as a passivation layer. Radiative recombination is in most cases negligible due to the indirect bandgap of silicon. The effective lifetime is given by

$$\frac{1}{\tau_{eff}} = \frac{1}{\tau_{rad}} + \frac{1}{\tau_{Aug}} + \frac{1}{\tau_{SRH}} + \frac{1}{\tau_{surf}} \tag{2.7}$$

.

2.2 IV characteristics and diode equation

2.2.1 I-V characteristics

To determine the I-V characteristics of silicon solar cells limited by the recombination mechanisms discussed above, the following approach, introduced in ref. [7, 32], can be followed. This approach models zero-resistance ideal cells, without perfect front-side antireflection coatings, reflecting rear mirrors and metalization. The current-voltage characteristic can be expressed as

$$J = J_L - qWR \tag{2.8}$$

where J_L is the photo-generated short circuit current, W the cell thickness, R the recombination rate (including radiative, Auger and defect recombination), and q the elementary charge. Obtaining effective lifetime value, τ_{eff} (see Eq (2.7), the recombination rate at each specific carrier density can be calculated through following expression

$$R = \frac{\Delta n}{\tau_{eff}} \tag{2.9}$$

Under the assumption of a narrow base, the change of the quasi-Fermi levels within the base are very small, and the quasi-Fermi level separation can be considered to be constant. When additionally assuming ideal contacts, the quasi-Fermi level separation equals the cells output voltage, V, and thus the excess carrier density, Δn is related to V by [33]

$$(n_0 + \Delta n)(p_0 + \Delta n) = n_{i,eff}^2 exp(\frac{qV}{k_B T}) \tag{2.10}$$

where the electron and hole equilibrium concentrations are n_0 and p_0. In (2.10), it is assumed that bulk series resistance losses are negligible; this is a valid assumption for cells operating under high illumination levels or with highly doped silicon wafers.

As seen in Eqs (2.9) and (2.10), both the current and voltage can be calculated versus excess carrier density. So, by sweeping the excess carrier density, the IV characteristics can be obtained. The quasi-Fermi level separation has its highest value at open circuit where there is no current flow, and the photo-generated voltage is limited by recombination processes. When current is flowing, e.g. at the MPP, carriers are extracted and so the gap between the Fermi levels decreases and the voltage drops. The Fermi-level gap separation decreases up until short-circuit conditions for which it becomes zero. Under this condition, photogenerated carriers will be ideally extracted from the absorber without loss.

2.2.2 Diode equation

The above parametrization can be applied for cases in which the carrier lifetime is well known; It is difficult for materials with bulk lifetime ranges of below $1\mu s$. Even for high quality silicon wafers, lifetime measurements are not practical after the final metalization steps. To calculate the IV characteristics under these conditions (the lifetime is difficult to measure directly), we may use the more traditional representation of the diode physics. Solar cells, like any other diode which includes a rectifying p-n junction, can be modeled with a diode equation (in the dark). Under illumination, however, the I-V curve shifts as the cell begins to generate power. As the light intensity increases, the upward shift increases as well. Since the cell is generating power, following the usual convention, we invert the current axis. The diode expression under illumination can be written as

$$J = J_L - J_0(exp[\frac{qV}{nkT}] - 1) \tag{2.11}$$

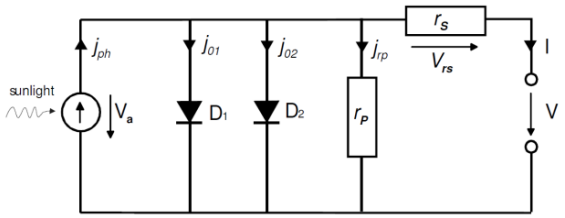

Figure 2.2: Schematic equivalent circuit diagram of a solar cell based on the two diode model

In the above parametrization, J_0 represents the recombination current. The recombination current itself can be divided to two different factors; one represents the intrinsic recombination (Auger and radiative), J_{01}, mostly dominant under high injection levels while the other represents bulk and surface defect recombination,J_{02}, mostly dominant under low injection levels. The solar cell operation condition can also be modeled by another parameter named the ideality factor, n, which represents how closely the solar cell operation is near to that of ideal diode behavior. In the two diode model, the ideality factor also can have different values; n_1 represents ideality factor under high level injection, and has values between 0.7 and 1. n_2 represents the ideality factor under high injection and depending on the defect density and surface passivation can have values 2 or above. The concept of ideality factor for solar cells and its limitations will be discussed in more details in Chapter 3. In reference [34], an expansive study of ideality factor dependency to Δn is provided. In addition to the recombination mechanism parameters, every solar cell has a series resistance, R_s (see Chapter 4 and 5) and shunt resistance, R_{sh}, which can be also included in the diode expression. The schematic of the above two diode model is shown in Fig 2.2. The corresponding expression is as follows

$$J = J_L - J_{01}(exp[\frac{q(V + JR_s)}{n_1 kT}] - 1) - J_{02}(exp[\frac{q(V + JR_s)}{n_2 kT}] - 1) - \frac{V + JR_s}{R_{sh}} \quad (2.12)$$

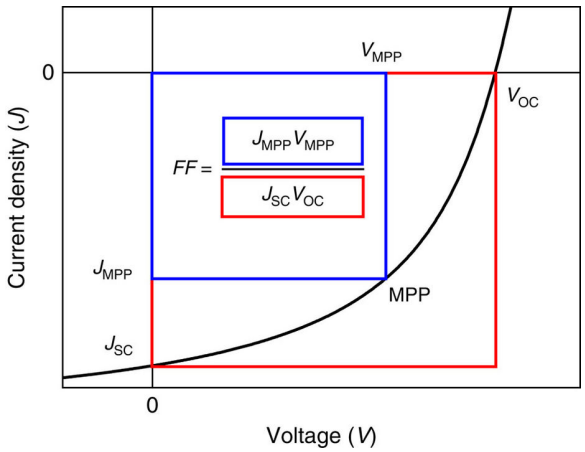

Figure 2.3: Output current as function of voltage. Also shown are the cell short-circuit current (J_{SC}) and open-circuit voltage (V_{OC}) points, as well as the maximum power point (V_{mpp}, J_{mpp}).

2.3 Loss mechanisms

The fill factor is the ratio of the product of the voltage and current at the MPP to the product of the open circuit voltage and short circuit current which are the key parameters in evaluating the performance of solar cells (see Eq 2.13). Graphically, the FF is a measure of the "squareness" of the solar cell IV curve, and is also the ratio of the area of the largest rectangle which will fit in the IV curve formed by $V_{\mathrm{OC}}$and J_{SC} (from PVCDROM [35]). In fact, we can calculate the fill factor by dividing the area of the smaller(dashed) rectangle to the larger(solid) rectangle in Fig. 2.3

$$FF = \frac{V_{mpp} J_{mpp}}{V_{oc} J_{sc}} \tag{2.13}$$

Series resistance, shunt resistance and additional recombination currents can strongly affect the fill factor of silicon wafer based solar cells. For cell process optimization, we need to determine and evaluate sources of each of these loss mechanisms. A good understanding of the physics behind these losses and a methodology to quantify, and then approximate these loss the sources is needed accordingly. In the next sections, using the equivalent diode equation, we briefly provide an approximate description

of the dependency of FF to each of above parameters in brief and then in the next chapters in more details we will discuss in more details both theoretically and experimentally the contribution of each separate factor to the fill factor.

2.3.1 Fill factor loss due to recombination

For silicon solar cells, it is now common to calculate the fill factor in the absence of external series resistance (the so-called pseudo fill factor, pFF) from Suns-V_{OC} measurements [36] (see Section 2.3.5), and to use this value as an upper limit against which the often varying actual FF can be compared [37]. In particular, suns-V_{OC} measurements give the series-resistance-free voltage at the MPP, across the contacts, from which the series resistance can be calculated [38], and the quasi steady state photoconductivity (QSSPC) or quasi steady state photoluminescence (QSSPL) measurements give the internal voltage at the MPP from which the voltage drop across the contacts can be calculated [39]. From these measurements, the loss on FF and V_{OC} of the device imposed by recombination in the quasi-neutral bulk and at the two cell surfaces is readily accessible, which sets a practical upper limit for the FF and V_{OC} of crystalline solar cells operating under high and low injection. We call this recombination limited FF (or V_{OC}) the internal (or implied fill factor (or V_{OC}), abbreviated by iFF (or iV_{OC}) [40]. The weight of this upper limit in the total loss is becoming increasingly significant specifically due to the recent improvements, e.g. lowering the contact resistances in SHJ solar cell operation conditions. Accordingly, as our attention is directed towards the recombination sources of FF loss, a well detailed evaluation and differentiation between SRH, surface and intrinsic recombination loss contributions to the fill factor becomes more demanding. That is, we would like to resolve the iFF (or iV_{OC}) into recombination factors that are intrinsic to the absorber bulk, e.g. radiative and Auger recombination, and those that can be engineered out, e.g. SRH and surface recombination. We will discuss and analyze in detail the FF

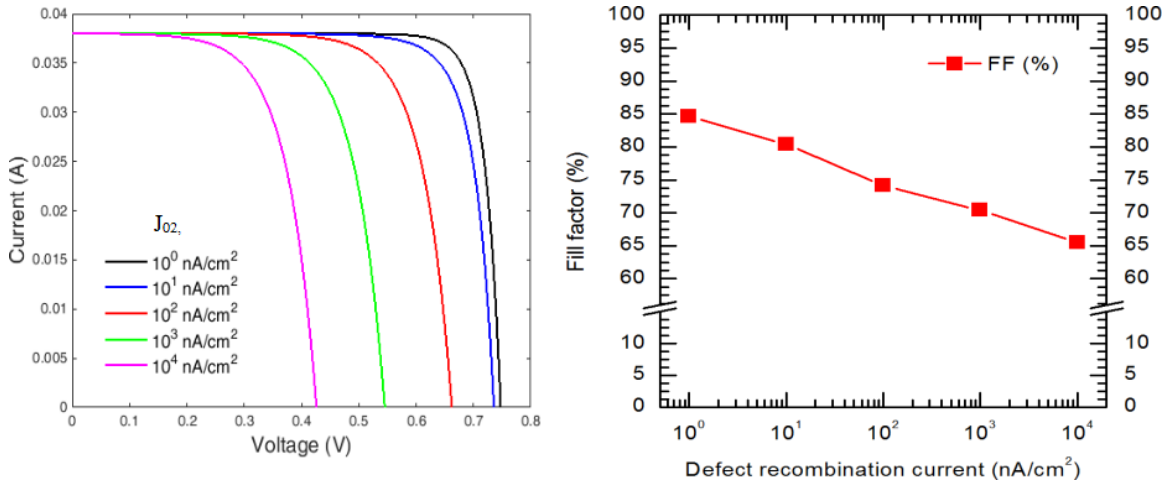

Figure 2.4: IV characteristic dependency to SRH recombination current, J_{02} (a) and extracted FF (b).

loss due to recombination in chapter 3 of this thesis. As seen in Eq (2.12), intrinsic recombination mechanism can be represented by J_{01} while defect recombination can be represented by J_{02} parameters in the two diode model approximation. Figure 2.4 shows how the maximum power point and accordingly FF is affected by J_{02}.

2.3.2 Fill factor loss due to shunt resistance

Shunt resistance can play a significant role in the performance of solar cells, and can be one of the sources of fill factor loss. Ideally, shunt resistance should have an infinite value; however, specifically for thin film silicon solar cells, its value decreases and leads to lower current flow through the load due to leakage current that in most cases is the result of the formation of cracks. Current channels through parallel paths will ultimately be lost as heat which increases the cell operating temperature, which can be further detrimental. Beside degrading the solar cell performance, low shunt resistance makes optimization of solar cells difficult because it masks other characteristic information such as the recombination currents, J_{01} and J_{02}, and the ideality factors n_1 and n_2. To study specifically the effect of shunt resistance on fill factor, we may vary the R_{sh} parameter in the two diode model expression, assuming

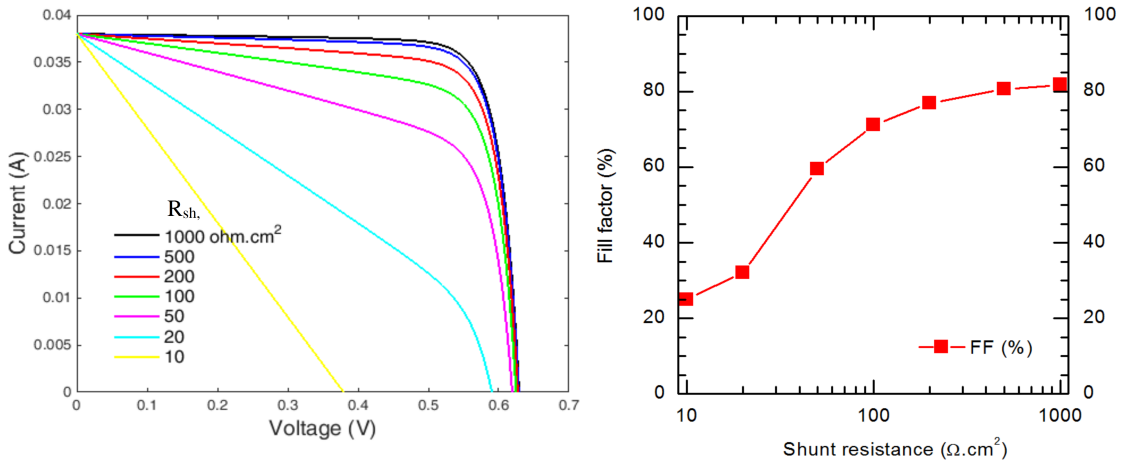

Figure 2.5: IV characteristic dependence on the shunt resistance, R_{sh} (a) and the extracted FF (b).

there is no loss due to series resistance. The IV characteristics obtained and the resulting FF are shown in Fig. 2.5.

For interdigitated back contact (IBC) solar cells, another type of shunting can occur which is different from conventional front-collecting-junction solar cells. Such shunting can be due to lithography related defects at the metal separation, or some laser-processed features along with possible edge effects associated with the perimeter of the laser-doped regions. To avoid this shunting losses, a thick, possibly multi-layer dielectric can be deposited to isolate the hole and electron contacts from each other [41, 42].

For non-IBC, front-collecting-junction solar cells SHJ cells (the main point of the present study) for which high quality n-type wafers are used, the defect density is low and shunting paths through the wafer are all blocked. Accordingly, very high values of shunt resistance are measured, that result in insignificant loss of fill factor. Therefore, in rest of this work, we have not investigated shunting losses assuming they are negligible.

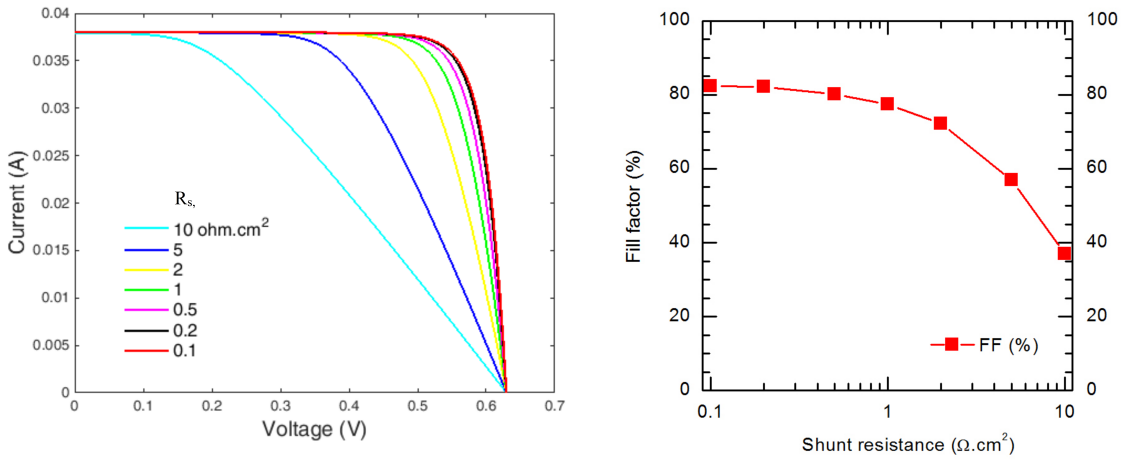

Figure 2.6: IV characteristic dependency to series resistance R_S(a) and extracted FF (b).

2.3.3 Fill factor loss due to series resistance

Series resistance is another parameter that can significantly affect the performance of solar cells and lead to a decrease in fill factor. Series resistance does not normally affect the open circuit voltage of silicon solar cells, because at that point no current is flowing through the device. However, at voltages near open circuit, e.g. at maximum power point, high series resistance values can have a very detrimental effect on the performance. To study specifically the effect of series resistance on fill factor, we may vary the R_S parameter in (2.12), assuming there is no loss due to shunt resistance. The resulting IV characteristics and corresponding FF are shown in Fig. 2.6. There are two types of series resistance that should be distinguished from another; 1) series resistance under illuminated conditions [43], and 2) series resistance under dark conditions [44]. Current may flow differently under each condition; under illumination, we have photo-generated carriers almost homogeneously all over the entire cell area which result in a relatively large lateral current toward the contacts, so a higher series resistance loss compared with dark conditions, since the current is specifically

limited to flow through the screen fingers and bus-bars. For SHJ solar cells that are operating in a tandem structure and as the bottom cell, the illumination level decreases almost by half of that in a single junction cell under one-sun illumination, which correspondingly leads to lower lateral current. This effect will be studied in more detail in Chapter 4.

Different methods to determine the lumped series resistance, R_{S} of solar cells is suggested in the literature and are well discussed and compared in Ref. [37]. The most reliable and prevalent ones are illumination intensity variation [45], the comparison of a Suns-V_{OC} with a one-sun IV-curve [46], and the modified comparison a one-sun IV-curve with the dark IV-curve method [47]. In this work, we have used the comparison of the Suns-V_{OC} with a one-sun IV-curve to investigate the series resistance loss. This method is specifically applicable to the Si solar cell industry for which Suns-V_{OC} can be measured at the early stages of device processing.

Beside losses due to metalization that can be easily measured, series resistance can have two other sources of losses that are more complicated and less investigated. These main loss sources for fill factor are introduced in the next two subsections and will be analyzed extensively in Chapters four and five of this thesis. A schematic of the cell is provided in Fig. 2.7, that beside highlighting the necessity for lateral transport in TCO layers, illustrates the different layers and their interfaces in SHJ cells.

2.3.3.1 Sheet resistance loss

Sheet resistance in SHJ cells is due to the need for lateral current transport. A transparent conductive oxide is sputtered on top of the doped a-Si:H layers on the front side of the SHJ cell to provide this transport path. The sheet resistance can be

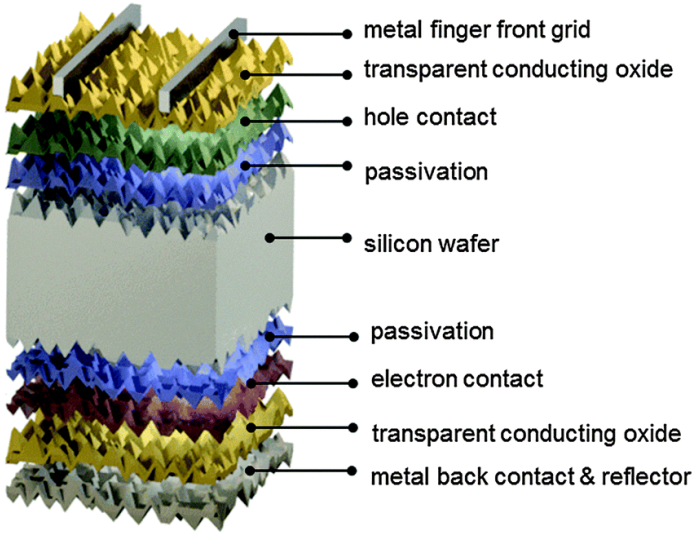

Figure 2.7: Schematic of SHJ solar cells (borrowed from [2]).

calculated through following expression,

$$R_{sh} = \frac{1}{e\mu nt} \tag{2.14}$$

Here, e is the electronic charge and μ, n, and t are the TCO electron mobility, free electron density, and thickness, respectively. To decrease the sheet resistance and resulting fill factor loss, we can adjust three parameters. First is the thickness that is fixed to 65-80 nm for SHJ cells under one-sun illumination because the front TCO should also serve as an anti-reflection layer. For SHJ cells that are used in a tandem structure and are illuminated by wavelength ranges between 700-1200 nm due to the assumed absorption in the top cell, this thickness can be fixed to 100-110 nm to again minimize the reflection at this specific range. From above expression, its clear that for higher thicknesses (e.g. the TCO for a SHJ cell in a tandem structure), the sheet resistance is smaller which means the TCO layer is less electrically constrained. The other parameter that can decrease the sheet resistance is the carrier density. However, higher values of carrier density lead to higher parasitic absorption. So, its value should be kept as small as possible. The final adjustable parameter in

Eq (2.14) is the mobility, which offers the only way to decrease the sheet resistance without compromise, yet it is the most difficult to control in practice [48].

It is worthwhile to mention that in SHJ cells, an inversion layer is present at the front interface between a-Si and c-Si, that may help to decrease the sheet resistance as well. However, as demonstrated in Ref. [21], the contribution of the inversion layer to lateral transport is negligible; this is due to its low conductivity in this region compared with the TCOs. Carriers can just travel a few hundred microns in this inversion layer before recombination, which is not enough for screen printed front grids with finger spacing in the milimeter range. Increasing the valence band offset can make this layer more conductive; however, this also impedes transport across the barrier to the emitter.

2.3.3.2 Contact resistance loss

To understand how significantly the hole and electron contacts play in the total series resistance, we should first have a look at the band structure of SHJ cells as shown in Fig. 2.8 (borrowed from Ref. [3]). As seen, the silicon absorber is sandwiched between the intrinsic, doped a-Si:H and TCOs on each side. There is a contact resistance at the interface of each of these thin layers: between c-Si and the intrinsic a-Si:H, between the intrinsic a-Si:H and the doped a-Si, between the doped a-Si:H and the TCO, and finally between the TCO and the metal contacts which are basically determined by the Fermi-level and work function of each of these layers. Specifically, the a-Si:H work function must be high/low enough to induce the junction into the c-Si (green and red shaded dotted lines in figure 2.8). The work function can be tuned by changing the doping density. However, increasing the dopant atoms leads to an abundance of defects that may lower the doping efficiency significantly below the level of c-Si which can create a barrier for carrier transport and result in further resistance.

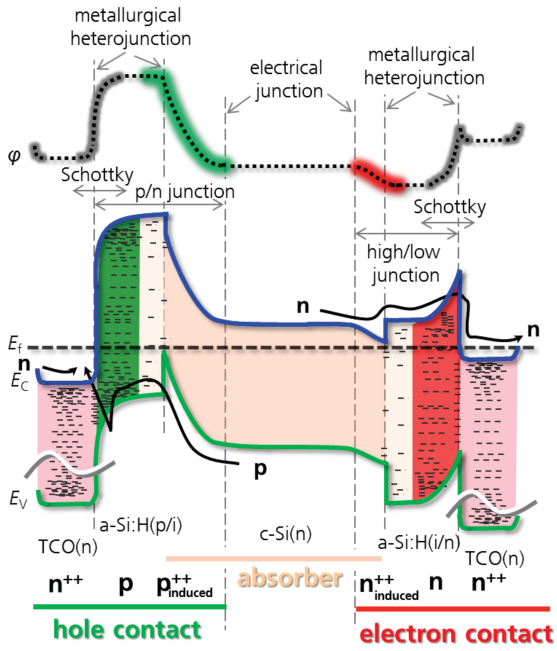

Figure 2.8: The equilibrium band diagram of the standard SHJ cells. It can be seen that the c-Si absorber is sandwiched between three thin films on each side, two a-Si:H films and one TCO. Similar films are applied to the front and rear with the only significant difference that the opposite doped a-Si:H film is used at either side. (from Ref.[3])

Another approach to tune the work function is by the alloying of the a-Si:H (see Ref. [49],[50]). Another function of doped a-Si is to provide a path for charge transport to the TCO. Again, a mismatch between the work function of the TCO and the a-Si:H layers lead to a parasitic band bending and an increase in contact resistance at this interface. With respect to the TCO, as discussed in previous section, their function is more than providing a good contact. In fact, an ideal TCO should have a low sheet resistance to provide good lateral transport for carriers. Moreover, it should be highly transparent and without any parasitic absorption. These two requirements limit our options in TCO materials and tuning their work-function to reach a minimum contact resistance. For further information on the concept, see Ref. [51]. In chapter five, we analyze the contact resistances between the above interfaces quantitatively.

2.3.4 Fill factor approximated expressions

Similar to the two common models introduced in Section 2.2 to simulate the IV characteristics of a solar cell, approximate models have been suggested to calculate the FF. Prior to the introduction of the Suns-V_{OC} technique, two approximate expressions were suggested by Green [38] and Swanson and Sinton [52] to predict the pFF from the V_{OC} of a silicon solar cell. These expressions are convenient because they allow one to, e.g., calculate the pFF of a cell reported in the literature without Suns-V_{OC} data or to use the implied open-circuit voltage (iV_{OC}) to gain insight into the FF in the early stages of cell processing (e.g., after passivation). However, the expressions proposed only explain the behavior of cells operating in low injection, for which the recombination rate is linear in the excess carrier density. Both expressions can be extended to higher injection by including a non-unity ideality factor. However, the formulas only use a single ideality factor as input, and, as ideality factor varies with injection level and is determined by the dominant recombination mechanism, it is not obvious which ideality factor to use. In recent years, these expressions, especially that proposed by Green have been occasionally used to calculate the FF without regard to the aforementioned limitations. The approximate empirical equation for the FF in terms of V_{OC} proposed by Green is shown below. Note that the series resistance and the shunt resistance are assumed to be zero and infinite, respectively.

$$FF = \upsilon_{oc} - ln\frac{(\upsilon_{oc} + 0.72)}{(\upsilon_{oc} + 1)} \tag{2.15}$$

in which

$$\upsilon_{oc} = \frac{V_{oc}}{mk_BT/q} \tag{2.16}$$

Swanson and Sinton derived a similar but less common expression for the FF in terms V_{OC} from a different starting point. These authors observed that, over a wide

range of conditions, the power of a solar cell evaluated at 95% of its J_{SC} is uncannily similar to the maximum power of the cell. Consequently, in the particular case in which the recombination rate is proportional to the excess carrier density, the excess carrier density at the maximum power point is 5% (a factor of 1/20) its value at open circuit. The output current and voltage at maximum power and finally fill factor are thus

$$J_{mpp} = 0.95 J_{sc},\ V_{mpp} = V_{oc} - (\frac{mk_BT}{q})ln(20) \tag{2.17}$$

$$FF = \frac{V_{mpp}J_{mpp}}{V_{oc}J_{sc}} = (1 - \frac{1}{20})\frac{\upsilon_{oc} - ln(20)}{\upsilon_{oc}} \approx \frac{\upsilon_{oc} - ln(20)}{\upsilon_{oc} + \upsilon_{oc}/20} \tag{2.18}$$

2.3.5 Fill factor measurement

One advantage of silicon solar cells technology is that different sources of losses and accordingly fill factor can be measured and separated at different stages of cell processing. Here, we introduce labels for the fill factor obtained at each stage and discuss the relevant measurement methods. Figure 2.9 summarizes above-mentioned losses in which:

FF_0 represents intrinsic fill factor. To obtain it, we assume there is infinite shunt resistance, no series resistance and that the bulk and surface defect recombination is ignorable. The only source of loss considered is intrinsic (Auger and radiative) recombination. Using the Auger and radiative recombination expressions obtained by Richter et al. [26] and applying the methodology introduced in Section 2.2, the IV characteristics and resulting FF_0 are calculated.

iFF represents the implied fill factor. To obtain it, we assume there is infinite shunt and no series resistance. However, beside intrinsic recombination, losses due to bulk and surface recombination are considered. In other words, all recombination mechanisms are taken into account. Similar to FF_0, iFF will be calculated applying

methodology introduced in Section 2.2. However, instead of using theoretical expressions, here, recombination is experimentally measured by applying photo-conductance technique using Sinton instrument lifetime tester. For further information regarding Sinton lifetime tester, see reference [26, 53]. Comparing iFF and FF_0, the fill factor losses due to defect recombination can be recognized and its role weighted over the whole FF loss can be determined.

pFF represents the pseudo fill factor. To obtain it, we assume there is infinite shunt and no series resistance. However, losses due to the formation of a reverse diode are taken into account which is the result of non-ideal carrier selectivity for holes and electrons at each surface. In fact, the hole and electron quasi- Fermi levels drop gradually as we pass through the selective layers on both sides of the cell and reach the surface. Therefore, the resulting V_{OC}, equal to the difference between electron and hole quasi- fermi levels, is actually smaller right at the contacts, compared with that in the bulk [51]. The pseudo-IV characteristics can then be calculated by varying the illumination level in discrete steps, and extracting V_{OC} for each. For further information regarding Pseudo IV measurement and the Sinton Suns-V_{OC} tester, see reference [54, 55]. Note that the Sinton Suns-V_{OC} tester does not include shunt resistance.

FF represents the actual fill factor. To obtain it, we consider all sources of losses including shunt, series, recombination and non-ideal carrier selectivity of the contacts. The actual FF is measured by the IV tester at the end of cell processesing i.e after metalization and all the annealing steps.

2.3.6 Fill factor excess carrier dependency

As demonstrated, the fill factor may be a good metric and well accepted parameter for all different solar cell technologies to evaluate the performance of a cell at its maximum power point. Here, we study how well the fill factor represents the working

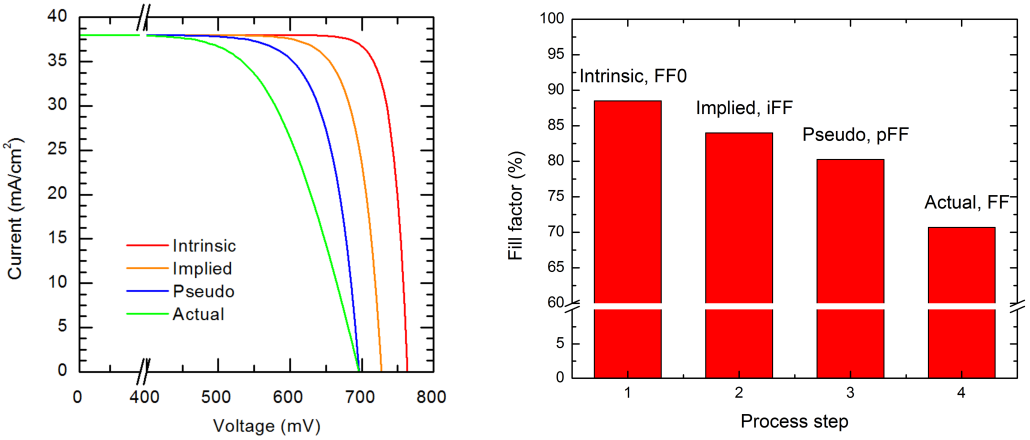

Figure 2.9: Summary of different fill factor loss mechanisms

operation condition at the maximum power point operation for silicon solar cells with different quality of bulk material and surface passivisation. Specifically, we compare the dependency of the fill factor with respect to the variation of both the illumination level, and the doping density. First, lets have another look at the FF expression once again and its relation to the voltage and current at the MPP and the efficiency.

$$Efficiency = \frac{P_{out}}{P_{in}} = \frac{V_{mpp} \times J_{mpp}}{P_{in}} = \frac{\frac{V_{mpp} \times J_{mpp}}{V_{oc} \times J_{sc}} \times V_{oc} \times J_{sc}}{P_{in}} \tag{2.19}$$

In the above expression, while the efficiency is just dependent on the voltage and current at the MPP, the FF is in fact determined by the ratio of the product of voltage and current at the maximum power point to the product of the voltage at open circuit and the current at short circuit. Under varying illumination levels, the carrier concentration is different, and accordingly, the dominant recombination mechanism may be different for a cell under operation at its MPP or its open/short circuit conditions. As a result, the FF may have different variation trends compared with the MPP operation condition alone due to its additional dependency to the open and short circuit operation conditions, which basically determines the efficiency. Figure 2.10 shows the variation of FF and $V_{\mathrm{mpp}}J_{\mathrm{mpp}}$derivatives versus photo-generated current

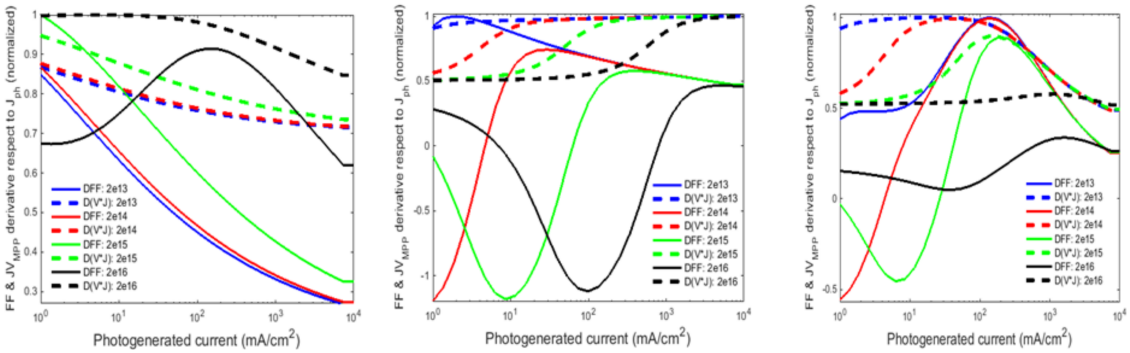

Figure 2.10: Variation of FFderivative (solid lines) and $V_{\mathrm{mpp}}J_{\mathrm{mpp}}$ derivative (dashed lines) versus photo-generated current for four different values of doping concentration assuming a) intrinsic recombination is the only existed recombination mechanism, b) SRH recombination is the only existed recombination mechanism and c) both intrinsic and SRH recombination mechanism are active.

for four different values of doping concentration assuming: a) intrinsic recombination is the only existing recombination mechanism, b) SRH recombination is the only existing recombination mechanism and c) both the intrinsic and SRH recombination mechanisms are active. We chose to study and compare the derivative trends of FF and $V_{\mathrm{mpp}}J_{\mathrm{mpp}}$because it can represent well the variation of these parameters. By having a closer look, it is clear that the two studied parameters are not necessarily sharing the same trends specifically in case (b) for which the SRH recombination is assumed to be the dominant recombination mechanism. The deviation between the two demonstrates that the fill factor may not be the best parameter to track the performance of solar cells at the MPP. For instance, figure 2.10 shows that for a silicon wafer with bulk doping density of $10^{16}\ cm^{-3}$, the fill factor slope of variation decreases as the photo-generated current varies from $10mA$ to $100mA$ while the $V_{\mathrm{mpp}}J_{\mathrm{mpp}}$ slope of variation increases.

Chapter 3

Recombination

As discussed in previous Chapter, the fill factor of a solar cell is sensitive to nearly every processing step during cell fabrication, and therefore tends to fluctuate across a batch and between batches of solar cells more than the open-circuit voltage V_{OC} or short-circuit current J_{SC}. For silicon solar cells, it is now common to calculate the fill factor in the absence of an external series resistance (the so-called pseudo fill factor, pFF) from Suns-V_{OC} measurements [36], and to use this value as an upper limit against which the actual FF can be compared (see Section 2.3.4). Prior to the introduction of the Suns-V_{OC} technique, two approximate expressions were suggested by Green [38] (see Eq 2.15) and Swanson and Sinton [52] (see Eq 2.16) to predict the pFF from the V_{OC} of a silicon solar cell (see Section 2.3.5). These expressions are convenient because they allow one to, e.g., calculate the pFF of a cell reported in the literature without Suns-V_{OC} data or to use the implied open-circuit voltage (iV_{OC}) to gain insight into the FF at the early stages of cell processing (e.g., after passivation) [36, 37, 40]. However, these expressions were proposed to explain the behavior of cells operating in low-level injection, for which the recombination rate is linear in the excess carrier density. Both expressions can be extended to higher injection by including a non-unity ideality factor. However, the formulas accept only a single ideality factor as input, and, as the ideality factor varies with injection level and is determined by the dominant recombination mechanism [34], it is not obvious which ideality factor to use.

In recent years, these expressions have been occasionally used to calculate FF without regard for the aforementioned limitations, especially that proposed by Green. In particular, the expressions have been applied for silicon cells under mid

to high injection and even for non-silicon solar cells including polymer, organic, dye-sensitized and multi-junction concentrator cells [14, 56–64]. In addition, regardless of the injection level and dominant recombination process(es), most often an ideality factor of 1 is assumed. In this Chapter, we investigate the accuracy of the FF approximations to understand the range of conditions for which they can safely be used. Meanwhile, it can provide a concrete understanding of which and how different variables will affect the fill factor, and so pave the way towards the next Chapters in which we mostly focus on evaluating, analyzing, designing and finally optimizing of parameters that determine the fill factor.

Here, our approach is to consider hypothetical solar cells with known recombination, from which we can calculate the effective lifetime of minority carriers. From the lifetime curves, we calculate the corresponding exact iV_{OC} and iFF, and compare the latter to the iFF computed with the approximate expressions using the exact iV_{OC}. We find that the deviations are significant whenever the incorrect ideality factor is assumed, and non-negligible even with the correct ideality factor. Along the way, we elucidate the dependence of V_{OC} and FF on the recombination mechanism, wafer doping density, and illumination.

3.1 Modeling

3.1.1 Calculation approach

For simplicity, we limit our analysis to solar cells on n-type silicon wafers, though it can be easily extended to p-type wafers. We begin by generating lifetime data for hypothetical silicon solar cells using recent models for intrinsic (radiative and Auger) [65] and bulk defect (SRH) recombination. We neglect surface recombination and assume perfect passivation for simplicity; intrinsic and bulk recombination turn out to be sufficient to evaluate the accuracy of the approximate FF expressions. Next, using the detailed balance model of Richter et al. [20], we compute current density-

voltage (J-V) characteristics from the lifetime data and find the exact FF and V_{OC} values for each hypothetical cell. We also extract the injection-dependent ideality factor from the lifetime using an expression developed by Hameiri et al. [34]. In select cases, the ideality factor of a cell at open circuit or at maximum power is then inserted, along with the exact V_{OC} of that cell, into the expression proposed by Green to find the corresponding approximate FFİn other cases, the injection dependence of the ideality factor is ignored and a value of 0.7, 1, or 2 is assumed. Finally, we compare the approximate and exact FF values and calculate the relative difference between them. Figure 3.1 shows this calculation approach schematically.

3.1.2 Lifetime curves

3.1.2.1 Intrinsic recombination model

We used the parametrization recently published by Richter et al. to model intrinsic recombination in silicon solar cells [26]. The model outputs the minority-carrier intrinsic lifetime as a function of excess carrier density. The main advantage of this model over previous models is that it considers the increased Auger recombination probability caused by the Coulomb interactions between electrons and holes. Radiative recombination within the Richter parameterization is based on the radiative coefficients measured by Trupke et al. [23], which are 50% smaller than those measured by Schlangenotto et al. [66], and as with Auger recombination, the effect of Coulomb interactions are included using the model introduced by Altermatt et al. [67]. The parametrization also considers the influence of bandgap narrowing on the effective intrinsic carrier density, which increases with doping and injection level [68, 69].

According to the Richter model, the intrinsic minority-carrier lifetime in silicon

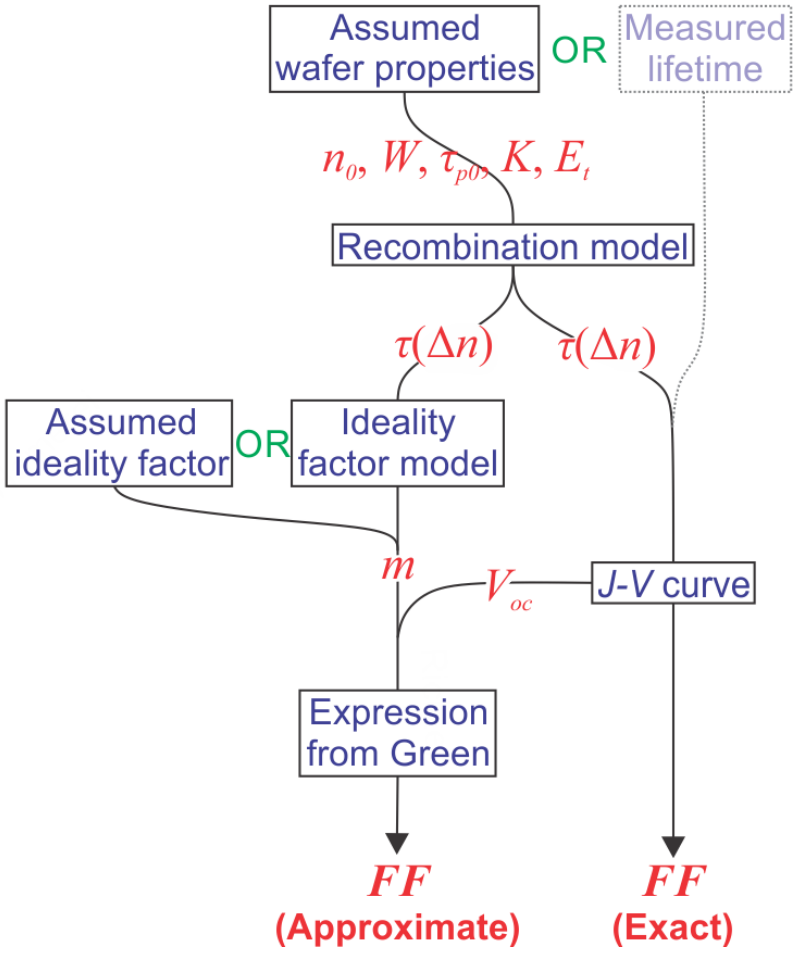

Figure 3.1: Illustration of the calculation approach used to find both the exact and approximate FF of a given hypothetical solar cell. Note that, though not done in the present work, measured lifetimes (dashed box) may be substituted for calculated lifetimes.

is given by

$$\tau_{intr} = \frac{\Delta n}{(np - n_{i,eff}^2)(2.5 \times 10^{-31} g_{eeh} n_0 + 8.5 \times 10^{-32} g_{ehh} p_0) + 3 \times 10^{-32} \Delta n^{0.92} + B_{rel} B_{low}} \tag{3.1}$$

with the Coulomb interaction enhancement factors

$$g_{eeh}(n_0) = 1 + 131 - tanh[(\frac{n_0}{N_{0,eeh}})^{0.66}] \quad , \quad g_{ehh}(p_0) = 1 + 7.51 - tanh[(\frac{p_0}{N_{0,ehh}})^{0.63}] \tag{3.2}$$

In these equations, n and p are the electron and hole densities, n_0 and p_0 are the equi-

librium electron and hole densities, $n_{i,eff}$ is the effective intrinsic carrier density, Δn is the excess carrier density, $B_{low} = 4.73 \times 10^{-15} cm^3 s^{-1}$ is the radiative recombination coefficient for lightly doped silicon in low injection [23], B_{rel} is the relative radiative recombination coefficient according to Ref. [67], and $N_{0,eeh} = 3.3 \times 10^{17} cm^{-3}$ and $N_{0,ehh} = 7 \times 10^{17} cm^{-3}$ are empirical constants.

3.1.2.2 Bulk-defect recombination model

A SRH model [28, 29] was used for recombination through bulk defect states. The SRH model consider a single trap level within the bandgap that has an assumed carrier capture behavior. The SRH model introduced by Rein et al. [70] gives the minority carrier lifetime in n-type silicon as

$$\tau_{SRH} = \tau_{p0}[\frac{n_0 + p_1 + \Delta n}{n_0 + p_0 + \Delta n} + K\frac{n_1 + p_0 + \Delta n}{n_0 + p_0 + \Delta n}] \tag{3.3}$$

In Eq 3.3, τ_{p0} is the equilibrium capture time constant of holes, given by

$$\tau_{p0} = \frac{1}{\sigma_p \upsilon_{th} N_t} \tag{3.4}$$

where σ_p is the capture cross section for holes, υ_{th} is the thermal velocity, and N_t is the defect density. The symmetry factor, K, in Eq 3.3 is characteristic of a defect and defined by the ratio of the hole and electron capture cross sections: $K = \sigma_p \sigma_p$. n_1 and p_1 are the SRH electron and hole densities, given by

$$n_1 = N_c exp(-\frac{E_c - E - t}{k_B T}) \quad , \quad p_1 = N_v exp(-\frac{E_t - E - v}{k_B T}) \tag{3.5}$$

where E_c and E_v are the energies of the conduction and the valence band edges, E_t is the energy of the trap, N_c and N_v are the effective densities of states in the conduction and the valence bands, and k_B and T have their usual meanings.

As shown in previous Chapter 2.1.4, Eq 2.7, the effective lifetime τ_{eff} can then be obtained from the intrinsic and SRH lifetimes by adding them in parallel.

Later, in Fig. 3.4, injection-dependent lifetime curves of silicon solar cells for intrinsic recombination, SRH recombination, and intrinsic and SRH recombination, will be shown and their relation with V_{OC} will be analyzed.

3.1.3 $J-V$ characteristics and exact FF

The approach introduced in Section 2.2.1 is used here to obtain the $J-V$ characteristics. This model was demonstrated recently by Richter [7], to assess the limiting efficiency of silicon solar cells in the absence of parasitic optical and electrical losses. We assume narrow-base conditions (the quasi Fermi levels are constant within the base), for which the quasi Fermi level separation is equal to the output voltage, given by

$$V = V_{jn} + V_{jp} = (\varphi_i - \varphi_n) + (\varphi_p - \varphi_i) = \frac{k_B T}{q} ln((n_0 + \Delta n)(p_0 + \Delta n)/n_{i,eff}^2) \quad (3.6)$$

where φ_i, φ_n and φ_p are the intrinsic Fermi potential, electron quasi-Fermi potential, and hole quasi-Fermi potential. Note that the narrow-base assumption is not valid when the minority-carrier diffusion length is comparable to or smaller than the wafer thickness (e.g., for low-quality multicrystalline wafers with $\tau_{p0} < 50\mu s$), a situation not encountered in this study. The output current of the solar cell is given by the difference between the generation and recombination current densities

$$J = J_{ph} - qW\Delta n/\tau_{eff} \quad (3.7)$$

where J_{ph} is the photogenerated current density, q is the electronic charge, W is the cell thickness, and R is the total recombination rate. For a given value of Δn, Equations 3.6 and 3.7 yield the output voltage and current of the solar cell (after τ_{eff} is calculated with Eq. 2.7); sweeping Δn thus results in a $J-V$ curve from which the FF can be determined.

3.1.4 Injection-dependent ideality factor

The approximate FF expressions require a single ideality factor m as input. Most often, a value is assumed or extracted from the J-V curve of a completed solar cell by fitting with a diode model. Here, in select instances, we used the formalism reported by Hameiri et al. [34] to calculate the ideality factor from the minority-carrier effective lifetime (expressed as the recombination rate) as a function of the excess carrier density

$$m = (\frac{1}{n} + \frac{1}{p})R\frac{d\Delta n}{dR} = \frac{2\Delta n + n_0}{\Delta n(\Delta n + n_0)}R\frac{d\Delta n}{dR} \tag{3.8}$$

3.2 Results

We begin by comparing the approximations introduced by Green and Swanson and Sinton. Figure 3.2 shows the FF calculated with the expressions for the commonly assumed ideality factors $m = 0.7, 1$, and 2. Despite their different origins and functional dependencies, the two expressions give very similar results, particularly for low-level injection ($m = 1$). For simplicity, we therefore investigate the accuracy of only the expression suggested by Green, and assume that any limitations encountered apply equally to the expression suggested by Swanson and Sinton in what follows. Furthermore, the approximate FF is hereafter used to refer to the FF values calculated with Greens expression (2.15). In assessing Eq 2.15, we consider a hypothetical solar cell exhibiting only intrinsic recombination, only SRH bulk recombination, or both mechanisms simultaneously. The first two cases are illustrative because they have well-defined limiting ideality factors under high and low injection, whereas the third is representative of a real solar cell with a mediocre bulk lifetime but excellent surface passivation. The third is likely also representative of a solar cell with excellent bulk lifetime but mediocre surface passivation (which we do not explicitly treat here)

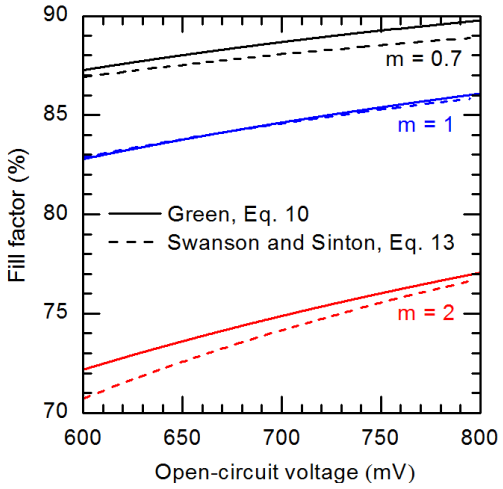

Figure 3.2: FF values calculated with the approximate expressions from Green and Swanson and Sinton for a range of typical V_{OC}s and ideality factors.

because surface recombination is also accurately modeled with the SRH formalism in most cases. Figure 3.3 shows the V_{OC}s calculated for these three cases using the methodology described in Section 2.2.1 for a $170\mu m$ thick solar cell. The data are displayed as a contour plot in which the wafer doping density and photogenerated current density are varied. These quantities were chosen for the axes because the doping density is the only variable parameter that influences the intrinsic lifetime (Eq 3.1) and is one of the few parameters that an ingot manufacturer can easily control; the photogenerated current density appears in Eq 3.7 and changes the excess carrier density at open circuit and thus the corresponding V_{OC}. In practice, the photogenerated current density changes over the course of a day, when placing a cell under concentration, or when using a silicon cell in a tandem. It also varies with wafer thickness, which is a suitable alternative x-axis variable for Fig. 3.3 if particular illumination conditions (e.g., $AM1.5G$) are assumed [7], though the two are treated independently in Eq 3.7. Doping density enters into the SRH lifetime (Eq. 3.3) in addition to the intrinsic lifetime, but so do several other parameters that characterize the assumed bulk defect. Throughout this paper, we assumed $\tau p_0 = 500\mu s$,

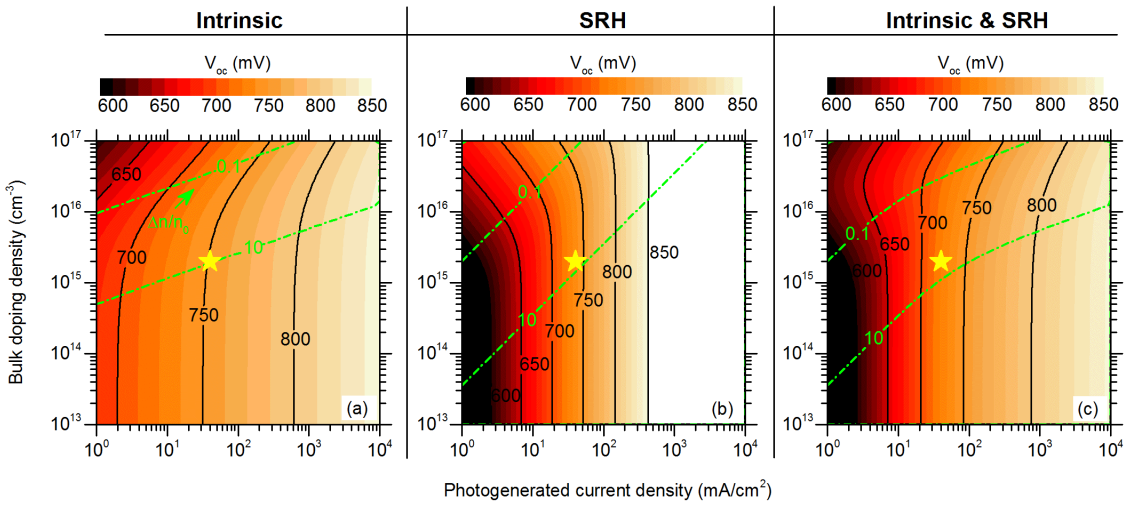

Figure 3.3: Exact V_{OC}s of silicon solar cells on n-type, 170μm thick wafers with varying doping density under varying illumination levels (photogenerated current densities). V_{OC}s are shown for cells with intrinsic recombination, SRH recombination, and intrinsic and SRH recombination in (a), (b), and (c), respectively. The color scale is the same for each plot. The dash-dotted green lines denote doping densities and photogenerated current densities for which n/n_0 is 0.1 or 10; these values are used to denote the boundaries of low injection (region above the upper green line) and high injection (region below the lower green line). The yellow stars correspond to a typical solar cell with a 2Ωcm n-type wafer under $AM1.5G$ illumination.

$K = 1$, and $E_t = 0.5eV$ (with $E_V = 0$). This hypothetical defect is representative of many real recombination-active defects in silicon (e.g., Mo, Cr, Ti, and Fe), which are near mid-gap and have near-unity capture cross section ratios [71–75]. In fact, the SRH lifetime changes little for $0.3eV < E_t < 0.8eV$ and $0.2 < K < 5$. τp_0 was arbitrarily chosen based on measured lifetimes in, e.g., high-quality multicrystalline or low-quality Czochralski wafers [76]. As Eq. 3.3 indicates, τ_{p0} simply scales the SRH lifetime. The intrinsic-recombination-limited V_{OC} (Fig 3.3a) and the SRH-recombination-limited V_{OC} (Fig. 3.3b) are both independent of doping density on high injection ($\Delta n > 10n_0$), but they have opposite dependencies on doping in low injection ($\Delta n < 0.1n_0$). We briefly digress to explore why. At open circuit, $J = 0$

and Eq. 3.7 can be rearranged as

$$\Delta n = \frac{J_{ph}\tau_{eff}}{qW} \tag{3.9}$$

Inserting this into Eq. 3.7 and noting that p_0 is negligible in n-type wafers yields an expression for V_{OC} that can be further simplified in low injection to

$$V_{oc} = C_0(ln(\frac{J_{ph}}{W}) + ln(n_0) + ln(\tau_{eff,oc})) + C_1 \tag{3.10}$$

and in high injection to

$$V_{oc} = 2C_0(ln(\frac{J_{ph}}{W}) + ln(\tau_{eff,oc})) + C_2 \tag{3.11}$$

where

$$C_0 = \frac{k_B T}{q}, \qquad C_1 = -\frac{k_B T}{q} ln(q n_{i,eff}^2), \qquad C_2 = -\frac{k_B T}{q} ln(q n_{i,eff}) \tag{3.12}$$

are constants and $\tau_{eff,oc}$ is the effective lifetime at open circuit. We first consider SRH recombination (Fig. 3.3b), which is the simpler of the two cases. Looking at Eq 3.3 and Fig. 3.4, in high injection the effective lifetime is independent of the photogenerated current density (or, specifically, Δn) and the doping density ($\tau_{SRH} = \tau_{p0}(1 + K) = 1ms$), and thus Eq 3.11 indicates that V_{OC} scales with the logarithm of J_{ph} and is unaffected by n_0. Hence the evenly spaced vertical contour lines in the lower right half of Fig. 3.3b. In low injection (upper left corner of Fig. 3.3b), the lifetime is again independent of photogenerated current density and doping density ($\tau_{SRH} = \tau_{p0} = 0.5ms$; see Fig. 3.4), but the extra term in Eq. 3.11 causes the V_{OC} to increase with the logarithm of no in addition to J_{ph}. Hence the diagonal contour lines (evenly spaced along both the x- and y-axes). For intrinsic recombination (Fig. 3.3a), in high injection the effective lifetime falls with increasing J_{ph} (increasing Δn in Eq. 3.1; see Fig. 3.4a) but not as fast as J_{ph} itself increases (Eq. 3.11). This again causes a logarithmic increase of V_{OC} with J_{ph} (C_1 is small), but with weaker dependence than

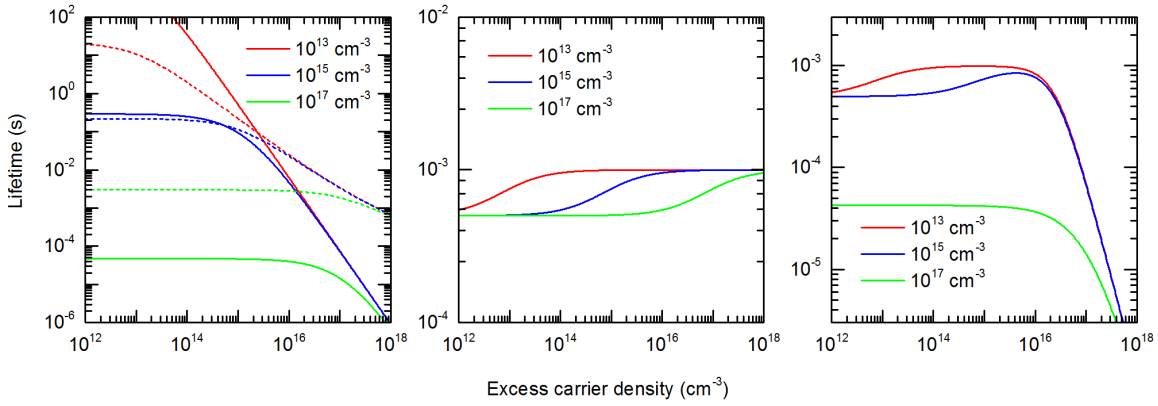

Figure 3.4: Injection-dependent lifetime curves of silicon solar cells on n-type, 170μm thick wafers with varying doping density. Lifetimes are shown for cells with intrinsic recombination, SRH recombination, and intrinsic and SRH recombination in (a), (b), and (c), respectively.

for SRH recombination (evenly spaced vertical contour lines with wider spacing). In low injection, the lifetime is constant with respect to $J_{\rm ph}$ (Fig 3.4a) yet again giving a logarithmic increase of $V_{\rm OC}$ with $J_{\rm ph}$.Unlike for SRH recombination, however, the low-injection lifetime decreases with increasing n_0 and does so faster than n_0 itself increases, so that $V_{\rm OC}$ decreases with increasing doping (see Eq 3.11). Interestingly, the trends in Fig 3.3a, which display the injection-level dependence just described, are not directly determined by the recombination mechanism (radiative or Auger). In particular, Auger recombination dominates whenever the excess carrier density ($n = n_0 + \Delta n$) is large, which occurs for increasing values along either axis. That is, Auger recombination dominates in low injection and some cases of high injection. Radiative recombination, by contrast, affects $V_{\rm OC}$ approximately as much as Auger, only in the lower left corner of the Fig, which corresponds to high injection!

Finally, Fig. 3.3c is a blend of Figs. 3.3a and 3.3b, with the $V_{\rm OC}$ lower than the lowest of the two $V_{\rm OC}$s from those figures. With the chosen SRH parameters, SRH recombination dominates at low photogenerated current density, while intrinsic

recombination dominates at high current density and at very high doping (Fig 3.4c). For a typical solar wafer and one-sun illumination, which is indicated by a yellow star, the V_{OC} is 725 mV and is nearly equally determined by intrinsic and SRH recombination. The cell is approaching high injection at open circuit ($\Delta n = 5n_0$).

Fig. 3.5ac show contour plots of the exact FFs extracted from the same $J - V$ curves used to create Fig. 3.3. (Note that each column in Fig. 3.5 has a different color scale because the range of FF values varies considerably depending on the recombination mechanism.) As is commonly observed experimentally, the FF and V_{OC} are somewhat correlated (c.f. Fig. 3.3 and 3.5). However, the shape of the FF and V_{OC} contours are far from identical because, unlike V_{OC} the FF is approximately the ratio of voltages: the voltages at maximum power and open circuit. (This simplified statement in fact assumes that $Jmpp/Jsc$ is constant. In fact, it varies from 0.9 to 0.97 across the contour plots, see Appendix B). In addition, the FF s in the case of only intrinsic and only SRH recombination give us little insight into the FF when both mechanisms are present. Figure 3.5c looks more like Fig. 3.5b than 3.5a, but with considerably higher values. In particular instances, FF is additionally complicated by the fact that the dominant recombination mechanism can be, e.g., SRH at the maximum power point but Auger at open circuit. For a typical solar wafer under one-sun illumination the $FF$is 79%, denoted again by a yellow star, which is nearly 10% lower than the intrinsic-recombination-limited FF and roughly equal to the SRH-limited FFİnterestingly, increasing or decreasing the photogenerated current density for this cell will result in a larger FF even though the V_{OC} increases monotonically with current density. The cell is between low and mid injection at maximum power ($\Delta n = 0.3n_0$). Using the exact V_{OC}s in Fig 3.3, we can now return to Eq 2.16 to find the associated approximate FFs and compare them to the exact FFs in Fig. 3.5. However, to use the expression, we also require an ideality

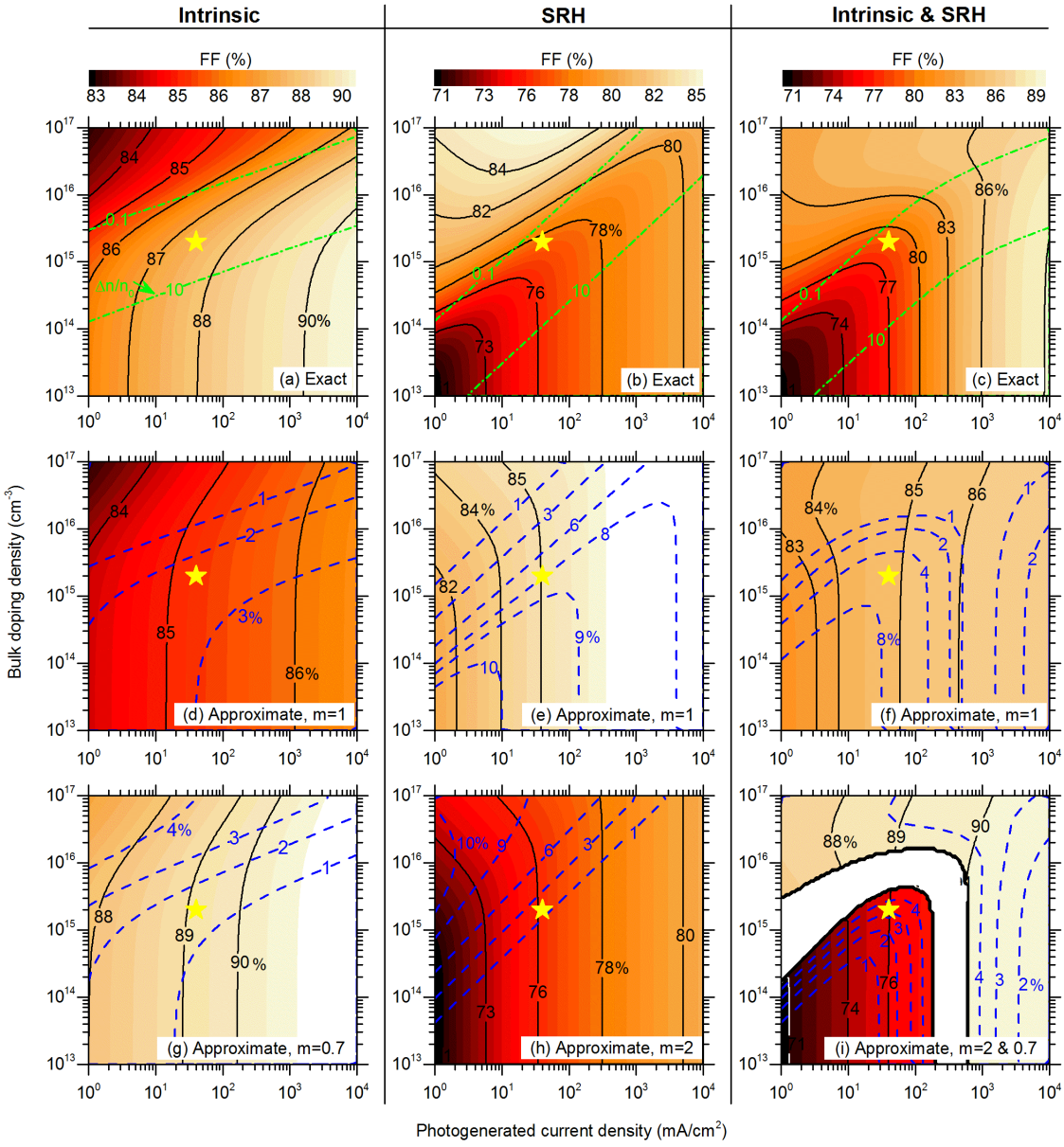

Figure 3.5: (a-c) Exact and (d-i) approximate FFs of silicon solar cells on n-type, 170 μm thick wafers with varying doping density under varying illumination levels (photogenerated current densities). FFs are shown for cells with intrinsic recombination, SRH recombination, and intrinsic and SRH recombination in the first, second, and third columns, respectively. The color scale is the same for each column, but not across columns. The dash-dotted green lines in (a-c) denote doping densities and photogenerated current densities for which n/n_0 is 0.1 or 10; these values are used to denote the boundaries of low injection (region above the upper green line) and high injection (region below the lower line). The yellow stars correspond to a typical solar cell with a $2\Omega cm$ n-type wafer under $AM1.5G$ illumination. The approximate FFs in (d-i) were calculated using the V_{OC}s shown in Fig. 3.3 and the assumed (constant) ideality factors shown. The blue dashed lines are contours of constant error in the FF in absolute percent.

factor. An ideality factor of $m = 1$ is most commonly assumed in the literature, and Fig. 3.5df show the resulting approximate FF. Note that the V_{OC}s in Fig 3.3a were used to generate Fig 3.5d, the V_{OC}s in Fig 3.3b were used to generate Fig 3.5e, and the V_{OC}s in Fig 3.3c were used to generate Fig. 3.3f. Comparing the colors in Figs 3.5df to those in Figs 3.5ac, there is little correlation between the exact FF and the approximate FF for any of the three recombination cases. The blue dashed lines are isocontours of the error in the FF in percent (absolute). Though the inaccuracy is less than 1% in the upper left regions of Fig. 3.5df, it reaches about 6% for a typical solar cell (yellow star) with both SRH and intrinsic recombination. That is, using the approximate expression for this cell predicts an overestimated FF of 85% when in fact the recombination limit is 79%.

What if, instead of assuming $m = 1$ under all conditions, we differentiate between low and high-level injection? The cut-offs for low and high injection are denoted by the green dash-dotted lines in Fig. 3.5ac. According to the theory, intrinsic recombination has a constant ideality factor of $m = 1$ in low injection and a constant ideality factor of $m \approx 0.7$ in high injection (where it is dominated by Auger recombination). SRH recombination also has a constant ideality factor of $m = 1$ in low injection, but the ideality factor converges to $m = 2$ in high injection. The following shows how these constants for the ideality factor are determined.

In order to calculate the ideality factor in both low and high injection for different recombination mechanisms, we rewrite Eq 3.6 as

$$(p_0 + \Delta n)(n_0 + \Delta n) = n_i^2 exp(fracqVk_BT) \tag{3.13}$$

In low injection, Eq. 3.13 can be reorganized to give

$$\Delta n = \frac{n_i^2}{n_0} exp(qVk_BT) \tag{3.14}$$

In high injection, Eq. 3.13 instead becomes

$$\Delta n = n_i exp(\frac{qV}{2k_BT}) \tag{3.15}$$

The Auger, radiative, and SRH lifetime expressions (see Eq 3.1 and 3.3) can each also be simplified in these two regimes as shown in Table 3.1. The C_i terms are constants. According to Eq 3.7, the recombination current density is

$$J_{rec} = qW\frac{\Delta n}{\tau_{eff}} \tag{3.16}$$

Inserting Eq 3.14 and 3.15, as well as the lifetime expressions in Table 3.1, into

Table 3.1: Lifetimes in low and high injection for individual recombination mechanisms

Recombination	Low injection	High injection
Aug	$\tau = \frac{1}{C_{Low,Aug}n_0^2}$	$\tau = \frac{1}{C_{High,Aug}\Delta n^{1.92}}$
Rad	$\tau = \frac{1}{C_{Low,Rad}n_0}$	$\tau = \frac{1}{C_{High,Rad}\Delta n}$
SRH	$\tau = C_{Low,SRH}$	$\tau = C_{High,SRH}$

Eq 3.16 leads to the recombination current density expressions in Table 3.2. The ideality factors are bold-faced in each expression. Note that $2/2.92 \approx 0.7$. We can

Table 3.2: Recombination current densities in low and high injection for individual recombination mechanisms

Recombination	Low injection	High injection
Aug	$J_{rec} = C_{Low,Aug}n_0n_i^2exp(\frac{qV}{\mathbf{1}k_BT})$	$J_{rec} = C_{High,Aug}n_i^2exp(\frac{qV}{\frac{2}{\mathbf{2.92}}k_BT})$
Rad	$J_{rec} = C_{Low,Rad}n_i^2exp(\frac{qV}{\mathbf{1}k_BT})$	$J_{rec} = C_{High,Rad}n_i^2exp(\frac{qV}{\mathbf{1}k_BT})$
SRH	$J_{rec} = \frac{qWn_i^2}{n_0C_{Low,SRH}}exp(\frac{qV}{\mathbf{1}k_BT})$	$J_{rec} = \frac{qWn_i}{C_{High,SRH}}exp(\frac{qV}{\mathbf{2}k_BT})$

now understand why the approximate FF in Fig. 3.5df is most accurate in the upper left corner of the plots, this area corresponds to low injection, for which $m = 1$, as was assumed. The following shows how these constants for the ideality factor are included. Figure 3.5g-i plot the FF calculated with the approximate expression using

a high-injection ideality factor for each recombination mechanism. The expression is again quite accurate in the injection range for which the ideality factor is appropriate (the lower right corner of the contour plots) for intrinsic recombination and SRH recombination. When the mechanisms are considered together in Fig 3.5i, however, it is not clear which ideality factor to use, and using $m = 0.7$ and $m = 2$ in the areas where intrinsic and SRH recombination dominate, respectively, produces unsatisfying results. In particular, the FF of a typical solar cell is incorrect by 3.5% absolute.

Based on Fig. 3.5, it appears that the approximate FF expression may be accurate if the correct ideality factor is used; the challenge is selecting that ideality factor. Each data point in Figs 3.5 and 3.3ac was extracted from an implied $J - V$ curve generated from a simulated lifetime curve, and Eq 3.8 calculates the ideality factor from such lifetimes. We therefore have the luxury of knowing the ideality factor as a function of excess carrier density ($m(\Delta n)$) for every doping density and photogenerated current density. Which carrier density should we use when calculating the ideality factor for the approximate the FF expression? Since the expression gives the FF a natural choice is the carrier density corresponding to the maximum power point; the resulting ideality factor is plotted in Figs 3.6a-c. Another reasonable option is the ideality factor corresponding to open circuit since the expression takes Voc as an input; the ideality factor for this case is plotted in Figs 3.6d-f Note that in 3.6 a and d, the ideality factor transitions from $m = 1$ to $m = 0.7$ when moving from low to high injection, as expected from expression 3.14, 3.15, 3.16 for intrinsic recombination. Similarly, it transitions from $m = 1$ to $m = 2$ in Fig. 3.6 b and e, as expected for SRH recombination. Our typical solar cell has an ideality factor of $m = 1.4$ at both maximum power and open circuit, which is not like any of the ideality factors assumed in Fig. 3.5.

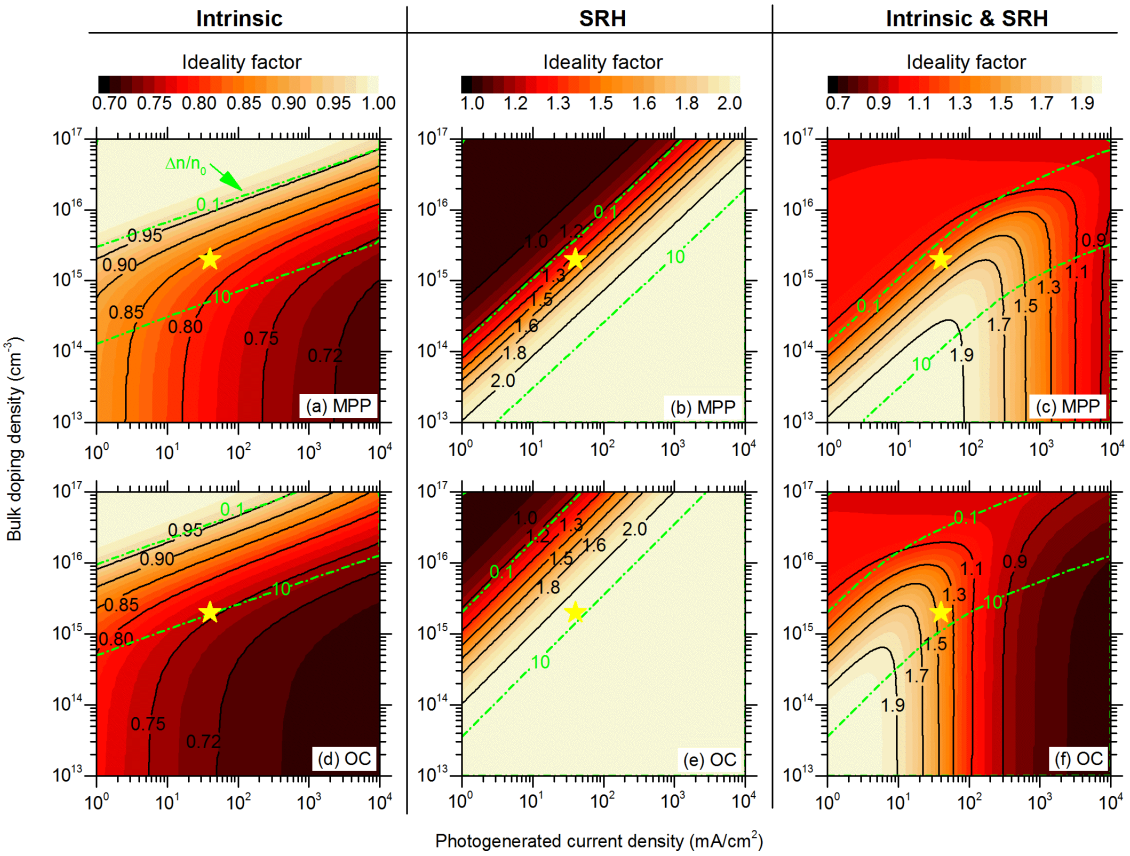

Figure 3.6: Ideality factors at (ac) maximum power and (df) open circuit of silicon solar cells on n-type, $170 \mu m$thick wafers with varying doping density under varying illumination levels (photogenerated current densities). Ideality factors are shown for cells with intrinsic recombination, SRH recombination, and intrinsic and SRH recombination in the first, second, and third columns, respectively. The color scale is the same for each column, but not across columns. The dash-dotted green lines denote doping densities and photogenerated current densities for which n/n_0 is 0.1 or 10; these values are used to denote the boundaries of low injection (region above the upper green line) and high injection (region below the lower line). The yellow stars correspond to a typical solar cell with a $2 \Omega cm$ n-type wafer under $AM1.5G$ illumination.

Fig. 3.7 a and b depict the FF calculated with the approximate expression using the precise ideality factors corresponding to the excess carrier densities at maximum power and open circuit, respectively. That is, Fig. 3.7 a and b are like Fig. 3.5 f or 3.5 i, but instead of a constant ideality factor, the exact, injection-level-dependent ideality factors shown in Fig. fig.Ideal c and f were used. Note that both intrinsic and bulk defect recombination mechanisms were considered. Comparing the colors in Fig. 3.7a, 3.7b, and 3.7c readily reveals that the approximate expression cannot replicate the exact FF in all cases, even if the true ideality factor is known; there is an inherent problem in using a single ideality factor to calculate a quantity that depends on two injection levels. Nevertheless, the expression can come close in select instances, even for cells not in distinctly low or high injection: For our typical solar cell, the absolute error in the FF is 2.6% in Fig. 3.7a and 1.7% in Fig. 3.7b. (as in Fig. 3.5, the blue dashed lines are error isocontours). However, even if somewhat accurate, this approach is impractical. One is unable to simply guess the best ideality factor to use, and the method employed here plots a $J-V$ curve from lifetime data, finds the maximum power point or open circuit, determines the associated Λn, and uses Eq. 3.8 to calculate m at that Δn yields the exact FF directly (from the $J-V$ curve) in fewer steps. Finally, as mentioned earlier, the shape of the FF and V_{OC}, contours are far from identical because, unlike V_{OC}, the FF is approximately a ratio of voltages-the voltages at maximum power and open circuit. This simplified statement in fact assumes that J_{mpp}/J_{sc} is constant. In fact, it varies from 0.9 to 0.97 across the contour plots as shown in Fig. 3.8.

3.3 Parametrization of fill factor upper limit

While it is apparently inappropriate to use the Green and Swanson approximations in conditions other than those for which they were derived (low injection) and it is improbable that there is a replacement expression that is generally applicable, it is

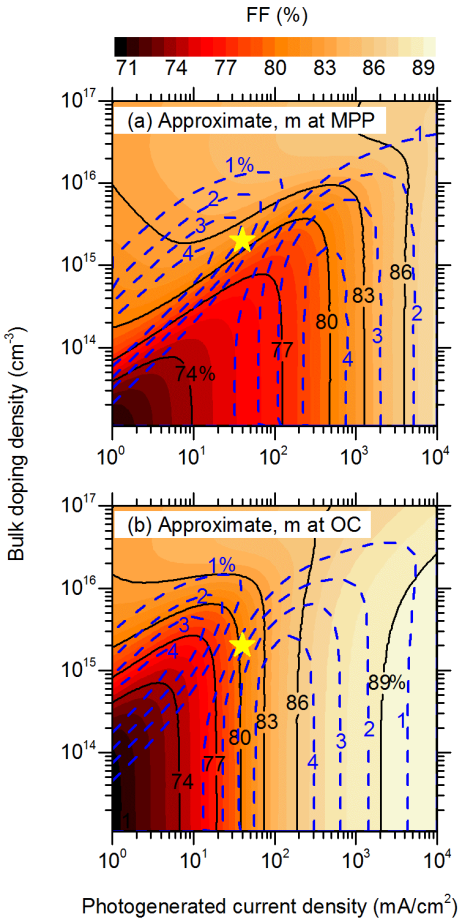

Figure 3.7: Approximate FFs of silicon solar cells on n-type, $170\mu m$thick wafers with varying doping density under varying illumination levels (photogenerated current densities). FFs are shown for cells with intrinsic and SRH recombination, and were calculated using the V_{OC}s shown in Fig. 3.3 and the ideality factors at (a) maximum power or (b) open circuit (the ideality factors are shown in Fig. 3.6 c and f). The color scale is the same for both plots. The yellow stars correspond to a typical solar cell with a $2\Omega cm$ n-type wafer under $AM1.5G$ illumination. The blue dashed lines are contours of constant error in the FFin absolute percent.

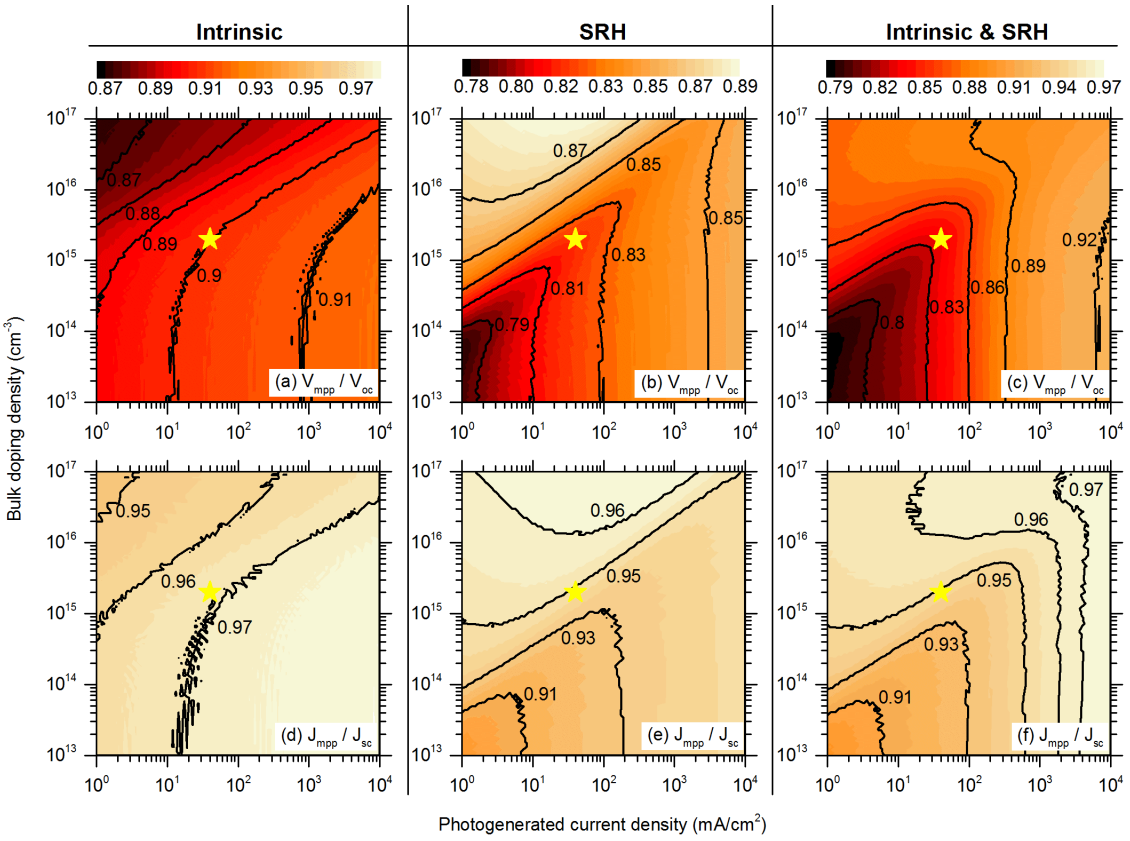

Figure 3.8: (ac) V_{mpp}/V_{oc} and (df) J_{mpp}/J_{sc} of silicon solar cells on n-type, $170\mu m$ thick wafers with varying doping density under varying illumination levels (photogenerated current densities). Ratios are shown for cells with intrinsic recombination, SRH recombination, and intrinsic and SRH recombination in the first, second, and third columns, respectively. The color scale is the same for each column, but not across columns. The yellow stars correspond to a typical solar cell with a $2\Omega cm$ n-type wafer under $AM1.5G$ illumination. The noisy contours are the result of numerical calculation error that arises when taking ratios.

possible to obtain an approximate expression for iFF in the simple case considered here of intrinsic recombination using only the MATLAB two dimensional curve fitting tool. The advantage of using this expression is that we only need to know about the doping concentration, wafer thickness and illumination intensity (photo-generated current). As seen, both the intrinsic FF and V_{OC} can be calculated independent of each other and we do not need to know about the value of V_{OC} in order to calculate FF or vice versa. Furthermore, the equation is completely independent of the ideality factor value. In fact, using this expression, one can differentiate between both FF and V_{OC} losses due to intrinsic recombination with the SRH and surface recombination mechanisms.

$$F(J_{ph}, N_0) = C_0 + C_1 J_{ph} + C_2 N_0 + C_3 J_{ph}^2 + C_4 N_0 J_{ph} + C_5 N_0^2 + C_6 J_{ph}^2 N_0 + C_7 N_0^2 J_{ph} + C_8 N_0^3 \tag{3.17}$$

in which,

$$J_{ph} = log(J_{ph}/w) \qquad and \qquad N_0 = log(n_0) \tag{3.18}$$

The constants are brought in reference [77], for n-type and p-type cells, respectively. Figure 3.9 a and b, show the calculated FF and V_{OC} using our suggested expression for comparison with the exact simulations shown in Fig. 3.5. As seen, the trend of variations is almost the same for both FF and V_{OC}.

3.4 Conclusion

We investigated the accuracy of the Green and, in less detail, the Swanson approximate expressions for the recombination-limited FF of hypothetical silicon solar cells. Though accurate for low-defect-density solar cells in very high and very low injection if ideality factors of 0.7 and 1 are used, the formulas give unacceptable errors for today's cells in typical operating conditions. Furthermore, while we considered only intrinsic recombination and SRH recombination at a single defect, introducing sur-

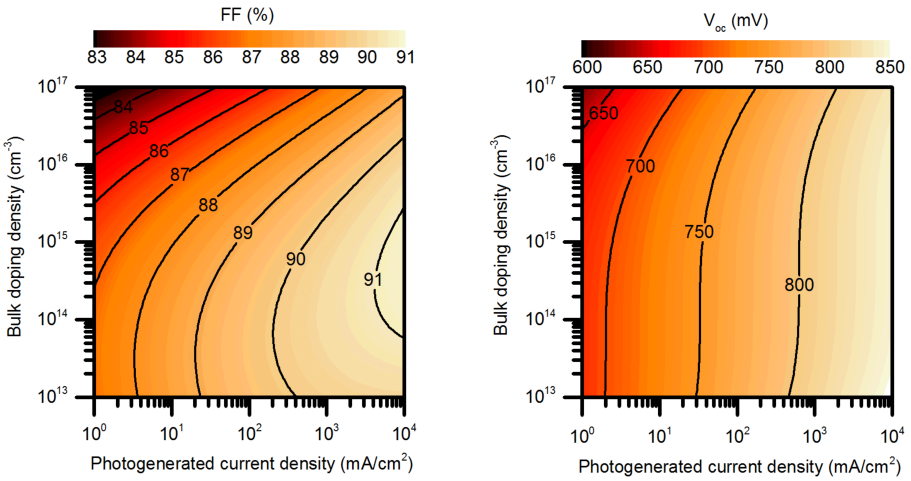

Figure 3.9: the calculated FF(a) and V_{OC}(b) using the suggested expression for comparison with the exact simulations

face recombination or multiple bulk defects in our analysis may exacerbate the error, particularly if the recombination mechanisms have strong injection dependence. The root of the problem is that the FF is determined by the recombination at both the maximum power point and open circuit (and, to a lesser extent, short circuit). As the dependence of the recombination rate on the excess carrier density frequently changes between these two operating pointswhich is reflected in a changing ideality factorno simple analytical expression can capture the complexity of FF. An extension of this conclusion is that, to accurately reflect the physics inside an operating cell, the ideality factor(s) in diode models should be a function of (implied) voltage.

What, then, are good practices for predicting the FF upper limit? We suggest calculating iFF from measured -or, if necessary, simulated- lifetime curves, as we have done here and others have done before [7, 40, 78]. This approach is becoming more common for silicon solar cells and has recently been codified in the newest quasi-steady-state photoconductance decay (QSSPC) software from Sinton Instruments. Most other cell technologies, however, are not amenable to QSSPC measurements

and no other comparatively simple technique presently exists to generate lifetime data as a function of injection level. These technologies would greatly benefit from new measurement methods, as they would facilitate accurate analysis of FF losses and prevent misuse of approximate formulas like that from Green.

Alternatively, we extracted an expression to relate iFF and iVoc of solar cells to the input parameters, i.e., wafer thickness, doping concentration, and photogenerated current.

Chapter 4

TCO optimization

As discussed in the introduction, series resistance can have different components, including bulk series resistance, contact resistance between top and bottom thin films, TCO sheet resistance and finger and busbar resistances. Among them, the silicon bulk series resistance is known and provided by wafer manufacturers. Metalization losses due to fingers and bus-bars are also easily measurable using a multimeter. However, other sources of series resistance are not very well defined and not measurable. Two of the most detrimental ones are the sheet resistance of front TCO layers, which limits the lateral transport of carriers, and the contact resistance at the interface of (a-Si and C-Si) and (doped a-Si and TCO). Here, we focus more on TCO layers and fill factor relevant losses. We study the trade off condition between TCO electrical and optical properties and discuss further the variation of this limitations when the SHJ is used as the bottom cell.

4.1 Introduction

Single junction crystalline silicon (c-Si) solar cells are reaching their theoretical efficiency limit and now industrial scale processes are producing cells with efficiencies above 25% [79]. As a result, further cost reduction of silicon based modules is not possible unless we come up with innovative designs that can boost the efficiency beyond 30%. Tandem solar cells that can integrate low- and high-bandgap materials are one of the most promising ideas to accomplish efficiencies beyond 30%. For two junction structures theoretical efficiencies of 44% can be obtained under 1-sun illumination [8]. Crystalline Silicon solar cells are promising for use as the bottom cell in such tandem devices due to their near-optimum bandgap and existing giga-watt-scale production capacity with cheap manufacturing costs [80].

In a two junction tandem structure, the performance of the bottom cell is most important for a wavelength range of 700-1200 nm ('IR spectrum' is hereafter used to refer to this wavelength range), because higher energy photons are mostly absorbed by the top cell. Among different silicon technologies, silicon heterojuncton (SHJ) solar cells are one of the most promising technologies to be used as the bottom cell. They are well-known because of their high V_{OC}, which results from the separation of the metal contacts from the absorber. SHJ cells, however, are suffering from high absorption at a wavelength range of 300-700 nm ('blue spectrum' is hereafter used to refer to this wavelength range) mainly in front intrinsic and doped a-Si layers. This will not be a shortcoming for the SHJ cells that are used in a tandem structure because this part of the light spectrum is already mostly absorbed in the top cell. Another advantage of SHJ cells is that their front TCO layer can perform as a tunneling recombination junction in two-terminal silicon solar cells [81]. TCO layers, however, are responsible for several losses in the IR spectrum, including, but not limited to, free carrier absorption (FCA) that can be categorized among optical losses, while sheet resistance and contact resistance can be categorized among electrical losses of SHJ cells. Optical losses in SHJ cell structure, is investigated expansively by several groups [20]. Specifically, performance of TCO at front and back, exposed to wavelength range of 300-1200nm ('full spectrum' is hereafter used to refer to this wavelength range) is compared and it is shown that front TCO layers play a more dominant role [82]. TCO source electrical losses are also investigated by current authors elsewhere under full spectrum [83].

There is a trade-off between optical and electrical losses in silicon heterojunction solar cells due to free-carrier absorption (FCA) in the front TCO layer: reducing FCA by lowering carrier density results in an increase in the sheet resistance and vice versa. Furthermore, variation of carrier density changes the refractive index and thus

the reflectance. Therefore, we need to optimize the front TCO thickness and carrier density in such a way that the overall power loss caused by reflectance, FCA, and series resistance is minimized. While optical optimization of the front TCO has already been thoroughly investigated [20, 82], a simultaneous study of ITO losses, both electrically and optically, has not been performed yet at one sun (single junction), let alone for a tandem structure, for which the SHJ cell exposure to light is limited to the IR spectrum. Accordingly, for tandem application, the photo-generated current drops to almost half of its value under full spectrum; this would result in lower electrical losses by decreasing the sheet resistance. As a result, more transparent - lower carried density with higher sheet resistance- TCOs can be applied on the front side, which then lead to comparable optical losses of front and back TCOs.

Here, we introduce and validate a methodology to design the front TCO layer of a SHJ solar cell to minimize the total associated power loss. We apply this methodology to the full spectrum - the wavelength range seen by a single-junction SHJ cell - as well IR spectrum, the wavelength range seen by a SHJ cell in a tandem with an approximately 1.75-eV-bandgap top cell. The latter analysis is limited to the case of a four-terminal tandem configuration, as the constraints on the front TCO are substantially different in a monolithic two-terminal configuration, and a TCO layer may not be necessary at all. To highlight the importance of this optimization, we evaluate our cells for IR spectrum and full spectrum, using four TCO films deposited with varying carrier concentration, and therefore with different transparency and conductivity.

For IR spectrum optimized SHJ cells, in particular, that are designed specifically to serve as bottom cells in four terminal tandems, the thickness of the front TCO layer, which acts as an anti-reflection coating, is tuned to maximize transmission of the $700 - 1200nm$ light that will be incident on the bottom cell. The front

TCO layer is also made with lower carrier density than in a one-sun cell, which decreases IR parasitic absorption without compromising lateral transport because the cell operates at approximately a half-sun equivalent (the generation rate is halved). Accordingly, for the IR spectrum, due to the lower value of photo-generated current, higher sheet resistances are tolerable and so finger spacing can be increased, thereby reducing shading losses.

Several groups have published silicon-based tandems, with NREL presently at the top of the one-sun efficiency chart at 29.8% with an InGaP cell stacked on top of a silicon heterojunction (SHJ) solar cell [84] in a four terminal structure. This four terminal tandem could be significantly improved by a tuned silicon bottom cell: A better infrared (IR) light response by minimizing reflection for IR light, as shown in our previous works [22], would push the tandem beyond 30%.

4.2 Experimental: TCO and a-Si layers fabrication

The TCO material that we have used in this work is indium tin oxide (ITO), reactively sputtered at room temperature using an $MRC944$ tool with a DC power supply using a target with a 90/10 In_2O_3/SnO_2 ratio. The oxygen concentration in the plasma and the ITO film thickness were varied to obtain carrier densities that varied from 2.5×10^{20} to $5.8 \times 10^{20} cm^{-3}$; and mobilities of all $20 \pm 10 cm^2/Vs$. ITO films were deposited on glass substrates both with or without i/n a-Si stacks beneath for optical and electrical characterization. Electron mobility and density were determined from hall measurements.

ITO films, including also i-, n-doped and p-doped a-Si:H layers were also deposited on polished silicon wafers to measure their thickness, refractive index n, and extinction coefficient k using a Woollam M-2000 spectroscopic ellipsometer. Ellipsometry spectra were recorded for an angle of incidence of 70° and a wavelength

range of $300 - 1200nm$; transmittance and reflectance spectra were recorded with the Lambda 950 spectrophotometer. The a-Si:H layers were deposited on glass and their ellipsometry and transmittance data were simultaneously fitted using a Tauc-Lorentz dispersion relation. ITO layers were deposited on a-Si:H i/n stacks on polished silicon wafers (the hydrogen in the a-Si:H layers alters the ITO properties upon annealing and thus it is preferable to characterize structures similar to those in the cells of interest) and their ellipsometry and reflectance data were simultaneously fitted using a combined Tauc-Lorentz and Drude dispersion relation. The complex refractive indices of monocrystalline silicon and silver (Ag) were taken from literature. Determined optical constants (n and k) of each specific ITO film, were used to simulate complete SHJ cells as a function of ITO thickness. Simulations of complete SHJ cells were done with Module Ray Tracer (MRT) from PV Lighthouse. MRT combines Monte Carlo ray-tracing with thin-film optics. Random pyramids of the textured silicon were simulated with base angle of 50.5° as was determined from angle-resolved reflectance measurements of the textured wafers.

Simultaneously, complete SHJ cells were fabricated applying all of the above ITO conditions to observe the corresponding effects on cell outputs. In detail, phosphorous doped monocrystalline CZ silicon wafers were double-side textured in KOH and subsequently cleaned in RCA-B and Piranha to remove metal and organic contaminants. The wafers were then dipped in 5% HF solution to remove the native oxide layer and immediately put under vacuum for a-Si:H deposition. a-Si:H stacks were deposited using PECVD (Applied Materials $P - 5000$); Chamber pressure and temperature was set to 4 $torr$ and $250°C$, respectively. ITO layers were sputtered through a shadow mask to define several 4 cm^2 cells per wafer. Silver was sputtered on the back side of the wafer to form a full area hole electrode while on the front the silver was screen printed to finish the electron electrode. The silver fingers crossed

the cell with bus bars that were outside the measurement area. The cells were then annealed at $200°C$ for 20 minutes to dry the silver paste. External quantum efficiency (EQE) and reflectance measurements were performed on cells and were recorded over the $300 - 1200nm$ wavelength range using a PV Measurements QEX10 tool. The total reflectance was measured over the same wavelength range using a PerkinElmer Lambda 950 spectrophotometer equipped with an integrating sphere. The angle of incidence was 7° from the wafer normal. Finally, Sinton FCT-450 flash tester was used to measure the IV curve along with the Suns-V_{OC} curve of each cell.

4.3 TCO layer properties

Our main goal here is to determine total power losses due to front TCO layers, both in experiment and simulation, and to compare them. To perform the simulation we need to know our layer characteristics, specifically a-Si layers and TCO, μ, N, n, k, t for a wide range. We selected ITO as our TCO layer because it's common and has tunable thickness and carrier density nearly independent of mobility. The analysis can be extended to any other TCO material. Several ITO layers with different characteristics were studied, among them two sets of samples with different O_2 concentrations, selected for further discussion in this paper.

Before we focus on our simulation and methodology, we need to have accurate n and k values of our layers. Other research groups have already studied ITO optical characteristics [48, 85]. Our measurement shows strong coincidence with n, k values already reported in the literature. However, as well studied in Ref. [86], we found that having an under-layer, a-Si:H layers would affect both electrical and optical characteristics of ITO layers significantly and complicate the role of variation in layer thickness, O_2 fraction and annealing state. The main reason is the effusion of hydrogen from underlying a-Si:H layers into ITO after annealing for 20 min at

$220°C$. In fact, Hydrogen acts as a dopant and so its effusion leads to an increase in both ITO conductivity and free carrier absorption. The pattern of Hydrogen effusion in ITO layers is dependent to ITO layer O_2 concentration, ITO layer thickness and annealing time and temperature after ITO layer sputtering. Figure 4.1a-c shows measured carrier density, mobility and sheet resistances for ITO layers with two different O_2 concentrations (2.5% and 7%) sputtered on i- and p-doped and i- and n-doped a-Si:H layers before (as-deposited) and after annealing. Please note that as ITO layers become more transparent (higher O_2 concentration), hydrogen effusion plays a more significant role and leads to a significant boost in the carrier density. The same dependency is observed for layers sputtered on n doped a-Si:H layers. The carrier density decreases with increasing thickness; this could be due to lower concentration of hydrogen in thicker ITO layers compared with thinner ones. The mobility does not seem to have a strong dependence on ITO layer thickness because an increase in carriers concentration increases the mobility a little bit. The reason for this is unclear to us. Given the large change in carrier concentration for the more transparent layer after annealing, we investigated the effect of annealing temperature (the stars in each figure correspond to TCO layers made with identical conditions) in Fig. 4.1d-f. A unique feature of heterojunctions is their symmetry prior to TCO deposition, and both front-emitter and rear-emitter configurations are common. For completeness, these figures also include the properties of the same TCO layers deposited and annealed on i/p. The take away from Fig. 4.1d-f is the following: (1) although the i/n and i/p layers are quite different, they have the same effect on the overlying ITO layers when annealed, (2) an increase in annealing temperature leads to a stronger hydrogen effusion and results in higher carrier density. As a conclusion, the annealing temperature is critical in determining the final carrier density of front ITO layers. Concurrently, it significantly affects the finger and bus bars series resistances. This

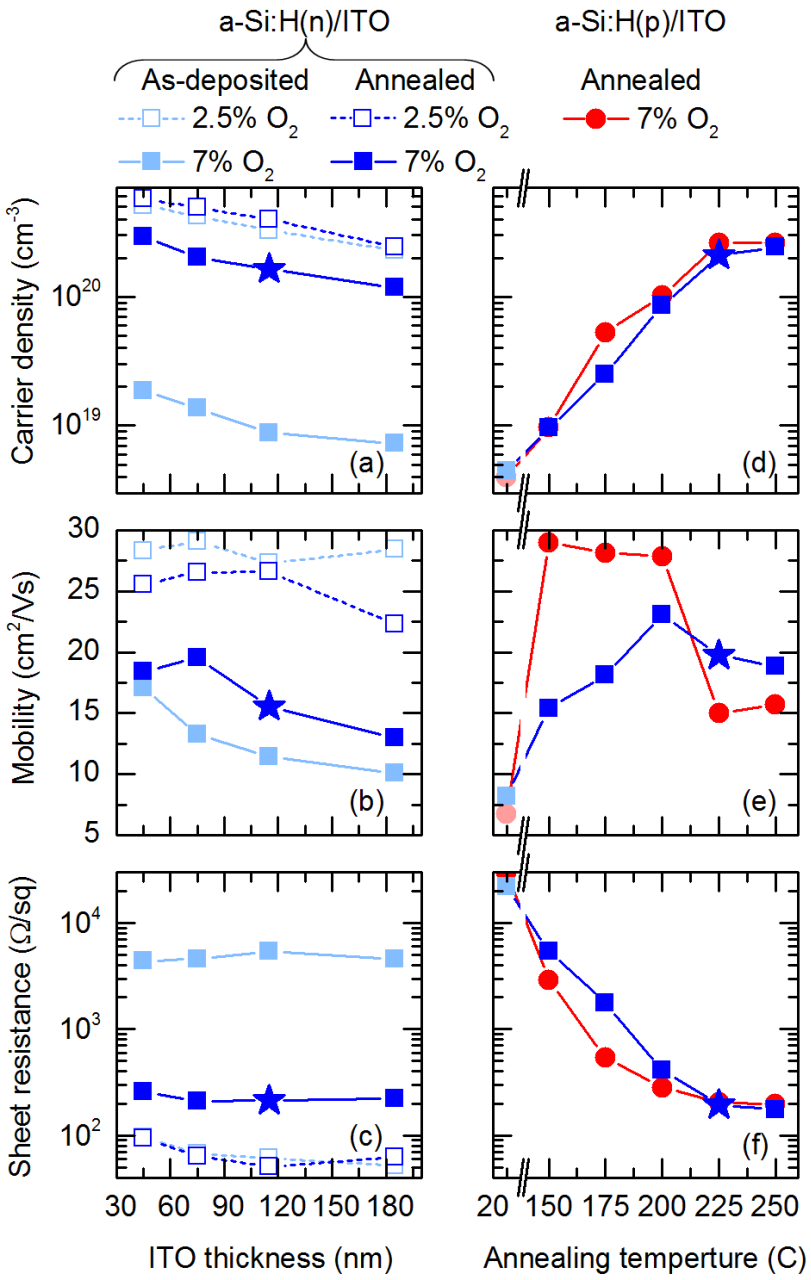

Figure 4.1: Carrier density, mobility and sheet resistance for ITO layers with varying thickness and O_2 concentration conditions, with or without i/n and i/p a-Si stack layers beneath. Blue stars show the conditions applied to our IR spectrum optimized solar cell.

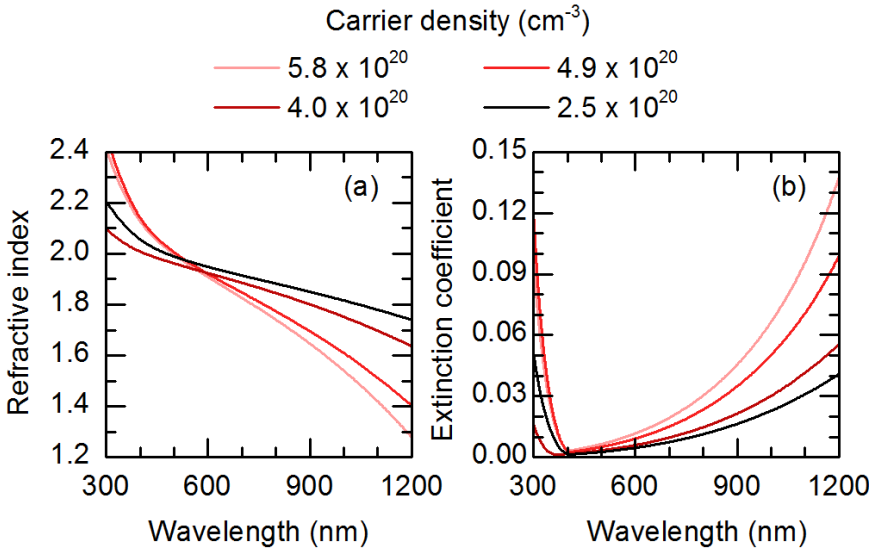

Figure 4.2: Refractive indices of the four ITO films studied, with different layer thicknesses leading to different carrier concentrations.

interdependency should be considered in any further device structural design.

For the rest of the paper, we chose four representative layers with the same oxygen concentration and four thicknesses, which lead to four carrier densities, to use for the loss simulation. These ITO layers are the ones shown in Fig. 4.1a-c with empty dark blue color squares. Corresponding refractive index, n, and extinction coefficient, k, values for these layers have been shown in Fig. 4.2. This data is used in our simulations in rest of the paper.

4.4 Minimizing current loss

In most similar studies [20, 87–89], it is common to perform EQE loss analysis, which focuses just on J_{SC} to optimize TCO and a-Si:H layer characteristics optically. We take this approach to begin with, since it is also a convenient way to validate our optical model. In the final analysis, however, electrical losses will be considered in parallel to optical losses through designing a power (instead of current) loss model. First, different components of current loss in front ITO layers is investigated, then parallel

electrical loss due to variation in sheet resistance of these ITO layers is considered. Adding them together, the output power loss is calculated and further optimization and suggestion is provided based on illumination under both IR spectrum and full spectrum.

Fig. 4.3 shows the reflected current, parasitic absorption current, escaped current and photo-generated current in a textured silicon substrate covered with four different ITO films with varying carrier concentration, calculated as a function of thickness under both IR spectrum (solid lines) and full spectrum (dashed lines) illumination.

Fig. 4.3a shows the reflected current for the four ITO films as a function of thickness. To minimize the front surface reflectance in the IR spectrum with a single layer ITO antireflection coating, the optimal refractive index (n_{opt}), and optimal thickness (t_{opt}) are given by $n_{opt} = \sqrt{n_{air} \times n_{Si}}$ and $t_{opt} = \lambda/(4 \times n_{ITO})$. Thus, for $n_{Si} = 3.5$ the n_{opt} is equal to 1.87 and t_{opt} is $\approx 120nm$ for a minimum at $\lambda = 900nm$ and $n_{ITO} \equiv n_{opt}$. Figure 4.3a shows the simulated front surface reflectance loss expressed in terms of current for the four ITO films (four different carrier concentrations) as a function of their thickness. Not surprisingly, the minimum front-surface reflectance under IR spectrum illumination, occurs for ITO thicknesses greater than $120nm$, and the minimum value depends on the carrier concentration because it alters the refractive index of the ITO film (see Fig. 4.2a). Among these four ITOs the lowest value of minimum reflectance loss is for $2 \times 10^{20} cm^{-3}$ concentration ITO because its refractive index is closer to n_{opt} at $\lambda = 900nm$ and thus also its thickness is closer to $120nm$. For other ITOs that have higher carrier concentration their refractive index at $\lambda = 900nm$ is lower than n_{opt} and thus their minimum reflectance loss is achieved at thickness greater than $120nm$. This thickness establishes

a reflectance minimum near $900nm$, in the middle of the IR spectrum wavelength band. Figure 4.3a suggests that IR SHJ cells need thicker ITO layers; however, to obtain the highest possible photo-generated current in the cell, FCA in the ITO films should be taken into account in addition to reflection.

Fig. 4.3b shows FCA loss and its dependence on ITO layer thickness and carrier concentration. The parasitic absorption current increases equally (with the same slope) both under full spectrum and IR spectrum conditions because TCO absorption is primarily in the IR region being the common part under both spectrums. There is a constant offset between two sets of curves, however, that is due to the a-Si:H layers absorption in the blue region. Figure 4.3c, shows the escape current loss ($\lambda \geq 1000nm$) for these four different ITO films. Escape reflectance (loss) is a result of a low absorption coefficient of the absorber and non-optimal light trapping scheme. But even in a hypothetical 'perfect' solar cell with Lambertian light-trapping and no front-surface reflectance and no parasitic absorption the escape reflectance would still be present and would be the only loss. The only way to minimize escape loss is either by changing the absorber to one that has higher absorption coefficient or by adopting light-trapping scheme that is superior to Lambertian. Consequently, escape reflectance is not 'bad' and does not determine the optimal ITO thickness. Therefore, for a given light trapping scheme and front-surface reflectance the escape loss is inversely proportional (not linearly) to parasitic absorption. As expected, the highest escape reflectance loss is given for the most transparent ITO ($2 \times 10^{20} cm^{-3}$) and the reason is because it has the lowest parasitic loss.

The photo-generated current is shown in Fig. 4.3d and is given by the maximum current afforded by the random-pyramid texture (which is near-Lambertian) minus the losses in Fig. 4.3a-c. It shows how the absorbed current varies as a func-

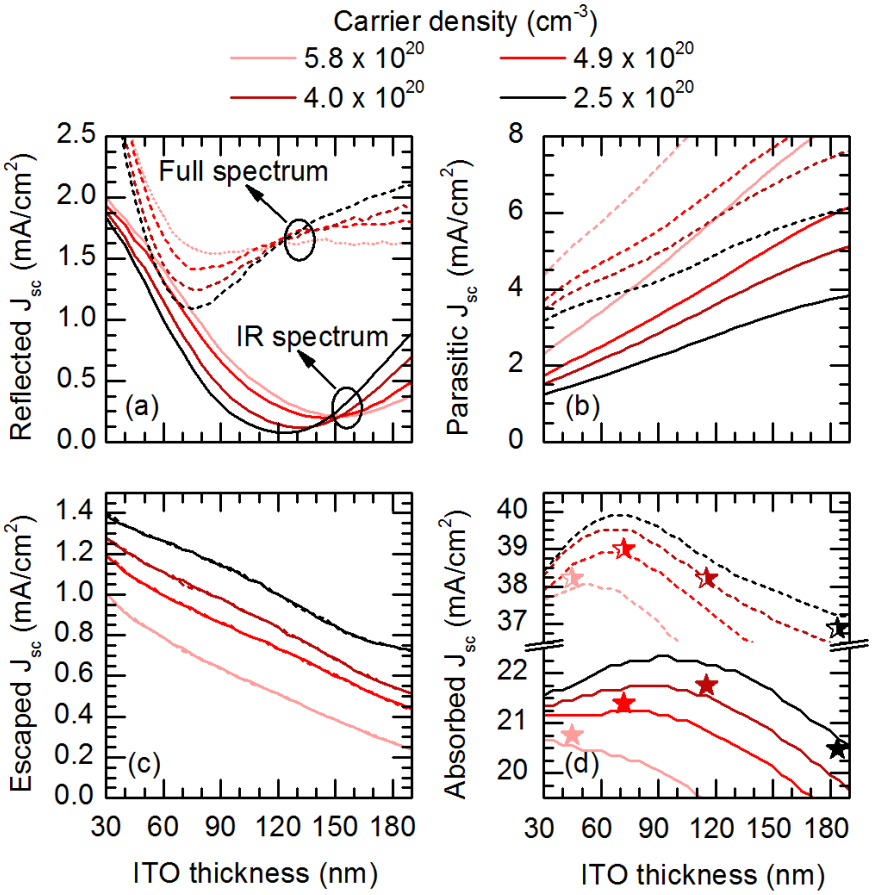

Figure 4.3: Reflected (a), parasitic (b), escaped (c) and absorbed currents (d) for ITO layers with varying thicknesses and O_2 concentrations, with i/n a:Si stack layers beneath. Stars show the corresponding measured EQE currents of fabricated cells applying each specific layer.

tion of ITO thickness. Note that for IR spectrum illumination the current maximum is shifted toward lower thicknesses than those found in Fig. 4.3b, because parasitic absorption in the IR increases with film thickness. This is different than under full spectrum illumination, for which the best ITO thickness is approximately $70nm$, regardless of the carrier concentration (i.e., front-surface reflection is more important than FCA for full spectrum illumination). Furthermore, because of enhanced FCA at higher carrier concentrations, the optimum ITO thickness decreases with increasing carrier density-opposite the trend for reflectance minima, in which the optimized

thickness was shifted to higher values for increasing carrier density because of decreasing refractive index. The optimal ITO thickness for an IR SHJ cell-from a current density perspective-is approximately $100nm$ for the corresponding carrier density of to $2.5 \times 10^{20} cm^{-3}$. Under full spectrum, however, the optimum thickness would be around $70nm$ and again for the corresponding carrier density of $7 \times 10^{20} cm^{-3}$ which is not shown here.

SHJ solar cells were fabricated with front ITO layers of varying thicknesses and carrier concentrations corresponding to those modeled. This was achieved by varying the thickness of ITO films deposited on a-Si layers for two different O_2 concentrations during sputtering, namely those shown in Fig. 4.1. The stars in Fig. 4.3d show the short-circuit current densities (J_{SC}) obtained from integrating external quantum efficiency (EQE) measurements on SHJ cells over the IR spectrum and one spectrum wavelength range. The simulated and measured values are well matched and validate the broad maximum around $100nm$ for the IR spectrum. Small discrepancies (with at most 2% error) between the measured and modeled data are most likely due to imprecise modeling of n and k values of ITO films sputtered on glass slides with i/n a-Si layers beneath (totally three layers needed to be modeled and fitted).

4.5 Minimizing power loss

Optical optimization of the front TCO layer is important, however, there is always a trade-off between electrical and optical losses. For each specific TCO carrier concentration, to determine the TCO film thickness which leads to both the lowest optical and electrical losses, we calculated power losses due to front-surface reflection, FCA in the TCO layer, sheet resistance, escaped light and shading, separately and then summed over them (see following expression).

$$P_{loss}(n,t,l) = P_{shading}(l) + P_{sheet}(n,t,l) + P_{optical}(n,t) \tag{4.1}$$

where

$$P_{optical}(n,t) = P_{parasitic}(n,t) + P_{reflection}(n,t) \tag{4.2}$$

In which, $P_{loss}, P_{shading}, P_{sheet}, P_{optical}$ are corresponding to total, shading, sheet and optical power losses, respectively. Optical power loss itself includes both parasitic and reflection losses denoted by $P_{parasitic}$ and $P_{reflection}$ respectively. n, t and l represent carrier density, ITO thickness and finger spacing, respectively. Note that the TCOs contribution to the lumped contact resistance, resulting from its interfaces with both a doped a-Si:H layer and metal fingers, is ignored in this analysis. These losses are not readily calculable, even if the precise properties of the adjacent layers are known (which they are frequently not), but we anticipate that any contact resistance may be a function of n but not t or l [22]. Note that power loss can be defined and reported in different forms, e.g. power loss compared to silicon radiative-limit efficiency assuming Lambertian light trapping. What we reported here, however, is defined as a percentage of the total photon power in the wavelength range of 300 to $1200nm$ (full spectrum) or 700 to $1200nm$ (IR spectrum).

$$P_{loss}(n,t,l) = 1 - \frac{P_{total}(n,t,l)}{P_{input}} \tag{4.3}$$

The advantage of evaluating power loss instead of any other parameter is that even if its absolute value is not accurate (e.g. because of imprecise modeling of optical constants), the corresponding ITO thickness characteristics for which it would be minimized (or optimized) will not change.

The optical power losses are calculated from the same reflectance and absorbance spectra, generated by the PVLighthouse Module Ray Tracer, used to calculate the current losses in Figure 3. The spectra are multiplied by the AM1.5G spectrum and integrated over the wavelength ranges identified above.

$$P_{parasitic}(n,t,l) = \int_{300\ or\ 700}^{1200} f(\lambda) Abs(n,t,l,\lambda)_{TCO} d\lambda \tag{4.4}$$

$$P_{reflection}(n,t,l) = \int_{300\ or\ 700}^{1200} f(\lambda) Ref(n,t,l,\lambda)_{TCO} d\lambda \tag{4.5}$$

Finally, the power loss resulting from shadowing of the cell by the fingers can be calculated through

$$P_{shading}(l) = P_{input}\left(\frac{aw_f + lw_b}{al}\right) \tag{4.6}$$

where a is the finger length, l is finger spacing and w_f and w_b are the finger and busbar thicknesses, respectively.

The ohmic power loss P_{sheet} is then obtained using the following expression [90] under IR spectrum and full spectrum, respectively.

$$P_{sheet} = (1/12) R_{sh} \times J_{MPP}^2 \times l^2) \tag{4.7}$$

where J_{mpp} is current at maximum power point (MPP). The sheet resistance for each of the four ITO films was calculated using the following expression.

$$R_{sh} = \frac{1}{e\mu nt} \tag{4.8}$$

where e and μ are electron charge and mobility. Measured values of mobility alongside the carrier densities shown in figure 4.4a used to calculate the sheet resistance of each of four specific layers. Corresponding sheet power loss is shown in figure 4.4b and 4.4c under IR and full spectrum, respectively. Sheet power loss increases both by increment of finger spacing and sheet resistance. At the upper end, with wide finger spacing and high sheet resistances, its value will not exceed 5%.

These figures can be used as a guide to determine the highest tolerable sheet power loss for a given sheet resistance and finger spacing. Based on the obtained value for sheet resistance, one may then determine the allowed pairings of carrier concentration and mobility. For instance, with a finger spacing of $3mm$ and an allowed power loss of 2%, under IR spectrum illumination, sheet resistances of up to

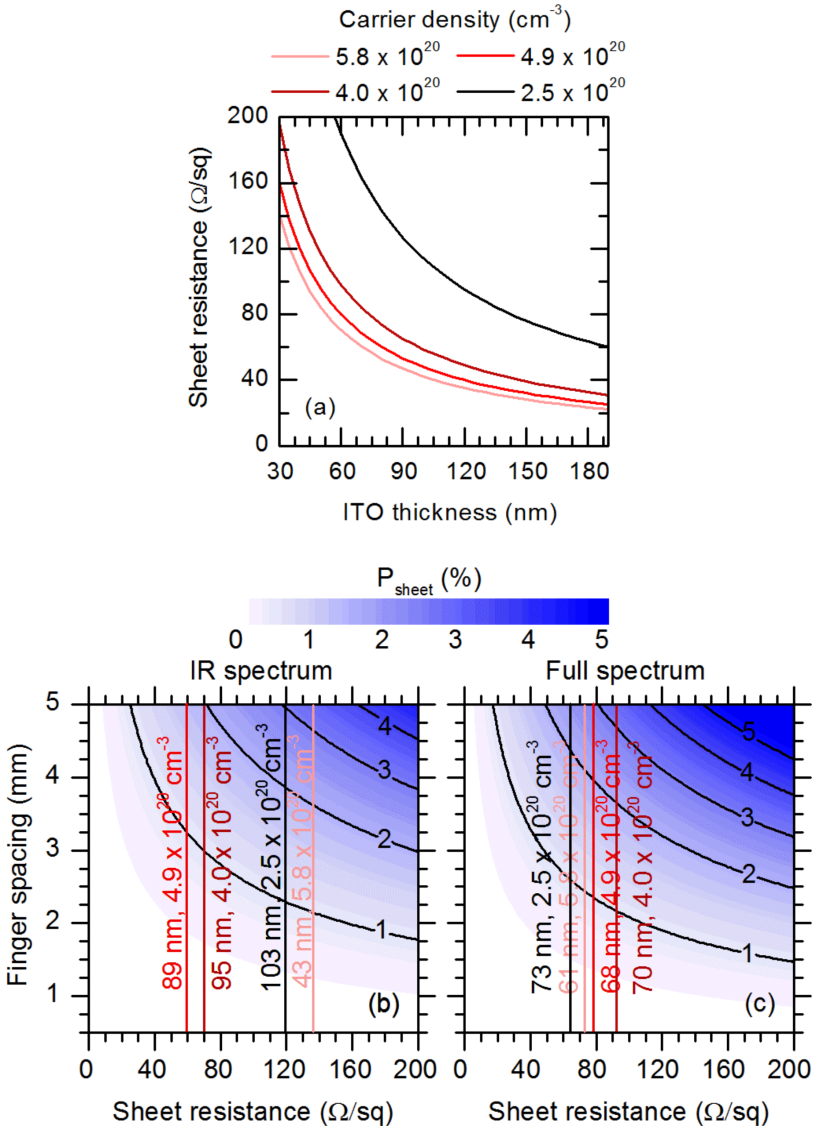

Figure 4.4: a) Sheet resistance for four different ITO film carrier densities, b) Sheet power loss (color scale), as a fraction of the input power, versus sheet resistance and finger spacing. The vertical lines correspond to the ITO layer thicknesses for which the power loss minimized in figure 4.5a and 4.5b for IR spectrum (solid lines) and full spectrum (solid lines) illumination, respectively.

$200\Omega/sq$ may be tolerated while under one sun, values lower than $120\Omega/sq$ are needed. Not surprisingly, this indicates that under IR spectrum illumination the front TCO is less restricted by electrical optimization compared to illumination under one sun condition.

Finally, by adding the optical and electrical power losses, the total power loss versus ITO thickness and finger spacing is calculated for each of the four ITO layers with different carrier densities. The results are plotted in figure 4.5a and 4.5b, corresponding to IR spectrum and full spectrum, respectively. Decreasing carrier concentration, we shift toward lighter blue colors (figure a1 toward a4 and similarly b1 toward b4) both under IR and full spectrum illumination. This shows the dominance of optical power loss over electrical power losses (vertical axis does not play a significant role in color variation). This can be observed by comparing contour values in figure 4.5 with figure 4.4 b and c; The sheet power loss is much smaller compared to the total power losses. Dashed and solid lines in figure 4.5 correspond to the ITO thickness for which the total power loss is minimized. The optimum will be shifted to the left (thinner ITO layer) by increasing the carrier concentration and resulting boost in optical power losses. The solid and dashed lines in figures 4.4 and 4.5 are actually corresponding to each other.

Figure 4.6 shows the total power loss for the optimized ITO thickness indicated by the solid and dashed lines in figure 4.5. As seen, by considering reflection and escape losses in addition to parasitic absorption, the role of sheet power loss becomes less significant and correspondingly its dependency on finger spacing decreases, especially under half sun illumination. This figure can be used as a guide to design the optimum finger spacing of the front screen for a specific carrier concentration. Figure 4.6 also shows that a finger spacing of around $3mm$ leads to the lowest loss under

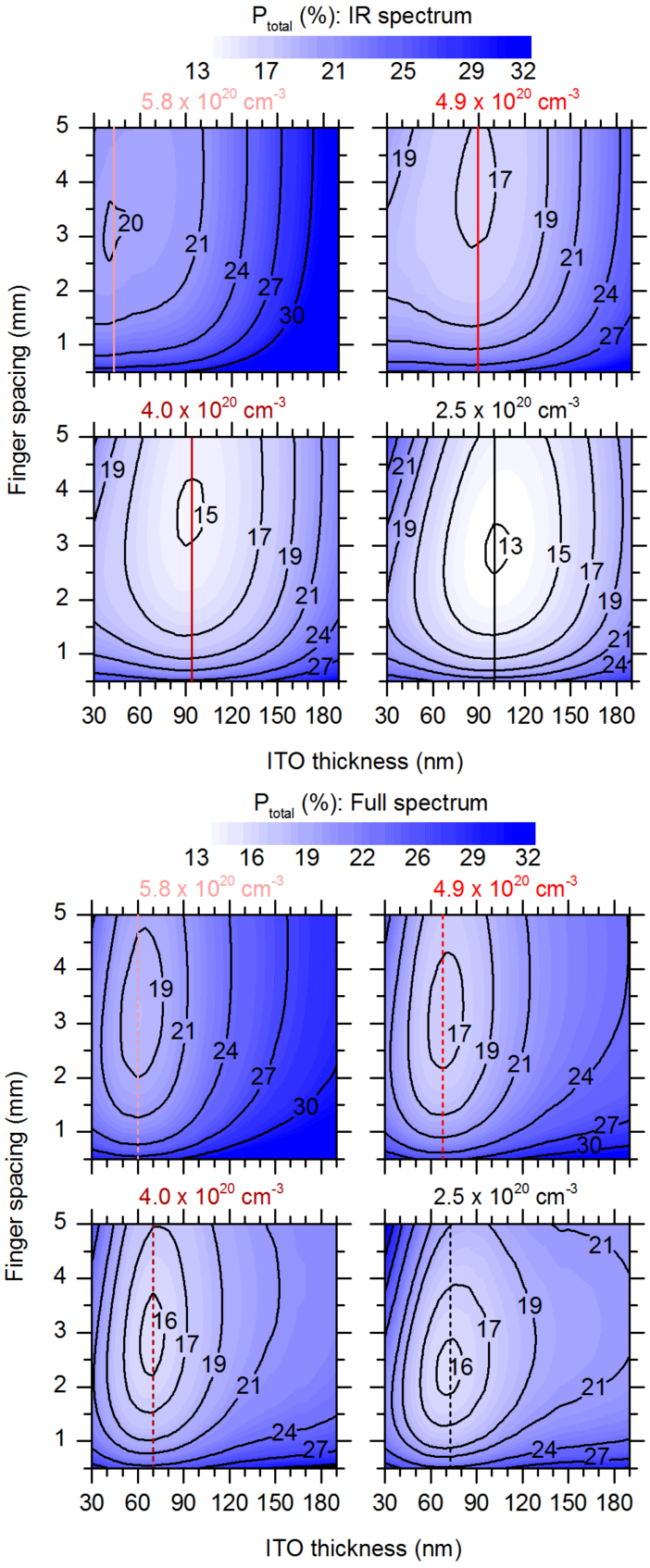

Figure 4.5: Total power loss versus ITO thickness and finger spacing for four ITO layers with different carrier densitie under IR spectrum (a) and full spectrum (b).

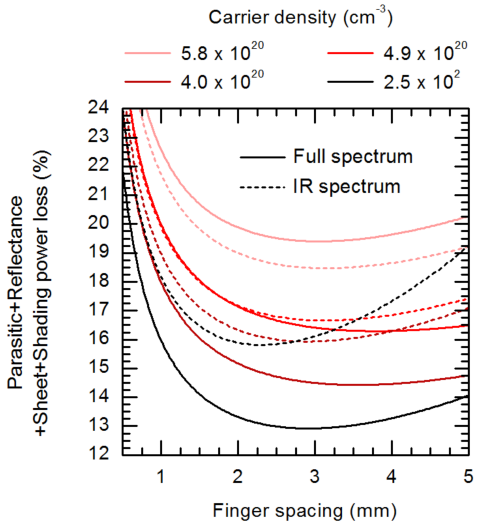

Figure 4.6: Total reflection, FCA, shading, and sheet power loss of SHJ cells with four ITO films and varied finger spacing. Results are shown under half sun (solid lines) and one sun (dashed lines) illumination.

half sun illumination for the TCO with a carrier density of around $2.5 \times 10^{20} cm^{-3}$. Under one sun illumination using the same film, a finger spacing of $2.2mm$ has the lowest loss. These two ITO layers have optimal thicknesses of $73nm$ and $103nm$, respectively. Note that as mentioned before, these presented values are all related to the set of samples with an O_2 concentration of 2.5% and varying thicknesses that were all relatively conductive. For more transparent samples ($7\%O_2$), however, parasitic losses in the front ITO layers diminish, while electrical losses increase; this leads to a stronger dependence on finger spacing (sharper minima for the total power loss would be observed). Note that, here we have presented the global optimum values which means that for each specific ITO layer thickness, the total power loss was calculated allowing us to select the minimum.

Figure 4.7 shows the contributing components of figure 4.6 in more detail. These components are shading power loss, sheet power loss, absorption power loss and reflectance power loss. The last two among them are categorized under optical

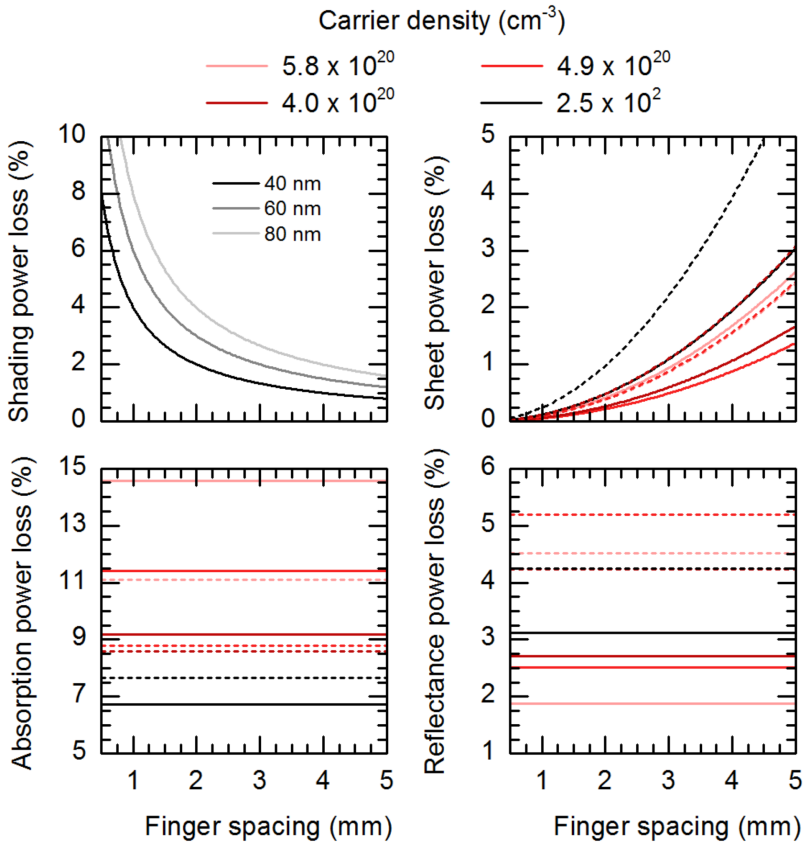

Figure 4.7: Building components of total power loss (shown in figure 4.6) including shading power loss, sheet power loss, absorption power loss and reflectance power loss.

power loss and thus do not depend on ITO thickness. The shading power loss is shown for three varied finger line widths.

We can expand this analysis to other TCOs like indium zinc oxide (IZO) or hydrogen-doped indium oxide; these layers are usually more transparent with higher mobilities, but their contact resistance (to silver paste, doped amorphous silicon layers, or both) is larger. The rear TCO can also be further optimized for the half sun range using a more transparent and thicker layer at the back [20].

Applying all TCO optimizations on complete cells, we measured EQEs for IR SHJ cells that exceed that of the Panasonic SHJ record cell [4] for wavelengths

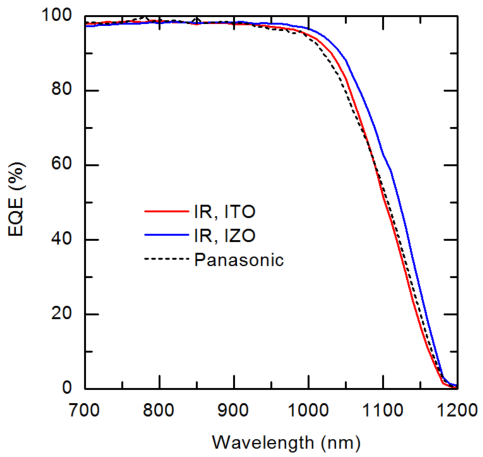

Figure 4.8: EQE of IR SHJ cells with optimized ITO and IZO front layers, as well as the EQE of the Panasonic record cell [4].

above $700nm$ as shown in figure 4.8. The V_{OC} of the IR SHJ cell with IZO is $722mV$ under one-sun illumination and $705mV$ at the half-sun illumination (using a neutral density filter) that is nominally seen by a bottom cell in a tandem structure. The FF is 77.9%, measured at half-sun illumination. For the range of $700-1200nm$, the AM1.5G-weighted efficiency of the IR SHJ cell at half-sun illumination is 36%.

4.6 Cell outputs

In this Section we present our cell results, mainly FF and efficiency for both sets (2.5 and $7\%O_2$) of our samples. As we will see later, J_{SC}(obtained from EQE measurement) values confirm our simulated results. In figure 4.9, we can see that both $FF$and efficiency are also following the predicted trends. As shown in figure 4.6, for the range of the carrier densities that we presented, finger spacing between 2 and $3mm$ have comparable losses so we we do not expect a recognizable dependence of FFon the finger spacing. The importance of this optimization for IR light is clear: the calculated difference in photo-generated current density between the two cases is $1.1mA/cm^2$. Note that this gain is significant for a silicon bottom cell working under reduced illumination with a maximum theoretical photo-generated current density of

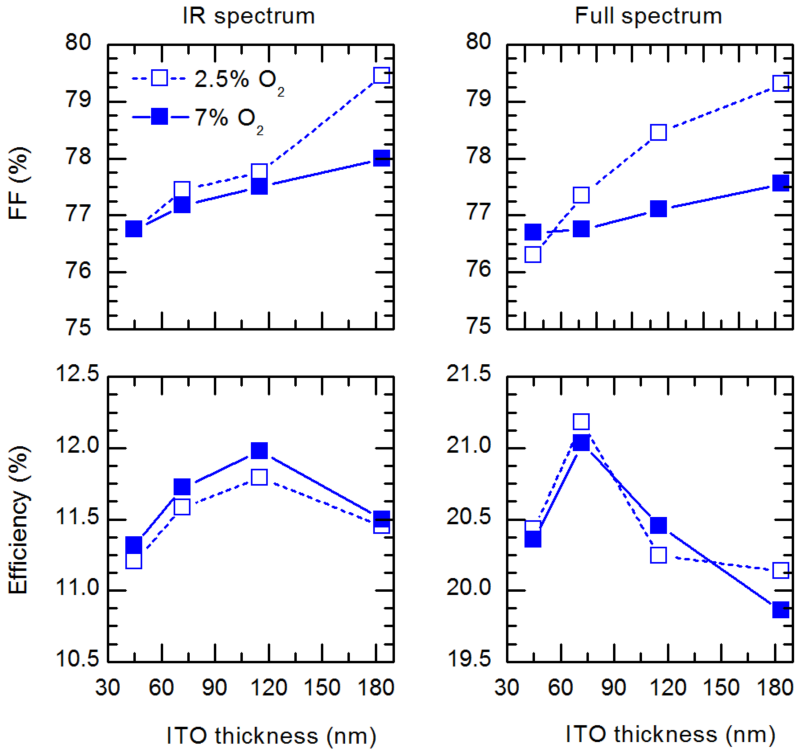

Figure 4.9: shows the measured $FF$and efficiency values on three different cells with different spacing. Cells in the left column are measured under half sun, while the ones in the right column are measured under one sun. Red curves represent cells with set of 2.5%O_2 concentration, blue curves represent cells with set of 7%O_2 concentration.

$22.5mA/cm^2$ $(1.1/22.5 = 4.9\%)$.

Chapter 5

Contact resistivity

[1].

5.1 Introduction

As bulk quality and passivation quality of silicon wafers improves and so recombination losses decrease, series resistance related losses turn to become the most significant source of loss in SHJ solar cells. As initially discussed by Wurfel and Cuevas [11, 12], carrier selective contacts can be considered as the most detrimental source of total series resistance losses. An electron selective contact must have the following properties: 1) the voltage drop produced by the electron current towards the electron contact needs to be less than a few millivolts to maintain high fill factor (ideally, the external voltage should be matched with the implied voltage) and 2) the hole current towards the electron contact must be negligible . The same can be said for the hole contact by swapping the word hole for electron. These conditions are realized when a contact: 1) has a high conductivity for one of the carriers and 2) has a large asymmetry in the conductivities of the two carrier types- the conductivity of the minority carrier must be low.

While the above cited works give excellent qualitative definitions for selectivity in terms of the conductivities of the majority and minority carriers, Brendel and Peibst capture the essence of these conductivities in terms of experimentally measurable parameters: the contact resistivity, ρ_{C}, and the contact recombination parameter, J_0. The conductivity of majority carriers is captured in ρ_{C} while the conductivity of minority carriers is captured in J_0 which can clearly be seen in the first mathematical

[1]This chapter is co-written by William Weigand, PhD student at Holman group, ASU; Contact address: William.Weigand@asu.edu

definition of selectivity. Brendel and Peibst define the selectivity of the contact as the logarithm of the ratio of the thermal voltage, V_{th}, to the product of J_0 and ρ_C: $S_{10} = log(V_{th}/(J_0\rho_C))$ [91]. This quantitative definition of selectivity clearly expresses the requirements outlined above and provides an experimental pathway to determine selectivity: J_0 can be determined through lifetime measurements [92], while $\rho_C$can be determined via transfer length method (TLM) measurements.

As an upper bound of contact resistivity for contacts that have a small area, Schroeder and Meier propose a solar cell with a front contact fraction of 5% of the cell area and a front sheet resistance of $(100\Omega/sq)$ from which they calculate that the contact resistivity must be less than 2 $m\Omega cm^2$ for a power loss of less than 0.5%. For a contact that is full area, such as the rear side of a solar cell or either contact in a heterojunction solar cell the conditions are a bit more relaxed, allowing a contact resistivity as high a 83 $m\Omega cm^2$ for the same power loss [93]. While one would expect that a 20 fold increase in contact area would result in a 20 fold increase in contact resistivity, the effect of current crowding for a smaller contact fraction becomes a limiting factor in the calculation.

Contact resistivity measurements are not new in silicon solar cell development and have been performed on contact structures with a wide range of values. There are three main methods used to determine contact resistivity. The simplest method is TLM, where one measures the resistance between a series of contact pads that are spaced at varying distance between each other [90]. Circular TLM (CTLM) is similar to TLM, except annular contacts are used instead of the traditional rectangular pads [94]. Contact resistivity can also be extracted by measuring the resistance through an entire device as described by Cox and Strack [95].

Table 5.1 provides a non-exhaustive list of different contacts, both metal to

diffused emitter and multi-layer heterojunction types, and their respective contact resistivities. Although heterocontacts tend to show a lower J_0 than direct metal contacts, their corresponding contact resistivities - with the exception of the Ca/TiO_x and LiF_x/Al electron contacts and the MoO_x hole contact - are $1-5$ orders of magnitude higher than a metal - to - diffused emitter contact. The relatively low contact resistivity of the exceptions mentioned above reflects their potential candidacy to boost the efficiency of silicon solar cells towards theoretical limits by acting as carrier selective contacts.

Table 5.1: Contact resistivities of carrier selective contacts.

Contact type	Contact test structure	$\rho_C(m\Omega cm^2)$
Metal to diffused emitter	c-Si(p)/c-Si(n+)/Ag paste [96]	1-2
Metal to diffused emitter	c-Si(p)/c-Si(n+)/Ni/Cu [97]	0.035
Metal to diffused emitter	c-Si(p)/c-Si(n+)/Ti/Pd/Ag [97]	0.073
Electron Heterocontact	Al/Mg/c-Si(n)/MgOx/Al [98]	17.5
Electron Heterocontact	c-Si(n)/a-Si:H(i)/Mg/Al [99]	220-310
Electron Heterocontact	c-Si(n)/TiOx/Ca/Al [100]	5
Electron Heterocontact	c-Si(n)/LiFx/Al [101]	2
Electron Heterocontact	c-Si(n)/a-Si:H(i)/a-Si:H(n) [16]	370
Electron Heterocontact	c-Si(n)/a-Si:H(i)/a-Si:H(n)/Ti/Al [102]	30
Electron Heterocontact	c-Si(n)/a-Si:H(i)/a-Si:H(n)/Ti/Cu [102]	10
Electron Heterocontact	c-Si(n)/a-Si:H(i)/a-Si:H(n)/Ti/Pd/Ag [102]	10
Electron Heterocontact	c-Si(n)/a-Si:H(i)/a-Si:H(n)/Al [102]	10
Electron Heterocontact	c-Si(n)/a-Si:H(i)/a-Si:H(n) [103]	140
Electron Heterocontact	c-Si(n)/a-Si:H(i)/BZO [104]	40
Electron Heterocontact	c-Si(n)/LiF/Al [105]	26
Hole Heterocontact	c-Si(p)/MoOx [19]	1
Hole Heterocontact	c-Si(p)/a-Si:H(i)/μ c-Si [106]	800
Hole Heterocontact	c-Si(p)/a-Si:H(i)/a-Si:H(p) [97]	380
Hole Heterocontact	c-Si(p)/a-Si:H(i)//a-Si:H(p) [103]	240
Hole Heterocontact	c-Si(p)/a-Si:H(i)//a-Si:H(p) [107]	11
Hole Heterocontact	Glass/PEDOT:PSS/Ag [108]	28

Interestingly, a thorough contact resistance analysis has not been fully reported for the most developed heterocontact to silicon solar cells: the amorphous

silicon/crystalline silicon heterocontact. This contact, originally developed by Sanyo, is now a key ingredient in the highest efficiency silicon solar cells to date with efficiencies greater than 26%, which utilized the heterojunction back contact technology [8]. The importance of the a-Si:H/ITO interface has been shown by Gogolin, et al, who measured all the resistive losses except the contact resistance of a typical silicon heterojunction solar cell (SHJ) and by subtracting the measured values from the measured series resistance they show that the a-Si:H/ITO interface is typically the most dominant resistive loss [17].

Similar to Gogolin, Lee, et al. attempted to understand the resistive losses in HBC cells and calculated the contact resistance by creating test structures to measure the total resistance through a stack containing metal, emitter a-Si:H(p), n c-Si, metal (ohmic contact) and subtracting off the known resistances determined through similar test structures. As seen in Table 1, they obtain values of 0.38 and 0.37 Ωcm^2 for the a-Si:H(i)/a-Si:H(n)/ITO/Ag and a-Si:H(i)/a-Si:H(p)/ITO/Ag contacts, respectively, contradicting the well held belief that for SHJ the hole contact causes the most detrimental resistive loss [16].

The most direct measurement of the contact resistance in SHJ solar cells came from Lachenal, et al. [103]. In this work the authors used the method developed by Sinton and Cuevas [103] to calculate a total series resistivity of 0.62 Ωcm^2 for a rear emitter bifacial SHJ solar cell. In addition, the authors used TLM to determine the contact resistivity of the a-Si:H(i)/a-Si:H(n)/ITO/Ag and a-Si:H(i)/a-Si:H(p)/ITO/Ag stacks with a value of 0.14 Ωcm^2 for the n-type stack and 0.24 Ωcm^2 for the p-type stack. Summing these two contact resistivities accounted for just over 60% of the total series resistance in the cell indicating the importance the resistivities of these contacts play in the overall performance of SHJ solar cells.

In this Chapter we extend the analysis of Lachenal, et al. by measuring the contact resistivity as a function of a-Si:H and ITO layer parameters and correlate with cell performance. Specifically, we focus on the hole contact in a traditional SHJ solar cell consisting of a-Si:H(i)/a-Si:H(p)/ITO/Ag and quantify the contact resistance through the transfer length method, series resistance, pseudo- fill factor (pFF), and fill factor (FF) as a function of easily tunable process parameters. In particular, we vary the a-Si:H(i) thickness, the a-Si:H(p) thickness and gas flow during PECVD, and the oxygen (O_2) gas concentration during ITO sputtering. From our experiments we quantify the impact of the hole contact resistance on SHJ solar cell device operation.

5.2 Hole Contact Resistivity

5.2.1 Materials and methods

To investigate the effects of the hole contact stack in the SHJ solar cell we made both TLM structures, to measure contact resistance, and cells, to extract pFF, FF, and series resistance, in parallel. As shown in figure 5.1a, the TLM structures consisted of a p-type wafer, symmetric hole contacts and a TLM pattern in sputtered ITO and Ag. As shown in figure 5.1b, the cells consisted of an n-type wafer with the same hole contact on the back as that of the TLM structure except the sputtered ITO and Ag are now full area and there is an electron contact on the front.

Boron- and phosphorous-doped CZ silicon (CZ Si(p,n)) wafers ($156mm$ pseudo-square) were double side textured in KOH to a thickness of 180 μm and subsequently cleaned in RCA-B solution for metals removal, Piranha solution for organics removal, and again in RCA-B solution for residual metals removal. The bulk resistivity of the silicon wafers was approximately 2 Ωcm for the boron doped and $3.8\Omega cm$ for the phosphorous doped samples. The wafers were then dipped in a 1 : 10 buffered oxide etch (BOE) solution for 1 minute to remove the native oxide on the surface and subsequently put under vacuum for a-Si:H deposition.

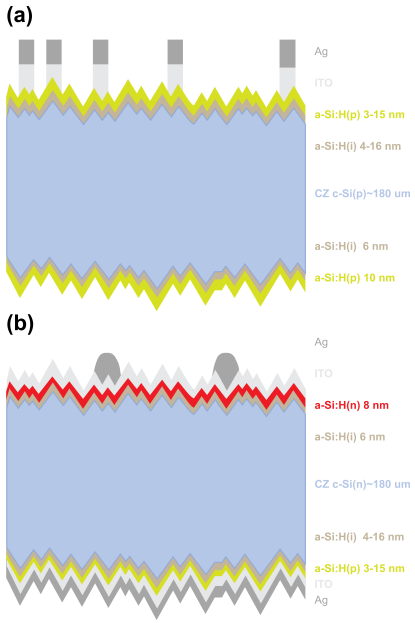

Figure 5.1: a) Schematic of TLM structures used to extract contact resistance. b) Schematic of full solar cells used to extract pFF, FF, R_{series}.

The a-Si:H layers were deposited using radio frequency (RF, $13.56MHz$) plasma enhanced chemical vapor deposition (PECVD) in an Applied Materials P5000. The tool has three chambers which deposit either intrinsic a-Si or either of the doped a-Si in order to prevent contamination of the chamber of the opposite dopant.

The standard ITO layers were sputtered in an MRC 944 using a DC source power of $1kW$ using a target that was $90/10 In_2O_3/SnO_2$. For the standard recipe the chamber pressure was $7.1mTorr$ in an ambient gas with oxygen partial pressure of $0.21mTorr$.The ITO layer thickness was $160nm$. For the ITO oxygen flow series the oxygen partial pressure during sputtering of the ITO varied from 0.14 to $0.85mTorr$.

For the TLM structures the ITO was deposited with a shadow mask to create TLM pads with spacings ranging from $250\mu m$ to $8000\mu m$. The width of the pads was $2mm$ and the length of the pads was $8mm$. Silver was also sputtered on top of the ITO pads to guarantee a constant potential. After depositing the TLM pads the

wafers were annealed at $200°C$ for 20 minutes to simulate the annealing necessary for the screen printed silver in full cells. The samples were then cleaved and the TLM pads removed from the wafer.

For the cells ITO was sputtered through a shadow mask to define several $4cm^2$ cells per wafer. Silver was sputtered on the back side of the wafer to form a full area hole electrode while on the front the silver was screen printed to finish the electron electrode. The silver fingers crossed the cell with bus bars that were outside the measurement area. The cells were then annealed at $200°C$ for 20 minutes to dry the silver paste.

Three TLM samples were cleaved rather than laser removed from the wafers because the laser cutting left edge damage, preventing accurate measurement. The TLM measurements were initially done by placing four probes, two current and two voltage, on subsequent sets of the silver pads and running an IV sweep. To make the measurements quicker a digital multimeter with two probes was used and compared to the four probe method. After comparing the four probe method and the multimeter method, we found the results to be extremely accurate (within 1%) and all subsequent measurements were done using the multimeter. All contact resistivity values are the average of three TLM patterns from the same wafers with error bars representing the standard deviation among the patterns.

For cell measurements a set of three $2cm \times 2cm$ cells were measured. A shadow mask was placed on the cut out sample such that only one cell was subject to testing at a time. Four probes, two current and two voltage, were placed on the silver bus bars and arranged so that they did not shade the cell. A Sinton FCT-450 flash tester was used to measure the IV curve along with the Suns-V_{OC} curve of each cell. From these measurements we report the pseudo- fill factor (pFF), fill factor (FF), and the

series resistivity (R_s). This is calculated by comparing the Suns-V_{OC}curve with the one sun curve as described by Sinton and Cuevas [36] with the formula provided by Pysch and Glunz [37]. All of the measurement are the average of the three cells with error bars representing the standard deviation of the sample set.

5.2.2 Results and discussion

5.2.2.1 a-Si:H(i) layer thickness

Others have studied the effect of the thickness of the a-Si:H(i) layer on complete silicon heterojunction solar cells, using current-voltage characteristics alone to reveal trends. Tanaka, et al. found that inserting a $4nm$ a-Si:H(i) layer between the c-Si and the a-Si:H(p) resulted in an increase in fill factor by approximately 0.8% while further increases in the thickness caused a drop in fill factor [109]. The increase in $FF$with a $4nm$ a-Si:H(i) layer is the result of a reduced surface recombination compared to a cell without this layer. Similar to Tanaka, Fujiwara and Kondo found that a $4nm$ a-Si:H(i) layer produced the optimal efficiency; yet they did not observe the same trend of a decreasing FFabove this thickness [110]. The same trend was seen by Holman, et al. who found that an initial increase in the a-Si:H(i) layer from $3nm$ to $4nm$ resulted in an increase in the FF while further increases did not change the FF[110]. The FF in all the above papers was relatively low and did not exceed 75%.

Figure 5.2 shows the effect that the a-Si:H(i) thickness has on both complete cells (pFF, FF, and R_s) and TLM structures (ρ_C). Figure 5.2a reveals a slight increase in the pFF from 82.9% to 84.0% by increasing the a-Si:H(i) thickness from 4 to $16nm$, which is due to the improved surface passivation. While the increase in pFF can be used to gauge how well the final cells will perform, this same trend is not represented in the final $FF$of the cell. Here, the FFdrops from 76.9% at a thickness of $4nm$ to 71.1% at a thickness of $16nm$; a drop of over 5%.

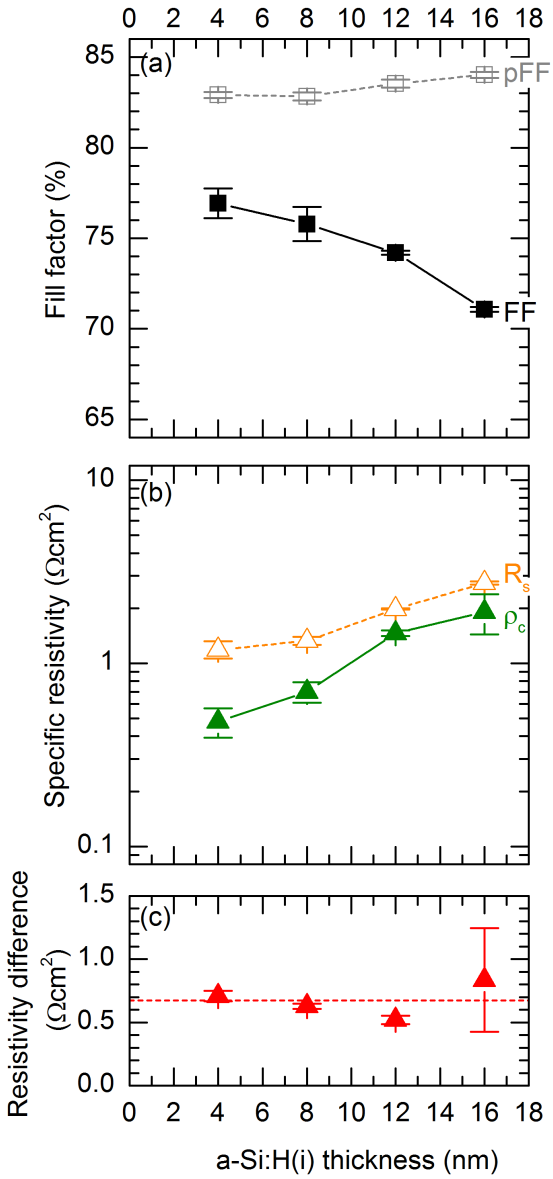

Figure 5.2: (a) pFF and FFas a function of a-Si:H(i) layer thickness. (b) $r_{\mathrm{S}}$and ρ_{C}. (c) Difference between $r_{\mathrm{S}}$and ρ_{C}. The red dashed line is the average resistivity difference of all samples.

Changing series resistivity, shown in figure 5.2b, is responsible for the drop in $FF$and increases from 1.19 to 2.75Ωcm^2 over the same a-Si:H(i) thickness range. This increase in series resistivity correlates to the contact resistivity, measured on separate TLM structures, which increases from 0.48 to 1.91 Ωcm^2. In particular, figure 5.2c shows that the difference between the series and contact resistivities is approximately constant for the range of a-Si:H(i) thicknesses investigated, indicating that the drop in $FF$is entirely attributable to growing contact resistivity. The contact resistivity for the thinnest a-Si:H(i) layer is twice that reported by Lachenal for their baseline layer [103] and approximately 1.2 times the value reported by Lee [16]. Not shown in this plot is a set of experiments where we repeat the same set of contact resistivity experiments and obtained values that range from 0.18 to 1.50Ωcm^2. These contact resisitivity samples did not have a matching set of solar cells;thus are not included in this Chapter. Also, the contact resistivity for a $6nm$ a-Si:H(i) layer was 0.23Ωcm^2 which is the same as that reported by Lachenal. This variation by a factor of two can possibly be attributed to process variation from the layers deposited after a-Si:H(i) (a-Si:H(p), ITO, Ag) or to additional interactions between that layers that were not investigated in this work.

To thoroughly explain the trends shown here, an analysis of the conduction mechanism through the a-Si:H(i) layer is required, but the exact conduction mechanism through a-Si/c-Si heterojunctions is still debated. Early models show that for thick a-Si:H(i) (approximately $1\mu m$ thick) the dominant transport mechanism is multitunneling capture-emission [111]. Our a-Si:H(i) layers are significantly thinner than this and the diffusive model proposed by Taguchi, et al. may be more appropriate [112]. In fact, they propose this diffusive model because of the resulting decrease in $FF$and increase in R_s with a-Si:H(i) layer thickness which are the same trends realized in this Chapter. Schulze, et al. provide a thorough analysis of transport

through a-Si/c-Si heterojunctions which showed that the dominant transport was again diffusive at high forward bias but increased surface passivation revealed heterojunction transport properties [113]. The results shown in this section show that the dominant transport mechanism is diffusive but we cannot yet disregard other possible mechanisms and a thorough computational and experimental analysis is necessary to pinpoint the exact mechanism or mechanisms.

5.2.2.2 a-Si:H(p) layer thickness and doping

Those reports in which the a-Si:H(i) thickness is varied usually also vary the a-Si:H(p) thickness. Namely, Tanaka, et al. studied the effect of the a-Si:H(p) thickness on heterojunction solar cells without an underlying a-Si:H(i) layer. They found that increasing the thickness of the a-Si:H(p) layer resulted in a slight drop in the FF [109]. Fujiwara and Kondo also studied the effects of a-Si:H(p) layer thickness and found that the FFremained relatively constant as a function of a-Si:H(p) thickness when the thickness exceeded $3nm$, below which the FF sharply decreased [110]. In contrast, Holman, et al. found that FFcontinued to increase for a thickness greater than the $3nm$ threshold determined by Fujiwara and Kondo [20].

It is also important to note that previous studies did not mention how the doping level of the a-Si:H(p) layer affected the cell characteristics. Bivour, et al. indicated that for sufficiently high doping of the a-Si:H(p) layer a fill factor of greater than 81% was achieved [114]. Bivour, et al. also performed simulations to obtain the same FF trend of Fujiwara and Kondo when the doping was sufficiently high. At lower doping the FF values were much lower and actually led to a loss in the FF with increasing a-Si:H(p) thickness, indicating the importance of doping in the a-Si:H(p) layer [51]. Note that in all the studies mentioned above, the a-Si:H(p) layer was at the front of the solar cell, while in our experiments the a-Si:H(p) layer is on the back,

as mentioned in section II.

Figure 5.3a shows that the pFF remains constant within experimental error at 81.5% over the entire thickness range. Similar to Fujiwara and Kondo, when the a-Si:H(p) layer is thicker than $3nm$ the FF remains relatively constant; in our case with a value of approximately 78%. The FF shown in figure 5.3a remains relatively constant at approximately 78% for thicknesses greater than $3nm$, but the FF drops to 76% for a thickness of $3nm$. This trend is consistent with the work of Fujiwara and Kondo.

As seen in figure 5.3b, for thicknesses greater than $3nm$ the R_{S}remains constant at $0.8\Omega cm^2$ as would be expected by the constant FF. Figure 5.3c confirms that the difference between $R_{\mathrm{S}}$and $\rho_{\mathrm{C}}$is also constant over this thickness range indicating that there are no changes to the Rs regardless of a-Si:H(p) layer thickness.

The most interesting feature of figure 5.3 are seen for the thinnest a-Si:H(p) layer. The $FF$of these cells is approximately 76% – a 2% decrease from the thicker layers. The $R_{\mathrm{S}}$of these cells is $1.1\Omega cm^2$, which is only $0.3\Omega cm^2$ greater than the thicker layers but the ρ_{C}increased to $0.99\Omega cm^2$, which is a factor of three greater than the thicker layers. The difference between the $R_{\mathrm{S}}$and $\rho_{\mathrm{C}}$is also much lower than the others. The poor performance of this cell is likely due to a depletion width, which is larger than the layer thickness [115].

For the a-Si:H(p) layer doping experiments, the pFF remains constant at about 81% as seen in figure 5.4 which indicates that al the cells should perform equally well in the absence of series resistance. The fill factor, shown in Figure 5.4a, of these cells has a particularly interesting trend. At low doping the FFincreases from a low of 68% and reaches a maximum of 79% at a gas flow of $18sccm$. At higher gas flows, the FFdrops by about 4% as the gas flow approaches $50sccm$ and decreases

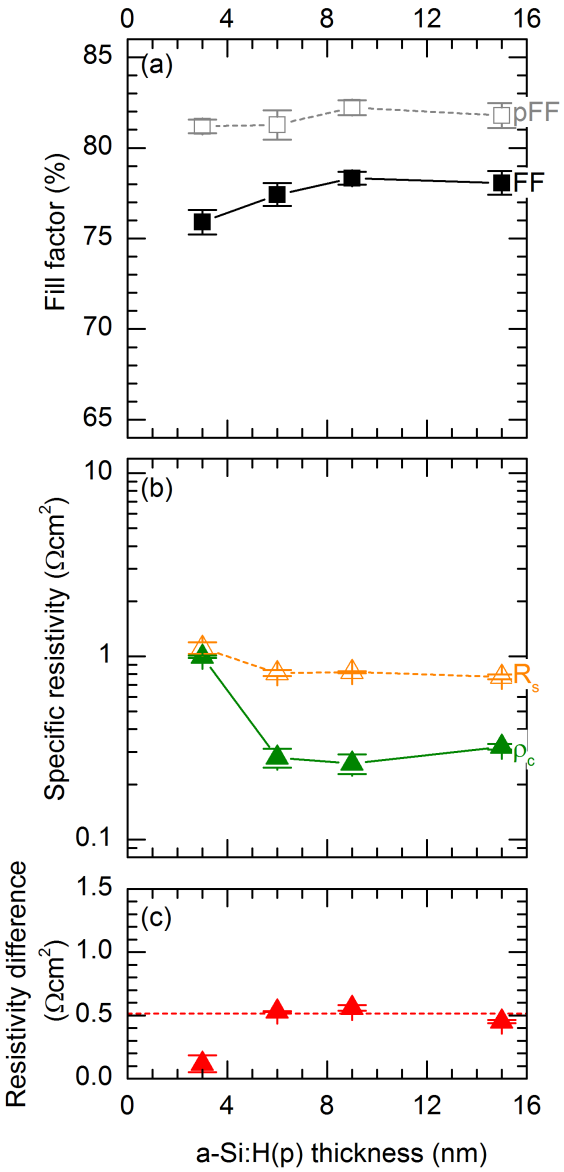

Figure 5.3: (a) pFF and FF as a function of a-Si:H(p) layer thickness. (b) $R_{\mathrm{S}}$and ρ_{C}. (c) Difference between $R_{\mathrm{S}}$and ρ_{C}. The red dashed line is the average resistivity difference for the three thicker samples.

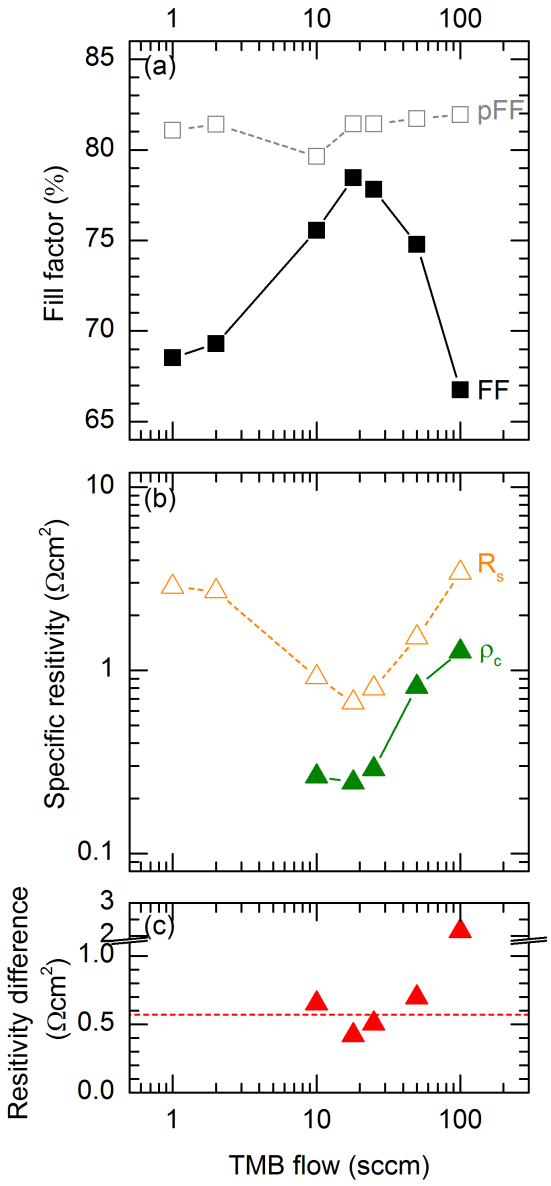

Figure 5.4: (a) pFF and FFas a function of TMB flow, (b) $R_{\mathrm{S}}$and ρ_{C}(c) Difference between $R_{\mathrm{S}}$and ρ_{C}. The red dashed line is the average resistivity difference for gas flows between 10 and 50$sccm$. Only one cell and TLM pad was measured for this experiment.

by another 8% at 100$sccm$. The trend of increasing $FF$was also seen by Bivour, et al. for diborane (B_2H_6) concentrations up to 4300ppm.

This trend can be explained by again considering the depletion of the a-Si:H(p)

layer. At low gas flows the amount of active dopants providing holes to the layer is sufficiently low that the layer becomes depleted. For TMB gas flows greater than $18sccm$ the decrease in FFcan be attributed to defect formation which occurs at a faster rate compared to active dopant formation [37].

This hypothesis is supported by observing the $R_{\mathrm{S}}$and ρ_{C}in figure 5.4b. The trend is a mirror image of the FFtrend where R_{S}decreases and attains a local minimum at $18sccm$ of TMB. The contact resistivity also reaches a local minimum at $18sccm$. Unlike the other process conditions we have varied so far, the difference between $R_{\mathrm{S}}$and $\rho_{\mathrm{C}}$is a bit more spread out about an average of $0.6\Omega cm^2$.

5.2.2.3 ITO oxygen concentration

The experimental work done on optimization of TCO layers for SHJ solar cells has mostly focused on sheet resistance, contact resistivity between the metal and TCO, and free-carrier absorption without regard to the layers role in the contact resistivity of the whole stack [20, 82, 116]. However simulations have shown the importance of carrier transport between the doped amorphous silicon layers and the TCO. In particular, Kanevce and Metzger have shown that in order to produce reasonable J-V curves there must be band-to-band tunneling across the a-Si/ITO interface [117, 118]. Additionally, Centurioni and Iencinella emphasize the impact of the TCO work function on the built-in potential of the a-Si/c-Si heterojunction solar cell. They mention that is important to have a TCO with a large work function on the emitter side to get the highest $V_{\mathrm{OC}}$and efficiency from this cell structure [119].

Similar to the previous experiments, 5.5a shows that the pFF remains constant indicating that changing oxygen partial pressure should result in solar cells with equivalent performance in the absence of series resistance. There is a significant drop in the $FF$of the cell from 77.7% to 65% by increasing the oxygen partial pressure

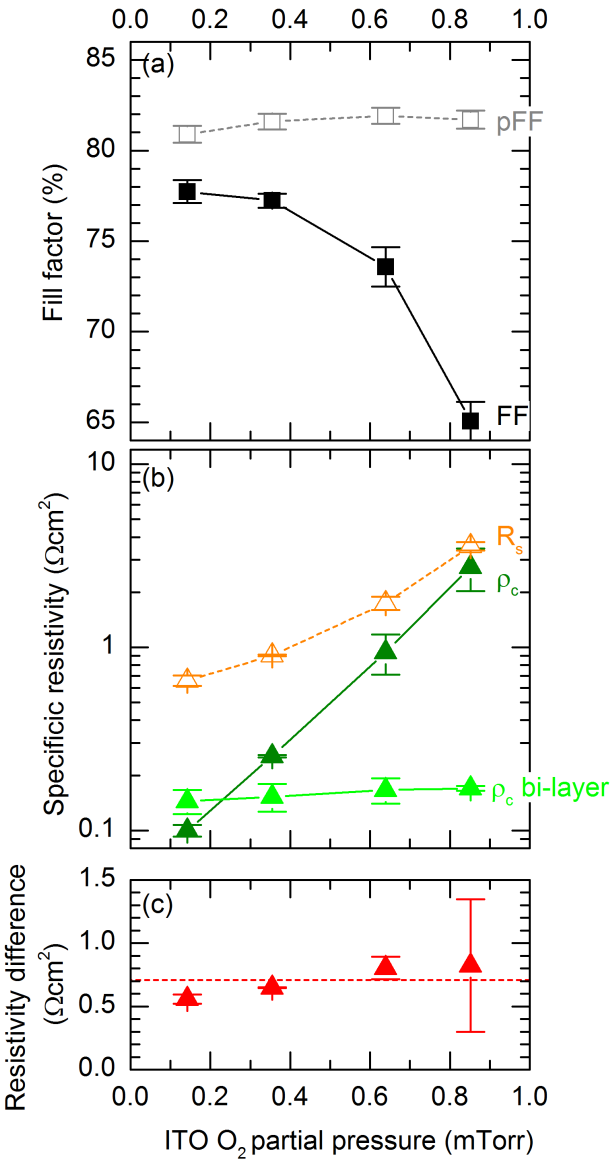

Figure 5.5: (a) pFF and FFas a function of O_2 partial pressure during ITO sputtering, (b) $R_S$and ρ_C(c) Difference between $R_S$and ρ_C. The red dashed line is the average resistivity difference of all samples.

from 0.14 to $0.85 mTorr$. This contradicts the work of Holman, et al. who found that increasing the carrier density of the rear side ITO to $10^{20} cm^{-2}$ resulted in a constant fill factor [82].

The detriment to the fill factor can again be attributed to the increasing Rs which increases from 0.66 to $3.57\Omega cm^2$ shown in figure 5.5b. By varying the properties of a boron doped zinc oxide layer, Favier, et al. find a strong linear correlation of the FFon R_{S}[120]. We also find a similar correlation between these two quantities (not shown). Note that the lowest ρ_{C}shown here is the lowest value ever presented for the classic hole contact in SHJ solar cells [16, 103]. The difference between $R_{\mathrm{S}}$and $\rho_{\mathrm{C}}$is constant with a value of $0.7\Omega cm^2$ over the entire range of partial pressures. The large increase in ρ_{C}, and subsequent decrease in fill factor, as a the oxygen partial pressure increases is most likely due to a decrease in the work function of the ITO with increasing oxygen partial pressure. Centurioni and Iencinella simulate the a-Si/c-Si solar cell with varying TCO work functions and show a drop in $FF$of over 30% with a work function decrease from 5.1 to $4.75eV$ [119]. Brendel, et al. also simulate similar decreases in $FF$to ours as a function of interfacial work function helping to validate our theory that the decrease in ITO work fuction with doping leads to a lower fill factor [51].

The effect of O_2 partial pressure can be removed by utilizing an ITO bilayer. The green line in figure 5.5b shows that by first depositing a $15nm$ ITO layer with an O_2 partial pressure of $0.142mTorr$ and then a $145nm$ layer of varying O_2 partial pressures between 0.142 and $0.852mTorr$ the contact resistivity remains constant with a value of $0.15\Omega cm^2$. This is in contrast to an ITO monolayer where the contact resistivity increases by two orders of magnitude over the same O_2 partial pressure range. Because the contact resistivity does not change as a function of ITO O_2 partial pressure for a bilayer but does change for a monolayer, we can confidently state that the most important interface for the contact resistivity is the a-Si:H(p)/ITO interface. Since the bi-layer and the monolayer experiments were completed on different days we redid the mono layer experiment (not shown) to demonstrate that the results

are reproducible on a day-to-day basis (they are). We also vary the thickness of the bilayers by making the $0.142mTorr$ layer $45nm$ and the $0.852mTorr$ layer $115nm$. As expected, this change in the thickness of the two layers did not influence the contact resistivity in any way.

The fact that the ITO bilayer has constant contact resistivity independent of the top layer doping implies that a cell made with a bilayer, in which the second layer is more transparent, should have a higher J_{SC}than a cell made with a single ITO layer. Unfortunately, the reflectivity and the EQE (not shown) of a cell made with a $0.14 - 0.85mTorr$ bilayer is significantly lower in the infrared than any of the single layers leading to lower J_{SC}. This deterioration of the optical properties is most likely due to the hydrogen doping of the ITO from the a-Si:H layers [86].

5.2.2.4 Processes that dominate hole contact resistivity

Figure 5.6 shows a tornado plot dictating which processes in the development hole contact for SHJ solar cells have an effect on the contact resistivity. Each of the changes is a 33% variation above and below our standard process outlined in section 5.2.1.

Although figure 5.6 indicates that the TMB flow rate can dramatically affect the contact resistivity, an appreciable change is observed only for large excursions from the optium value. Figure 5.6 thus reveals that the contact resistivity is least sensitive to TMB flow rate, of all the parameters explored. Unlike the other processes that show both an increase and decrease in contact resistivity, the TMB flow increases in either direction as our standard process flow sits at the contact resistivity minimum in Figure 4(b).

The a-Si:H(p) layer thickness does not matter unless the thickness drops below $3nm$ (figure 5.3) which is not seen in figure 5.6 because this thickness is not within the

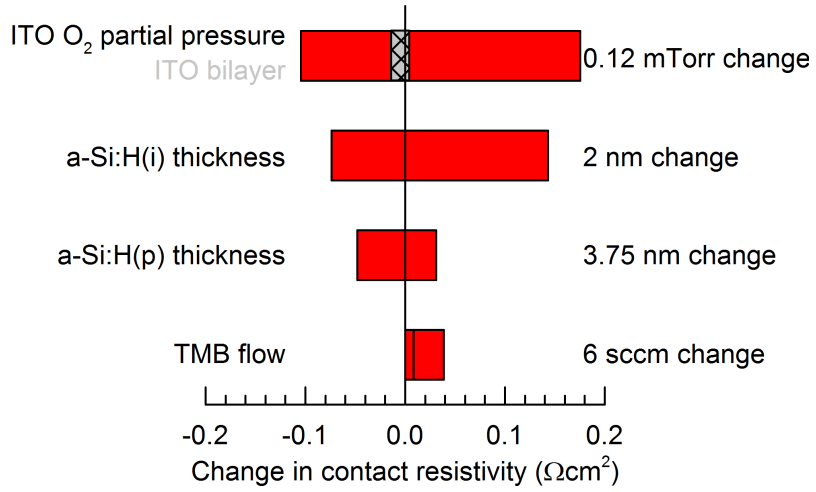

Figure 5.6: Absolute change in contact resistivity as a function of the four varied parameters in this Chapter. All variations are 33% of our baseline process.

33% perturbation. The thickness of the a-Si:H(p) layer is likely to become important when the hole contact is placed on the front of the solar cell because of the increased parasitic absorption of visible light with increased thickness. In this case a 33% decrease in the thickness would lead to a serious increase in contact resistance.

By increasing the a-Si:H(i) layer thickness by only $2nm$ the contact resistivity increases by $0.14\Omega cm^2$ while decreasing the thickness by $2nm$ decreases the contact resistivity $0.07\Omega cm^2$. This may be significant for industrial scale PECVD systems where it is entirely possible to have a thickness variation of the same magnitude across the chamber [121–123]. Note that the change in contact resistivity is asymmetric where an increase of $2nm$ increases the contact resistivity more than a decrease of $2nm$ decreases the contact resistivity. From a purely contact resistivity point of view it would be wise to have too thin of a layer than too thick of a layer but a thinner layer leads to poorer passivation and thus a loss in V_{OC}.

The largest detriment to the contact resistivity comes from varying the ITO partial pressure. By increasing the O_2 partial pressure by $0.12mTorr$ the contact

resistivity increases by $0.17\Omega cm^2$ while a decrease of the same amount results in a decrease of $0.10\Omega cm^2$. This is not true when using the bilayers discussed in the previous section. For a bilayer where the bottom layer is $15nm$ an increase in the O_2 partial pressure results in an increase of $4 \times 10^{-4}\Omega cm^2$ while a decrease in the O_2 partial pressure results in a drop in contact resistivity of $0.014\Omega cm^2$. When the bottom layer is $45nm$ an increase in partial pressure increases the contact resistivity by $0.006\Omega cm^2$ while a decrease results in a decrease of $0.005\Omega cm^2$. This analysis shows that it is most important to control the ITO sputtering tool or to utilize an ITO bilayer. Fortunately, a change in $0.12mTorr$ of oxygen during ITO sputtering is quite large and can be easily controlled during SHJ cell manufacturing.

5.3 Electron Contact Resistivity

Similar possible variables for the n-doped layer stack has still remained to be addressed. The n-type amorphous silicion based contact consisting of intrinsic amorphous silicon (a-Si:H(i)), phosphorous doped amorphous silicion (a-Si:H(n)) and indium tin oxide (ITO) is studied. We varied the thicknesses of the a-Si:H(i) (see figure 5.7) and a-Si:H(n) (see figure 5.8) and ITO O_2 partial pressure (see figure 5.9) to determine which layers have the most impact on the contact resistivity. Specifically, we observe that increasing the thickness of the a-Si:H(i) and the ITO O_2 partial pressure results in an increase in the contact resistivity similar to p-layer stack. In parallel to TLM contact resistance patterns, solar cells are fabricated and FFtrends studied to confirm if it's trend of variation follows the contact resistivity.

5.4 Total contact resistance

Each source of losses is now well measured and we are able to evaluate the weight of each variable and determine direction that future efforts should be focused on to improve the fill factor of silicon solar cells.

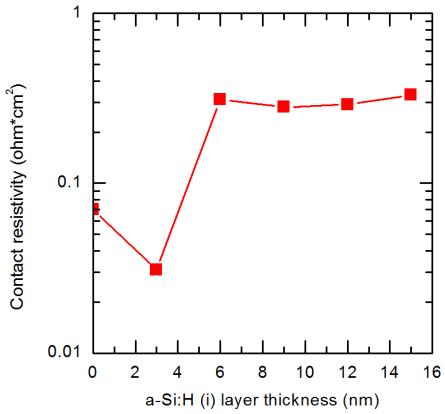

Figure 5.7: Contact resistivity as a function of a-Si:H(i) layer thickness.

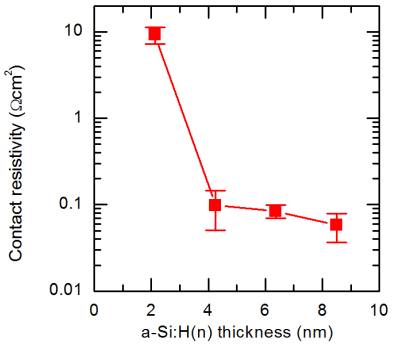

Figure 5.8: Contact resistivity as a function of a-Si:H(n) layer thickness.

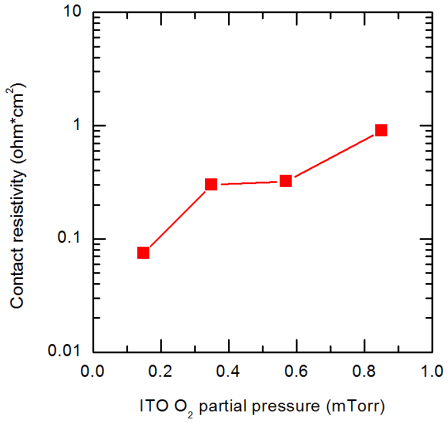

Figure 5.9: Contact resistivity as a function of ITO O_2 partial pressure.

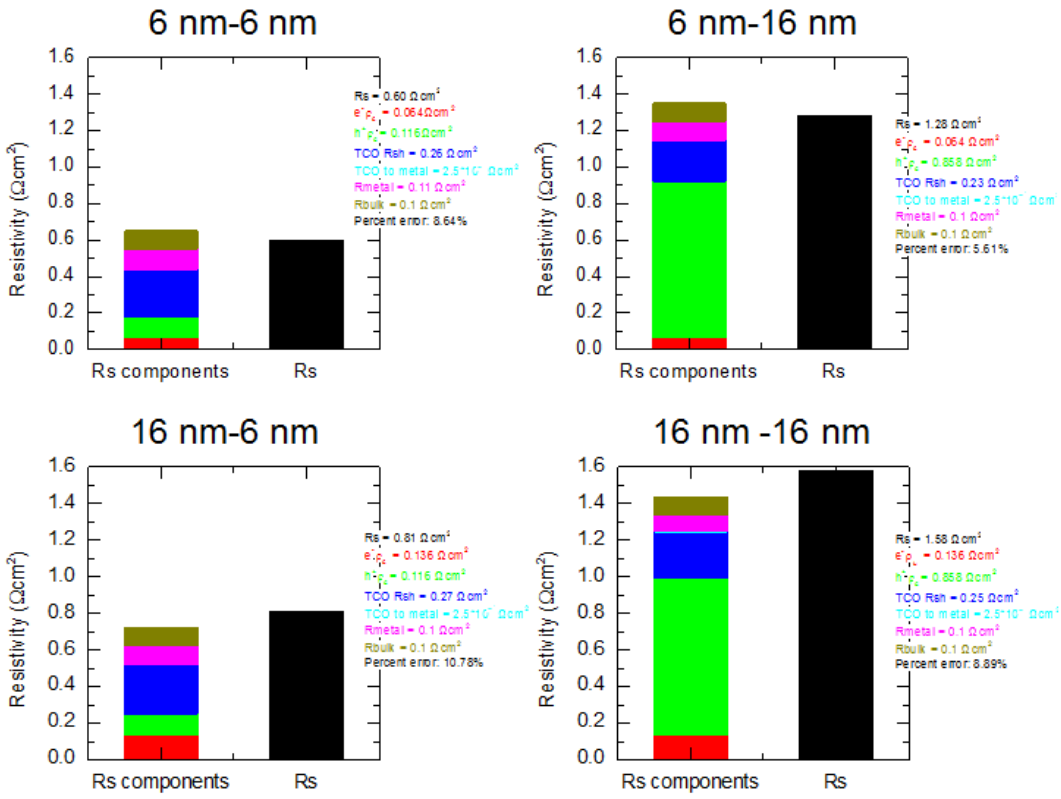

Figure 5.10: Different components of series resistance as a function of ITO O_2 partial pressure.

To investigate the accuracy of our analysis, solar cells with varying intrinsic a-Si layer thickness and ITO O_2 partial pressure (the two most determining parameters) are fabricated, actual IV curves obtained and total resistance is measured using Sinton IV tester. All different series resistance components in a typical SHJ cell structure are measured and then summed up and compared with the total series resistance loss measured with IV tester. Following figures show the results. As seen, the difference between what calculated through summing up different components with the total values is less than 10% for almost all cases. According the above analysis, we conclude then that contact resistance is actually the main source of resistance losses and correspondingly fill factor loss in silicon heterojunction solar cells. Clearly,

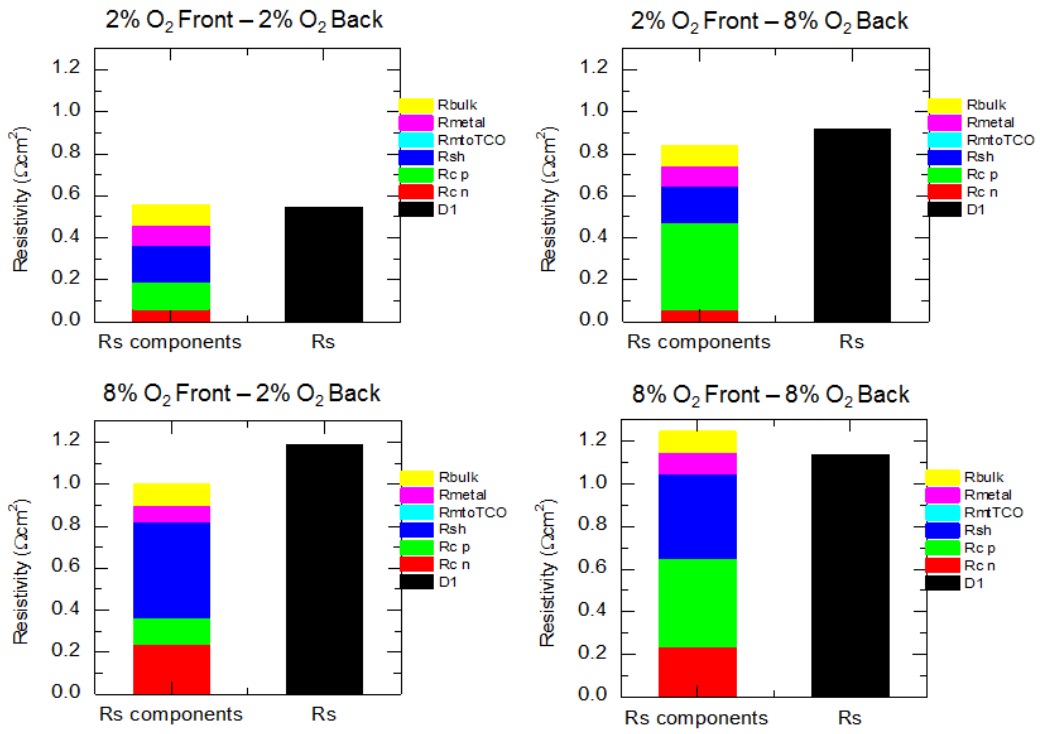

Figure 5.11: Different components of series resistance as a function of intrinsic a-Si layer thickness.

by minimizing the contact resistivity of both contacts there would be a significant increase in the fill factor of the cell.

5.5 Conclusion

We have shown the effect that changing hole and electron contact layer properties has on silicon heterojunction solar cells performance. The hole contact resistivities presented in this work are within the range shown by others and are considerably higher than those of a metal to diffused surface. The a-Si hole contact also had higher contact resistivity of some of the more novel hole contacts such as MoO_x and $CuO : N_x$. This does not mean that the hole contact of the traditional SHJ solar cell should be replaced- in fact it is still the basis of the highest efficiency SHJ solar cell. An analysis of the electron contact will also provided to complete analysis of the

series resistance losses in SHJ solar cells.

The contact resistivity is most strongly affected by changes in the oxygen partial pressure during ITO deposition indicating that this process should be closely monitored to develop high quality SHJ solar cells.

While the contact resistivity is an important parameter in discussing the performance of the solar cell, we did not include an analysis of the transport physics across these interfaces. A comprehensive study of the processes varied here is the next logical step to fully understand these contacts. As noted by the difference in trends between an ITO monolayer and bilayer, the a-Si/ITO interface limits the performance of the SHJ solar cell and an understanding of the charge carrier transport across this interface is necessary to fully optimize this solar cell technology.

We also did not take into account interactions between the layers. For example, our a-Si:H(i) layer thickness experiments had ITO layers with only one condition for oxygen flow during sputtering. It is possible that repeating the same set of experiments while also varying the oxygen concentration during ITO sputtering could produce different values of the contact resistivity and cell parameters. We have already shown that utilizing an ITO bilayer with the layer with a low partial pressure of oxygen at the a-Si/ITO interface removes the effect of oxygen partial pressure. By choosing a different standard parameter for any layer in the stack, the effect of varying a different layer could be hidden because the initial layer has become the dominant layer affecting the contact resistance across the stack.

Chapter 6

Conclusions and Future work

The objective of this thesis was to achieve a detailed understanding of the loss mechanisms in SHJ solar cells. The working principles of these cells and what affects the cell operation, e.g. the IV characteristics at the maximum power point (MPP) and the correspondingly fill factor (FF) were investigated. Different loss sources were analyzed separately, and the weight of each in the total loss at the MPP were evaluated. The total series resistance was measured and then compared with the value obtained through summation over each of its components. In other words, series resistance losses due to recombination, vertical and lateral carrier transport, metalization, etc, were individually evaluated, and then by adding all these components together, the total loss was calculated. The concept of fill factor and its direct dependence on the loss mechanisms at the MPP of the device was explained, and its sensitivity to nearly every processing step of the cell fabrication was investigated. This analysis provided a focus lens to identify the main source of losses in SHJ solar cells and paved the path for further improvements in cell efficiency.

In this thesis, we provided a detailed understanding of the FF concept; we explained how it can be directly measured; how it can be calculated and what expressions can better approximate its value and under what operating conditions. The relation between $FF$and cell operating condition at the MPP was investigated. We separately analyzed the main FF sources of losses including recombination, sheet resistance, contact resistance and metalization. We studied FF loss due to recombination and its separate components which included the Augur, radiative and SRH recombination was investigated. We studied FF loss due to contact resistance and its separate components which included the contact resistance of different interfaces, e.g.

between the intrinsic and doped a-Si layers, TCO and a-Si layers. We also studied FF loss due to lateral transport and its components that including the TCO sheet resistance, the finger and the busbars resistances.

6.1 Summary

This thesis was divided in following chapters:

In Chapter 2 we reviewed some theory and physics behind solar cell and explained its IV characteristics. Then the concept of fill factor was discussed in more detail and it's relation with cell operating condition at the maximum power point will was clarified. Specifically, we explained what the difference was between the actual, pseudo and implied FF and how each of them can be measured, calculated, or approximated.

In Chapter 3 after further analysis of the fill factor concept, the approximate expressions proposed by Green and Swanson and Sinton to predict the FF of a solar cell from its V_{OC} was discussed. The expressions were originally suggested for silicon solar cells that behave according to a single-diode model and, in addition to V_{OC}, they require an ideality factor as input. They are now commonly applied to silicon cells by assuming a unity ideality factor-even when the cells are not in low injection-as well as to non-silicon cells. Here, we evaluated the accuracy of the expressions in several cases. In particular, we calculated the recombination-limited FF and V_{OC} of a hypothetical silicon solar cells from its simulated lifetime curves, and compared the exact FF to that obtained with the approximate expressions using assumed ideality factors. Considering cells with a variety of recombination mechanisms, wafer doping densities, and photogenerated current densities revealed the range of conditions under which the approximate expressions can safely be used. We found out that the expressions are unable to predict FF generally.

In Chapter 4 the front transparent conductive oxide (TCO) layers of silicon heterojunction solar cells were discussed and we examined how the IV characteristics and specifically the FF are affected by that. We investigated how to optimize the TCO layers electrically and optically to minimize losses due to sheet resistance and free carrier absorption. We studied it for different wavelength ranges: $300-1200\ nm$ (full spectrum)and $700-1200\ nm$ (half spectrum). The latter is required if the silicon cell are to be used in a tandem structure as the bottom cell. Here, we demonstrated a procedure for determining the total loss associated with the front TCO layer and employ it to determine which carrier density, mobility, and finger pitch combinations minimize loss.

In Chapter 5 series resistance effects on SHJ solar cells was studied which is the main source of loss in this technology.

Until recently, little has been done to understand the main factors contributing to the high resistance. Here we began a systematic analysis to determine the important interactions between the different layers in the hole and electron-collecting contact consisting of a stack of a-Si:H(i)/a-Si:H(p or n)/ITO/Ag. We attempted to address how the stack performs when the intrinsic and doped amorphous silicon layers thickness, is varied, how the work function of the ITO which is controlled by varying the Oxygen partial pressure can affect the contact resistance at it's interface with the a-Si layer and what is it's contribution to total series resistance loss. We also determined how the ITO thickness affects the fill factor of the cell and assessed how much of the reduction in FF is due to the contact resistivity.

6.2 Future work

What was not investigated in this thesis is considering the effects of above studies under different illumination levels, e.g. the contact resistance is illumination level de-

pendent which directly determines the injection levels of carriers and correspondingly shifts the bulk silicon fermi level. Also, part of the blue light will be always absorbed in the front a-Si layers. As a result, under operating conditions, the front contact is under illumination while the back contact is in the dark. So, the band structure geometry may possibly be different for front contact comparing with back contact. This may break the symmetry and lead to a different weights of the front versus back contact resistances and accordingly the fill factor losses. Furthermore, as observed in current and proceeding chapters, the contact resistance for an n-layer stack may be different compared with p-layer stack. This difference may be even more dramatic depending on which stack is on the front side and hence under illumination, and which one is on the back. In other words, the contact resistance may determine if it's better to have a front or back emitter contact.

REFERENCES

[1] M. A. Green, Y. Hishikawa, W. Warta, E. D. Dunlop, D. H. Levi, J. Hohl-Ebinger, and A. W. Ho-Baillie, "Solar cell efficiency tables (version 50)," *Progress in Photovoltaics: Research and Applications*, vol. 25, no. 7, pp. 668–676, 2017.

[2] C. Battaglia, A. Cuevas, and S. De Wolf, "High-efficiency crystalline silicon solar cells: status and perspectives," *Energy & Environmental Science*, vol. 9, no. 5, pp. 1552–1576, 2016.

[3] M. Bivour, "Silicon heterjunction solar cells: Analysis and basic unterstanding," Ph.D. dissertation, PhD thesis, University Freiburg, 2016.

[4] K. Nakamura, "Current status and technology trend of crystalline si solar cell," in *Active-Matrix Flatpanel Displays and Devices (AM-FPD), 2017 24th International Workshop on*. IEEE, 2017, pp. 94–97.

[5] A. Goodrich, P. Hacke, Q. Wang, B. Sopori, R. Margolis, T. L. James, and M. Woodhouse, "A wafer-based monocrystalline silicon photovoltaics road map: Utilizing known technology improvement opportunities for further reductions in manufacturing costs," *Solar Energy Materials and Solar Cells*, vol. 114, pp. 110–135, 2013.

[6] D. M. Powell, M. T. Winkler, H. Choi, C. B. Simmons, D. B. Needleman, and T. Buonassisi, "Crystalline silicon photovoltaics: a cost analysis framework for determining technology pathways to reach baseload electricity costs," *Energy & Environmental Science*, vol. 5, no. 3, pp. 5874–5883, 2012.

[7] A. Richter, M. Hermle, and S. W. Glunz, "Reassessment of the limiting efficiency for crystalline silicon solar cells," *IEEE Journal of Photovoltaics*, vol. 3, no. 4, pp. 1184–1191, 2013.

[8] K. Yoshikawa, H. Kawasaki, W. Yoshida, T. Irie, K. Konishi, K. Nakano, T. Uto, D. Adachi, M. Kanematsu, H. Uzu *et al.*, "Silicon heterojunction solar cell with interdigitated back contacts for a photoconversion efficiency over 26%," *Nature Energy*, vol. 2, p. 17032, 2017.

[9] J. Plá, E. Centurioni, C. Summonte, R. Rizzoli, A. Migliori, A. Desalvo, and F. Zignani, "Homojunction and heterojunction silicon solar cells deposited by low temperature–high frequency plasma enhanced chemical vapour deposition," *Thin Solid Films*, vol. 405, no. 1, pp. 248–255, 2002.

[10] L. Korte, E. Conrad, H. Angermann, R. Stangl, and M. Schmidt, "Advances in a-si: H/c-si heterojunction solar cell fabrication and characterization," *Solar Energy Materials and Solar Cells*, vol. 93, no. 6, pp. 905–910, 2009.

[11] A. Cuevas, T. Allen, J. Bullock, Y. Wan, X. Zhang *et al.*, "Skin care for healthy silicon solar cells," in *Photovoltaic Specialist Conference (PVSC), 2015 IEEE 42nd.* IEEE, 2015, pp. 1–6.

[12] U. Würfel, A. Cuevas, and P. Würfel, "Charge carrier separation in solar cells," *IEEE Journal of Photovoltaics*, vol. 5, no. 1, pp. 461–469, 2015.

[13] J. Bullock, M. Hettick, J. Geissbühler, A. J. Ong, T. Allen, C. M. Sutter-Fella, T. Chen, H. Ota, E. W. Schaler, S. De Wolf *et al.*, "Efficient silicon solar cells with dopant-free asymmetric heterocontacts," *Nature Energy*, vol. 1, p. 15031, 2016.

[14] S. De Wolf, A. Descoeudres, Z. C. Holman, and C. Ballif, "High-efficiency silicon heterojunction solar cells: A review," *green*, vol. 2, no. 1, pp. 7–24, 2012.

[15] S. Y. Herasimenka, W. J. Dauksher, and S. G. Bowden, "¿ 750 mv open circuit voltage measured on 50 μ m thick silicon heterojunction solar cell," *Applied Physics Letters*, vol. 103, no. 5, p. 053511, 2013.

[16] S.-Y. Lee, H. Choi, H. Li, K. Ji, S. Nam, J. Choi, S.-W. Ahn, H.-M. Lee, and B. Park, "Analysis of a-si: H/tco contact resistance for the si heterojunction back-contact solar cell," *Solar Energy Materials and Solar Cells*, vol. 120, pp. 412–416, 2014.

[17] R. Gogolin, M. Turcu, R. Ferré, J. Clemens, N.-P. Harder, R. Brendel, and J. Schmidt, "Analysis of series resistance losses in a-si: H/c-si heterojunction solar cells," *IEEE Journal of Photovoltaics*, vol. 4, no. 5, pp. 1169–1176, 2014.

[18] F. Feldmann, M. Bivour, C. Reichel, H. Steinkemper, M. Hermle, and S. W. Glunz, "Tunnel oxide passivated contacts as an alternative to partial rear contacts," *Solar Energy Materials and Solar Cells*, vol. 131, pp. 46–50, 2014.

[19] J. Bullock, A. Cuevas, T. Allen, and C. Battaglia, "Molybdenum oxide moox: A versatile hole contact for silicon solar cells," *Applied Physics Letters*, vol. 105, no. 23, p. 232109, 2014.

[20] Z. C. Holman, A. Descoeudres, L. Barraud, F. Z. Fernandez, J. P. Seif, S. De Wolf, and C. Ballif, "Current losses at the front of silicon heterojunction solar cells," *IEEE Journal of Photovoltaics*, vol. 2, no. 1, pp. 7–15, 2012.

[21] M. Filipič, Z. C. Holman, F. Smole, S. De Wolf, C. Ballif, and M. Topič, "Analysis of lateral transport through the inversion layer in amorphous silicon/crystalline silicon heterojunction solar cells," *Journal of Applied Physics*, vol. 114, no. 7, p. 074504, 2013.

[22] M. Leilaeioun, W. Weigand, J. Y. Zhengshan, and Z. Holman, "Design of the front transparent conductive oxide layer of silicon heterojunction solar cells for single-junction and four-terminal tandem applications," in *Photovoltaic Specialists Conference (PVSC), 2016 IEEE 43rd.* IEEE, 2016, pp. 0681–0684.

[23] T. Trupke, M. A. Green, P. Würfel, P. Altermatt, A. Wang, J. Zhao, and R. Corkish, "Temperature dependence of the radiative recombination coefficient of intrinsic crystalline silicon," *Journal of Applied Physics*, vol. 94, no. 8, pp. 4930–4937, 2003.

[24] M. Green, "Silicon solar cells: Advanced principles and practice sydney," *Australia: The University of New South Wales*, 1995.

[25] A. G. Aberle, *Crystalline silicon solar cells: advanced surface passivation and analysis.* Centre for Photovoltaic Engineering. University of New South wales, 1999.

[26] A. Richter, S. W. Glunz, F. Werner, J. Schmidt, and A. Cuevas, "Improved quantitative description of auger recombination in crystalline silicon," *Physical Review B*, vol. 86, no. 16, p. 165202, 2012.

[27] J. Dziewior and W. Schmid, "Auger coefficients for highly doped and highly excited silicon," *Applied Physics Letters*, vol. 31, no. 5, pp. 346–348, 1977.

[28] W. Shockley and W. Read Jr, "Statistics of the recombinations of holes and electrons," *Physical review*, vol. 87, no. 5, p. 835, 1952.

[29] R. N. Hall, "Electron-hole recombination in germanium," *Physical review*, vol. 87, no. 2, p. 387, 1952.

[30] M. J. Kerr and A. Cuevas, "Very low bulk and surface recombination in oxidized silicon wafers," *Semiconductor science and technology*, vol. 17, no. 1, p. 35, 2001.

[31] D. K. Schroder, *Semiconductor material and device characterization.* John Wiley & Sons, 2006.

[32] M. A. Green, "Limiting efficiency of bulk and thin-film silicon solar cells in the presence of surface recombination," *Progress in Photovoltaics: Research and Applications*, vol. 7, no. 4, pp. 327–330, 1999.

[33] T. Tiedje, E. Yablonovitch, G. D. Cody, and B. G. Brooks, "Limiting efficiency of silicon solar cells," *IEEE Transactions on electron devices*, vol. 31, no. 5, pp. 711–716, 1984.

[34] Z. Hameiri, K. McIntosh, and G. Xu, "Evaluation of recombination processes using the local ideality factor of carrier lifetime measurements," *Solar Energy Materials and Solar Cells*, vol. 117, pp. 251–258, 2013.

[35] C. Honsberg and S. Bowden, "Pvcdrom," *retrieved 16 th November 2011*, 2010.

[36] R. A. Sinton, A. Cuevas, and M. Stuckings, "Quasi-steady-state photoconductance, a new method for solar cell material and device characterization," in *Photovoltaic Specialists Conference, 1996., Conference Record of the Twenty Fifth IEEE.* IEEE, 1996, pp. 457–460.

[37] D. Pysch, A. Mette, and S. W. Glunz, "A review and comparison of different methods to determine the series resistance of solar cells," *Solar Energy Materials and Solar Cells*, vol. 91, no. 18, pp. 1698–1706, 2007.

[38] M. A. Green, "Solar cell fill factors: General graph and empirical expressions," *Solid-State Electronics*, vol. 24, no. 8, pp. 788–789, 1981.

[39] R. M. Swanson and R. A. Sinton, "High-efficiency silicon solar cells," *Advances in solar energy*, vol. 6, pp. 427–484, 1990.

[40] A. Descoeudres, Z. C. Holman, L. Barraud, S. Morel, S. De Wolf, and C. Ballif, "¿ 21% efficient silicon heterojunction solar cells on n-and p-type wafers compared," *IEEE Journal of Photovoltaics*, vol. 3, no. 1, pp. 83–89, 2013.

[41] M. Lu, S. Bowden, U. Das, and R. Birkmire, "Interdigitated back contact silicon heterojunction solar cell and the effect of front surface passivation," *Applied Physics Letters*, vol. 91, no. 6, p. 063507, 2007.

[42] J.-H. Guo, P. J. Cousins, and J. E. Cotter, "Investigations of parasitic shunt resistance in n-type buried contact solar cells," *Progress in Photovoltaics: Research and Applications*, vol. 14, no. 2, pp. 95–105, 2006.

[43] L. D. Nielsen, "Distributed series resistance effects in solar cells," *IEEE Transactions on electron devices*, vol. 29, no. 5, pp. 821–827, 1982.

[44] A. G. Aberle, "Surface passivation of crystalline silicon solar cells: a review," *Progress in Photovoltaics: Research and Applications*, vol. 8, no. 5, pp. 473–487, 2000.

[45] M. Wolf and H. Rauschenbach, "Series resistance effects on solar cell measurements," *Advanced energy conversion*, vol. 3, no. 2, pp. 455–479, 1963.

[46] I. E. Commission *et al.*, "Procedures for temperature and irradiance corrections to measured iv characteristics of crystalline silicon pv devices," *IEC Standard*, vol. 891, 1987.

[47] A. Rohatgi, J. Davis, R. Hopkins, P. Rai-Choudhury, P. McMullin, and J. McCormick, "Effect of titanium, copper and iron on silicon solar cells," *Solid-State Electronics*, vol. 23, no. 5, pp. 415–422, 1980.

[48] L. Barraud, Z. Holman, N. Badel, P. Reiss, A. Descoeudres, C. Battaglia, S. De Wolf, and C. Ballif, "Hydrogen-doped indium oxide/indium tin oxide bilayers for high-efficiency silicon heterojunction solar cells," *Solar Energy Materials and Solar Cells*, vol. 115, pp. 151–156, 2013.

[49] Y. Tawada, M. Kondo, H. Okamoto, and Y. Hamakawa, "Hydrogenated amorphous silicon carbide as a window material for high efficiency a-si solar cells," *Solar Energy Materials*, vol. 6, no. 3, pp. 299–315, 1982.

[50] T. Brown, C. Bittencourt, M. Sebastiani, and F. Evangelisti, "Electronic states and band lineups in c-si (100)/a-si 1- x c x: H heterojunctions," *Physical Review B*, vol. 55, no. 15, p. 9904, 1997.

[51] M. Bivour, S. Schröer, and M. Hermle, "Numerical analysis of electrical tco/a-si: H (p) contact properties for silicon heterojunction solar cells," *Energy Procedia*, vol. 38, pp. 658–669, 2013.

[52] K. W. Böer, *Advances in solar energy: an annual review of research and development*. Springer Science & Business Media, 2012, vol. 6.

[53] R. A. Sinton and A. Cuevas, "Contactless determination of current–voltage characteristics and minority-carrier lifetimes in semiconductors from quasi-steady-state photoconductance data," *Applied Physics Letters*, vol. 69, no. 17, pp. 2510–2512, 1996.

[54] R. Sinton, A. Cuevas *et al.*, "A quasi-steady-state open-circuit voltage method for solar cell characterization," in *Proceedings of the 16th European Photovoltaic Solar Energy Conference*, vol. 1152, 2000.

[55] S. Bowden and A. Rohatgi, "Rapid and accurate determination of series resistance and fill factor losses in industrial silicon solar cells." Georgia Institute of Technology, 2001.

[56] X. Guo, N. Zhou, S. J. Lou, J. Smith, D. B. Tice, J. W. Hennek, R. P. Ortiz, J. T. L. Navarrete, S. Li, J. Strzalka *et al.*, "Polymer solar cells with enhanced fill factors," *Nature Photonics*, vol. 7, no. 10, pp. 825–833, 2013.

[57] B. Qi and J. Wang, "Fill factor in organic solar cells," *Physical Chemistry Chemical Physics*, vol. 15, no. 23, pp. 8972–8982, 2013.

[58] Z. Fu, W. Shen, R. He, X. Liu, H. Sun, W. Yin, and M. Li, "Theoretical studies on the effect of a bithiophene bridge with different substituent groups (r= h, ch 3, och 3 and cn) in donor–π–acceptor copolymers for organic solar cell applications," *Physical Chemistry Chemical Physics*, vol. 17, no. 3, pp. 2043–2053, 2015.

[59] S. Yoo, B. Domercq, and B. Kippelen, "Intensity-dependent equivalent circuit parameters of organic solar cells based on pentacene and c 60," *Journal of Applied Physics*, vol. 97, no. 10, p. 103706, 2005.

[60] Z. Huang, G. Natu, Z. Ji, M. He, M. Yu, and Y. Wu, "Probing the low fill factor of nio p-type dye-sensitized solar cells," *The Journal of Physical Chemistry C*, vol. 116, no. 50, pp. 26 239–26 246, 2012.

[61] K. J. Singh and S. K. Sarkar, "Highly efficient arc less ingap/gaas dj solar cell numerical modeling using optimized inalgap bsf layers," *Optical and Quantum Electronics*, vol. 43, no. 1, pp. 1–21, 2012.

[62] Y. Wang, A. Gerger, A. Lochtefeld, L. Wang, C. Kerestes, R. Opila, and A. Barnett, "Design, fabrication and analysis of germanium: silicon solar cell in a multi-junction concentrator system," *Solar Energy Materials and Solar Cells*, vol. 108, pp. 146–155, 2013.

[63] D. Mbewe, H. Card, and D. Card, "A model of silicon solar cells for concentrator photovoltaic and photovoltaic/thermal system design," *Solar energy*, vol. 35, no. 3, pp. 247–258, 1985.

[64] P. Löper, B. Niesen, S.-J. Moon, S. M. De Nicolas, J. Holovsky, Z. Remes, M. Ledinsky, F.-J. Haug, J.-H. Yum, S. De Wolf *et al.*, "Organic–inorganic halide perovskites: Perspectives for silicon-based tandem solar cells," *IEEE Journal of Photovoltaics*, vol. 4, no. 6, pp. 1545–1551, 2014.

[65] M. Diaz, L. Wang, D. Li, X. Zhao, B. Conrad, A. Soeriyadi, A. Gerger, A. Lochtefeld, C. Ebert, R. Opila *et al.*, "Tandem gaasp/sige on si solar cells," *Solar Energy Materials and Solar Cells*, vol. 143, pp. 113–119, 2015.

[66] H. Schlangenotto, H. Maeder, and W. Gerlach, "Temperature dependence of the radiative recombination coefficient in silicon," *physica status solidi (a)*, vol. 21, no. 1, pp. 357–367, 1974.

[67] P. Altermatt, F. Geelhaar, T. Trupke, X. Dai, A. Neisser, and E. Daub, "Injection dependence of spontaneous radiative recombination in crystalline silicon: Experimental verification and theoretical analysis," *Applied physics letters*, vol. 88, no. 26, p. 261901, 2006.

[68] A. Schenk, "Finite-temperature full random-phase approximation model of band gap narrowing for silicon device simulation," *Journal of Applied Physics*, vol. 84, no. 7, pp. 3684–3695, 1998.

[69] D. Yan and A. Cuevas, "Empirical determination of the energy band gap narrowing in highly doped n+ silicon," *Journal of Applied Physics*, vol. 114, no. 4, p. 044508, 2013.

[70] S. Rein, T. Rehrl, W. Warta, and S. Glunz, "Lifetime spectroscopy for defect characterization: Systematic analysis of the possibilities and restrictions," *Journal of Applied Physics*, vol. 91, no. 4, pp. 2059–2070, 2002.

[71] K. Graff, *Metal impurities in silicon-device fabrication*. Springer Science & Business Media, 2013, vol. 24.

[72] B. B. Paudyal, K. R. McIntosh, D. H. Macdonald, and G. Coletti, "Temperature dependent carrier lifetime studies of mo in crystalline silicon," *Journal of Applied Physics*, vol. 107, no. 5, p. 054511, 2010.

[73] J. E. Birkholz, K. Bothe, D. Macdonald, and J. Schmidt, "Electronic properties of iron-boron pairs in crystalline silicon by temperature-and injection-level-dependent lifetime measurements," *Journal of Applied Physics*, vol. 97, no. 10, p. 103708, 2005.

[74] A. D. Basner, "Synthesis of heteroaromatic ruthenium dyes for use as electron reservoirs in dye-sensitized solar cells," Ph.D. dissertation, Syracuse University, 2017.

[75] J. Schmidt, R. Krain, K. Bothe, G. Pensl, and S. Beljakowa, "Recombination activity of interstitial chromium and chromium-boron pairs in silicon," *Journal of Applied Physics*, vol. 102, no. 12, p. 123701, 2007.

[76] Z. Xiong, Z. Zhang, H. Ye, S. Fu, P. P. Altermatt, Z. Feng, and P. J. Verlinden, "High performance multicrystalline wafers with lifetime of 400μs at industrial scale," in *Photovoltaic Specialist Conference (PVSC), 2015 IEEE 42nd*. IEEE, 2015, pp. 1–4.

[77] M. Leilaeioun and Z. Holman, "A new expression for intrinsic fill factor of silicon solar cells," in *Photovoltaic Specialist Conference (PVSC), 2015 IEEE 42nd*. IEEE, 2015, pp. 1–4.

[78] M. Reusch, M. Bivour, M. Hermle, and S. W. Glunz, "Fill factor limitation of silicon heterojunction solar cells by junction recombination," *Energy Procedia*, vol. 38, pp. 297–304, 2013.

[79] Y. OHSHITA, T. KAMIOKA, and K. NAKAMURA, "Technology trend of high efficiency crystalline silicon solar cells." *AAPPS Bulletin*, vol. 27, no. 3, 2017.

[80] M. A. Green, "Silicon solar cells: state of the art," *Phil. Trans. R. Soc. A*, vol. 371, no. 1996, p. 20110413, 2013.

[81] D. Grant, K. Catchpole, K. Weber, and T. White, "Design guidelines for perovskite/silicon 2-terminal tandem solar cells: an optical study," *Optics express*, vol. 24, no. 22, pp. A1454–A1470, 2016.

[82] Z. C. Holman, M. Filipič, A. Descoeudres, S. De Wolf, F. Smole, M. Topič, and C. Ballif, "Infrared light management in high-efficiency silicon heterojunction and rear-passivated solar cells," *Journal of Applied Physics*, vol. 113, no. 1, p. 013107, 2013.

[83] M. Leilaeioun, J. Y. Zhengshan, and Z. Holman, "Optimization of front tco layer of silicon heterojunction solar cells for tandem applications," in *Photovoltaic Specialists Conference (PVSC), 2016 IEEE 43rd.* IEEE, 2016, pp. 0681–0684.

[84] S. Essig, C. Allebé, T. Remo, J. F. Geisz, M. A. Steiner, K. Horowitz, L. Barraud, J. S. Ward, M. Schnabel, A. Descoeudres *et al.*, "Raising the one-sun conversion efficiency of iii–v/si solar cells to 32.8% for two junctions and 35.9% for three junctions," *Nature Energy*, vol. 2, no. 9, p. 17144, 2017.

[85] M. Morales-Masis, S. M. De Nicolas, J. Holovsky, S. De Wolf, and C. Ballif, "Low-temperature high-mobility amorphous izo for silicon heterojunction solar cells," *IEEE Journal of Photovoltaics*, vol. 5, no. 5, pp. 1340–1347, 2015.

[86] K.-U. Ritzau, T. Behrendt, D. Palaferri, M. Bivour, and M. Hermle, "Hydrogen doping of indium tin oxide due to thermal treatment of hetero-junction solar cells," *Thin Solid Films*, vol. 599, pp. 161–165, 2016.

[87] K. Jäger, L. Korte, B. Rech, and S. Albrecht, "Numerical optical optimization of monolithic planar perovskite-silicon tandem solar cells with regular and inverted device architectures," *Optics Express*, vol. 25, no. 12, pp. A473–A482, 2017.

[88] S. Albrecht, M. Saliba, J.-P. Correa-Baena, K. Jäger, L. Korte, A. Hagfeldt, M. Grätzel, and B. Rech, "Towards optical optimization of planar monolithic perovskite/silicon-heterojunction tandem solar cells," *Journal of Optics*, vol. 18, no. 6, p. 064012, 2016.

[89] I. Almansouri, A. Ho-Baillie, S. P. Bremner, and M. A. Green, "Supercharging silicon solar cell performance by means of multijunction concept," *IEEE Journal of Photovoltaics*, vol. 5, no. 3, pp. 968–976, 2015.

[90] D. L. Meier and D. K. Schroder, "Contact resistance: Its measurement and relative importance to power loss in a solar cell," *IEEE transactions on electron devices*, vol. 31, no. 5, pp. 647–653, 1984.

[91] R. Brendel and R. Peibst, "Contact selectivity and efficiency in crystalline silicon photovoltaics," *IEEE Journal of Photovoltaics*, vol. 6, no. 6, pp. 1413–1420, 2016.

[92] A. Cuevas, R. A. Sinton, and M. Stuckings, "Determination of recombination parameters in semiconductors from photoconductance measurements," in *Optoelectronic and Microelectronic Materials And Devices Proceedings, 1996 Conference on.* IEEE, 1996, pp. 16–19.

[93] D. K. Schroder and D. L. Meier, "Solar cell contact resistancea review," *IEEE Transactions on electron devices*, vol. 31, no. 5, pp. 637–647, 1984.

[94] G. S. Marlow and M. B. Das, "The effects of contact size and non-zero metal resistance on the determination of specific contact resistance," *Solid-State Electronics*, vol. 25, no. 2, pp. 91–94, 1982.

[95] R. Cox and H. Strack, "Ohmic contacts for gaas devices," *Solid-State Electronics*, vol. 10, no. 12, pp. 1213IN71 215–1214IN81 218, 1967.

[96] M. M. Hilali, A. Rohatgi, and S. Asher, "Development of screen-printed silicon solar cells with high fill factors on 100/spl omega//sq emitters," *IEEE transactions on electron devices*, vol. 51, no. 6, pp. 948–955, 2004.

[97] E.-J. Lee, D. Kim, and S. Lee, "Ni/cu metallization for low-cost high-efficiency perc cells," *Solar energy materials and solar cells*, vol. 74, no. 1, pp. 65–70, 2002.

[98] Y. Wan, C. Samundsett, J. Bullock, M. Hettick, T. Allen, D. Yan, J. Peng, Y. Wu, J. Cui, A. Javey *et al.*, "Conductive and stable magnesium oxide electron-selective contacts for efficient silicon solar cells," *Advanced Energy Materials*, vol. 7, no. 5, 2017.

[99] Y. Wan, C. Samundsett, D. Yan, T. Allen, J. Peng, J. Cui, X. Zhang, J. Bullock, and A. Cuevas, "A magnesium/amorphous silicon passivating contact for n-type crystalline silicon solar cells," *Applied Physics Letters*, vol. 109, no. 11, p. 113901, 2016.

[100] T. G. Allen, J. Bullock, Q. Jeangros, C. Samundsett, Y. Wan, J. Cui, A. Hessler-Wyser, S. De Wolf, A. Javey, and A. Cuevas, "A low resistance calcium/reduced titania passivated contact for high efficiency crystalline silicon solar cells," *Advanced Energy Materials*, 2017.

[101] J. Bullock, P. Zheng, Q. Jeangros, M. Tosun, M. Hettick, C. M. Sutter-Fella, Y. Wan, T. Allen, D. Yan, D. Macdonald *et al.*, "Lithium fluoride based electron contacts for high efficiency n-type crystalline silicon solar cells," *Advanced Energy Materials*, vol. 6, no. 14, 2016.

[102] R. Labie, T. Bearda, O. El Daif, B. O'Sullivan, K. Baert, and I. Gordon, "Resistance and passivation of metal contacts using n-type amorphous si for si solar cells," *Journal of Applied Physics*, vol. 115, no. 18, p. 183508, 2014.

[103] D. Lachenal, D. Baetzner, W. Frammelsberger, B. Legradic, J. Meixenberger, P. Papet, B. Strahm, and G. Wahli, "Heterojunction and passivated contacts: a simple method to extract both n/tco and p/tco contacts resistivity," *Energy Procedia*, vol. 92, pp. 932–938, 2016.

[104] F. Wang, S. Zhao, B. Liu, Y. Li, Q. Ren, R. Du, N. Wang, C. Wei, X. Chen, G. Wang *et al.*, "Silicon solar cells with bifacial metal oxides carrier selective layers," *Nano Energy*, vol. 39, pp. 437–443, 2017.

[105] Y. Zhang, R. Liu, S.-T. Lee, and B. Sun, "The role of a lif layer on the performance of poly (3, 4-ethylenedioxythiophene): poly (styrenesulfonate)/si organic-inorganic hybrid solar cells," *Applied Physics Letters*, vol. 104, no. 8, p. 083514, 2014.

[106] G. Nogay, J. P. Seif, Y. Riesen, A. Tomasi, Q. Jeangros, N. Wyrsch, F.-J. Haug, S. De Wolf, and C. Ballif, "Nanocrystalline silicon carrier collectors for silicon heterojunction solar cells and impact on low-temperature device characteristics," *IEEE Journal of Photovoltaics*, vol. 6, no. 6, pp. 1654–1662, 2016.

[107] X. Zhang, Y. Wan, J. Bullock, T. Allen, and A. Cuevas, "Low resistance ohmic contact to p-type crystalline silicon via nitrogen-doped copper oxide films," *Applied Physics Letters*, vol. 109, no. 5, p. 052102, 2016.

[108] S. Mahato, L. G. Gerling, C. Voz, R. Alcubilla, and J. Puigdollers, "Pedot: Pss as an alternative hole selective contact for ito-free hybrid crystalline silicon solar cell," *IEEE Journal of Photovoltaics*, vol. 6, no. 4, pp. 934–939, 2016.

[109] M. Tanaka, M. Taguchi, T. Matsuyama, T. Sawada, S. Tsuda, S. Nakano, H. Hanafusa, and Y. Kuwano, "Development of new a-si/c-si heterojunction solar cells: Acj-hit (artificially constructed junction-heterojunction with intrinsic thin-layer)," *Japanese Journal of Applied Physics*, vol. 31, no. 11R, p. 3518, 1992.

[110] H. Fujiwara and M. Kondo, "Effects of a-si: H layer thicknesses on the performance of a-si: H/ c-si heterojunction solar cells," *Journal of Applied Physics*, vol. 101, no. 5, p. 054516, 2007.

[111] H. Matsuura, T. Okuno, H. Okushi, and K. Tanaka, "Electrical properties of n-amorphous/p-crystalline silicon heterojunctions," *Journal of Applied Physics*, vol. 55, no. 4, pp. 1012–1019, 1984.

[112] M. Taguchi, E. Maruyama, and M. Tanaka, "Temperature dependence of amorphous/crystalline silicon heterojunction solar cells," *Japanese Journal of Applied Physics*, vol. 47, no. 2R, p. 814, 2008.

[113] T. Schulze, L. Korte, E. Conrad, M. Schmidt, and B. Rech, "Electrical transport mechanisms in a-si: H/c-si heterojunction solar cells," *Journal of Applied Physics*, vol. 107, no. 2, p. 023711, 2010.

[114] M. Bivour, C. Reichel, M. Hermle, and S. W. Glunz, "Improving the a-si: H (p) rear emitter contact of n-type silicon solar cells," *Solar Energy Materials and solar cells*, vol. 106, pp. 11–16, 2012.

[115] H. Schade and Z. E. Smith, "Contact resistance measurements for hydrogenated amorphous silicon solar cell structures," *Journal of applied physics*, vol. 59, no. 5, pp. 1682–1687, 1986.

[116] K. Ellmer and R. Mientus, "Carrier transport in polycrystalline transparent conductive oxides: A comparative study of zinc oxide and indium oxide," *Thin solid films*, vol. 516, no. 14, pp. 4620–4627, 2008.

[117] A. Kanevce and W. K. Metzger, "The role of amorphous silicon and tunneling in heterojunction with intrinsic thin layer (hit) solar cells," *Journal of Applied Physics*, vol. 105, no. 9, p. 094507, 2009.

[118] ——, "Device physics of heterojunction with intrinsic thin layer (hit) solar cells," *MRS Online Proceedings Library Archive*, vol. 1153, 2009.

[119] E. Centurioni and D. Iencinella, "Role of front contact work function on amorphous silicon/crystalline silicon heterojunction solar cell performance," *IEEE Electron Device Letters*, vol. 24, no. 3, pp. 177–179, 2003.

[120] A. Favier, D. Munoz, S. M. De Nicolás, and P.-J. Ribeyron, "Boron-doped zinc oxide layers grown by metal-organic cvd for silicon heterojunction solar cells applications," *Solar Energy Materials and Solar Cells*, vol. 95, no. 4, pp. 1057–1061, 2011.

[121] A. Howling, L. Sansonnens, J. Ballutaud, C. Hollenstein, and J. Schmitt, "Nonuniform radio-frequency plasma potential due to edge asymmetry in large-area radio-frequency reactors," *Journal of applied physics*, vol. 96, no. 10, pp. 5429–5440, 2004.

[122] H. Takatsuka, Y. Yamauchi, K. Kawamura, H. Mashima, and Y. Takeuchi, "World's largest amorphous silicon photovoltaic module," *Thin solid films*, vol. 506, pp. 13–16, 2006.

[123] B. Legradic, B. Strahm, D. Lachenal, D. Bätzner, W. Frammelsberger, J. Meixenberger, P. Papet, G. Wahli, J. Zhao, D. Decker *et al.*, "High efficiency si-heterojunction technology-it's ready for mass production," in *Photovoltaic Specialist Conference (PVSC), 2015 IEEE 42nd.* IEEE, 2015, pp. 1–3.